Title
Developments in Ultrafast Electron Diffraction for Recording Lattice Dynamics in Quantum and Nanoscale Materials

Author
Durham, Daniel Brian

Publication Date
2022

Developments in Ultrafast Electron Diffraction for Recording Lattice Dynamics in Quantum and Nanoscale Materials

by
Daniel Brian Durham

A dissertation submitted in partial satisfaction of the
requirements for the degree of
Doctor of Philosophy

in

Engineering - Materials Science and Engineering

in the

Graduate Division
of the
University of California, Berkeley.

Committee in charge:
Professor Andrew Minor, Chair
Professor Zakaria Al Balushi
Professor Costas Grigoropoulos

Spring 2022

Developments in Ultrafast Electron Diffraction for Recording Lattice Dynamics in Quantum and Nanoscale Materials

Abstract

Developments in Ultrafast Electron Diffraction for Recording Lattice Dynamics in Quantum and Nanoscale Materials

by

Daniel Brian Durham
Doctor of Philosophy in Engineering – Materials Science and Engineering
University of California, Berkeley

Professor Andrew Minor, Chair

Ultrafast electron diffraction is a developing technique for recording the evolution of atomic structure during dynamic processes. While many exciting discoveries and important observations have been made so far, the technique still faces instrumentation, modeling, and other challenges that inhibit materials science studies, especially of quantum and nanoscale materials. In this dissertation, I describe several developments of UED technology and modeling capabilities to overcome these challenges as well as show a couple of scientific applications. I begin with a general introduction to UED and its value to materials science. I then describe the scattering theory underlying UED patterns and demonstrate a multislice approach that dramatically improves quantitative retrieval of atomic motions in crystals. After this, I introduce the High Repetition-rate Electron Scattering (HiRES) beamline, a state-of-the-art high-brightness UED setup which enables several advances in UED capabilities. I follow up by detailing the first scientific study using the beamline, where a unique light-induced structural melt-recovery process in a quantum material was recorded for the first time. I then show proof-of-principle demonstrations of nanoscale probing enabled by HiRES, including diffraction from isolated nanomaterials as well as focused nanoprobes for nanodiffraction and nanoimaging. Following this, I describe progress towards plasmon-enhanced nanoemitters and how they can be used to further improve the brightness of UED nanoprobes. Finally, I briefly tie together these varied developments and outline areas for further development and scientific exploration. Altogether, the work detailed here expands the reach of UED for study of quantum and nanoscale materials and lays groundwork for further advances that will enable new, wide-open frontiers in materials science.

Contents

Acknowledgments

The efforts described here faced many challenges. Some were experimental challenges due to the unique and complex nature of the custom instruments used. Others were large-scale external disruptions, like handling power loss and lab closures due to local wildfires as well as navigating research and life during the COVID-19 pandemic. The work here was completed thanks to heroic efforts of many team members, colleagues, and collaborators as well as to personal support from friends and family during trying times. So, I gratefully acknowledge the following:

My mom and dad for their steady love, support, and guidance throughout my life

My grandmother Yvonne and late grandfather Ceylon for lending a much needed ear

My PhD advisor Prof. Andy Minor for believing in me and allowing me the flexibility to pursue the range of projects in this work

Dr. Daniele Filippetto for being an energetic, skilled, and good-natured mentor

Fellow members of the HiRES team, including Eric Cropp, Dr. Khalid Siddiqui, and Dr. Fuhao Ji, as well as colleagues and visiting students with whom I worked closely on the plasmon-enhanced emitters project, including Fabrizio Riminucci, Kostas Kanellopulos, Silvia Rotta Loria, and Chris Pierce, for all their tremendous efforts and dedication as well as for their humor and friendship

My colleagues at UC Berkeley and Berkeley Lab for embodying the spirit of team science and helping me to pursue my multi-faceted research

My friends in Cal Community Music for providing a welcoming community and keeping music in my life

All the friends I made here for the games, adventures, and laughs

The Berkeley Fellowship for funding most of the first two years of my graduate stipend

The STROBE NSF Science and Technology Center for funding most of the remaining stipend and providing additional professional development opportunities and scientific community (Grant No. DMR 1548924)

The Office of Science, Office of Basic Energy Sciences, of the U.S. Department of Energy for supporting work performed at the Molecular Foundry under Contract No. DE-AC02-05CH11231

The Laboratory Directed Research and Development (LDRD) Program of Lawrence Berkeley National Lab for supporting the quantum materials science studies under U.S. Department of Energy (DOE) Contract DE-AC02-05CH11231

Chapter 1:

Introduction: Watching atoms dance

To the human eye, solid materials often appear motionless. Yet, at the atomic scale, they are a vibrant ballroom, with electron and nuclei partners spinning and stepping in a chaotic, yet coordinated dance. The complex attractive and repulsive interactions between these particles, governed by the laws of quantum mechanics, typically drive them to organize in a stable arrangement. However, thermal energy causes them to restlessly shimmy around these stable positions. Strongly interacting particles, such as nuclei and bound electrons, perform highly coordinated movements, since each particle's motion necessarily pushes its neighbors. On the other hand, weakly interacting particles, such as weakly bound valence electrons, can whirl around the room essentially unhindered, only changing their direction to avoid close contact with the other particles (or rebounding when they carelessly collide with them).

This dynamic nature and the underlying quantum mechanical interactions lead to many of the interesting properties and behaviors of materials that we use in daily life. For instance, these determine whether a material is conductive or insulating; opaque or transparent; and shiny or dull. Such properties are crucial for electronics; energy storage; paints, inks, and coatings; thermal management; and much more. They also govern how materials change from one state to another, and how their properties can be dynamically controlled and switched. This is especially needed for active materials, which are designed to respond to changes in environment, or in device applications where materials are switched between various contrasting states by applying external forces. So, understanding the atomic-scale interactions and dynamics is valuable for designing, tuning, and controlling materials for a broad range of applications.

Some materials have unusually strong quantum mechanical interactions which lead to unconventional structure, properties, and behaviors. These broadly termed "quantum materials" exhibit a diverse array of extraordinary phenomena[1]. Superconductivity is an oft-studied example, wherein strongly interacting nuclei can help shuttle electrons through a material without electrical resistance. Charge density waves a contrasting example, wherein valence electrons distort nearby nuclei and become trapped, condensing into a periodic superstructure that generally increases electrical resistance. In recent years, such materials have attracted significant attention, not only because of their unique properties but also because the interactions are often sensitive to material composition and the external environment, making them highly tunable and switchable. Numerous research groups and centers are presently devoted to discovering and characterizing quantum materials, and new materials continue to be synthesized and reported.

In addition, a variety of new structures and phenomena emerge as materials are confined in size along one or more dimensions. Broadly termed "nanomaterials" are just nanometers wide along at least one dimension, ie. in the range of one to a thousand atoms across. At this scale, the interactions between particles can change dramatically and lead to behaviors not found in the bulk material. This is especially so for quantum materials. Examples include dramatic changes in optical and electrical properties of single or few-layered 2D flakes[2] as well as the emergence of one-dimensional charge density wave ordering in sufficiently confined 1D wires[3].

How can we understand the complex interactions and dynamic motions underlying such materials? After all, the tempo of the atomic ballroom is mindnumbingly fast. Atomic nuclei in solids can collectively step back and forth in less than a picosecond (10^{-12} seconds), with some atomic-scale processes measured in femtoseconds (10^{-15} seconds). In other words, atoms make more than a trillion steps within just one of ours. A trillion of our steps would be a dance of eternity… lasting more than 30000 years! Recording video with effectively atomic scale resolution and more than 10^{12} frames per second would seem an insurmountable task, especially considering that even the fastest of high-speed cameras today are limited to MHz (10^6 fps) frame rates at best.

The key to catching these “ultrafast" dynamics is to record one snapshot at a time using what are essentially ultrashort strobe lights. Over the past half century, scientists and engineers have learned how to routinely generate repeating laser pulses that are each just femtoseconds long. For one, these can be used to rapidly inject energy into electrons or nuclei of the material to reliably and repeatedly initiate a dynamic process of interest. Simultaneously, these can be used to generate short probe pulses to capture snapshots of the material at varying times. This “pump-probe" approach allows to record a time series of processes by which the energized particles transfer their energy, providing a window into the strength of interactions between particles. In some cases, the particles making up a solid will collectively re-organize in response to laser pulses, and studying the ordering dynamics can provide information about the fundamental interactions at play. Sometimes, new orderings are discovered which can find application in light-driven devices such as photodetectors and photonic computers.

Energetic electrons are increasingly used as the dynamic probes, which are generated from ultrashort laser pulses using photoemission. One scheme is ultrafast electron diffraction (UED), in which short, high-energy electron pulses impinge on the sample and the coherent scattering pattern from the atomic lattice is recorded. These diffraction patterns provide information about the atomic structure, including spacings between atoms, crystallinity, and magnitude of atomic vibrations. High energy electrons scatter strongly, especially from the atomic nuclei, providing signals even from just a few atomic layers. This approach has already been used to discover and record a wide range of light-induced structural processes, such as rapid switching between charge density wave arrangements in tantalum dichalcogenides[4], transient competition between charge density wave formation along perpendicular axes in rare earth tellurides[5], and multi-step energy transfer mechanisms in materials such as graphite[6].

However, many challenges remain in performing and interpreting UED measurements. In many cases, the probe electrons scatter from a material multiple times as they pass through, complicating the resulting scattering pattern. Also, pulsed electron beams are often not very bright due to the strong repulsion between electrons. This necessitates numerous hours or even days to obtain good quality diffraction movies even from relatively large, millimeter-scale regions of material. This limitation often prevents access to dynamics that occur within nanoscale volumes.

My work entailed in this dissertation contributes several developments in UED for recording atomic structure dynamics in quantum and nanoscale materials. First, in Chapter 2, I demonstrate a multislice approach to modeling UED patterns that greatly improves quantification of atomic motions in crystals. In the process, I discuss scattering theory that provides a basis for understanding the UED measurements that follow. The next two chapters describe the development and application of a higher brightness UED instrument. In Chapter 3, I introduce the newly commissioned High Repetition-rate Electron Scattering (HiRES) beamline at Lawrence Berkeley National Laboratory, a state-of-the-art setup that enables relativistic UED with unprecedented average brightness. In Chapter 4, I describe the first scientific study at HiRES: observing a light-induced structural melt-recovery process in $TaTe_2$, a layered quantum material, for the first time. In the final two chapters, I detail developments that facilitate study of nanomaterials. In Chapter 5, I demonstrate instrument advances at HiRES to enable probing of dynamics in nanoscale volumes. In Chapter 6 I illustrate the design, prototyping, and testing of plasmon-enhanced photoemitters for brighter pulsed electron sources. I conclude by summarizing the described advances and providing a perspective on future growth areas in instrumentation and scientific study.

Chapter 2:

Multislice diffraction models to quantify atomic motions in crystals

---

2.1 Need for improved dynamical scattering models for UED

One of the most alluring quests of ultrafast electron diffraction (UED) studies is to extract movies of atomic motions during photoinduced processes. Examples include structural transformations, coherent lattice oscillations (phonons), incoherent thermal motions, and more. While scattering patterns are sensitive to all of these phenomena, accurate quantitative retrieval of such motions from UED experiments can be challenging: this is because electrons scatter strongly from solids, leading to multiple scattering and channeling phenomena that complicate the relationship between the electrostatic potential of the material and the resulting scattering pattern.

When the probing particles have a low scattering cross section and scatter at most once passing through the material, then single scattering (kinematical) models can be applied. The simple analytical form of these models provides a Fourier transform relationship between the electrostatic potential and scattering pattern, allowing atomic coordinates and thermal displacement parameters to be retrieved by a Gerchberg-Saxton algorithm[7, 8] which iteratively updates the atomic parameters and scattered wave phases to provide the best match. This approach is routinely used for high energy x-ray and neutron scattering which have low scattering cross section and typically scatter no more than once when passing through micrometers or even millimeters of material.

Electrons, on the other hand, can be subject to multiple scattering and channeling effects through even just a few to tens of nanometers of material[9]. These effects greatly complicate the relationship between structure and signal, prohibiting direct inversion of the scattering pattern to retrieve atomic coordinates. Though using relativistic electron probes provides a longer mean free path, multiple scattering effects are often still present even at MeV-scale energies. These effects are especially prevalent in dense, inorganic solids, as well as single crystals viewed along high-symmetry zone axes. Many interesting quantum and nanoscale materials have one or both of these characteristics. In such cases, modeling the complete, “dynamical” diffraction process is needed to accurately retrieve the full structural information.

At present, approaches for modeling dynamical diffraction in UED are limited. Existing procedures, such as those developed for static diffraction in TEM, do not always account for factors that are important in UED, such as lattice temperature and mesoscale sample topography (averaged over the um to mm probe size). UED studies that do invoke dynamical diffraction models typically use N-beam scattering matrix (Bloch wave) methods: However, these calculations are computationally intensive for complex samples where many diffracting beams are needed to capture the behavior, such as multilayered films, amorphous layers or substrates, and large superlattices[10–12]. Also, while these prior examples were able to extract the specific information desired from their experiment, they could not quantitatively match the diffraction signals with the dynamical model alone, requiring introduction of additional, empirical offsets and functions to fit the data. Accurate, quantitative modeling of diffraction signals is needed to retrieve the full structural information.

In this chapter, I describe a multislice modeling approach tailored for UED studies of single crystal films. This has been used to quantify photoinduced atomic motions in experiments at HiRES as described in later chapters. These models match measured diffraction patterns as well as photoinduced changes considerably better than kinematical models, and provide a means to access more detailed structural information. I will first discuss the relevant scattering theory underlying these models. Then, I will introduce the technical details of the multislice calculations and describe how various physical parameters are incorporated, including beam properties, lattice temperature, and sample topography. Finally, I demonstrate quantification of photoinduced thermal atomic motions in pump-probe UED measurements on ultrathin single crystal gold films, showcasing both the necessity and utility of multislice models for quantifying atomic motions in single crystals.

2.2 Theory of scattering from crystalline solids

2.2.1 Scattering from individual atoms

Electrons scatter from materials because the charged electrons strongly interact with the electrostatic potential of the atoms in the material. The electrostatic potential of a single atom arises from the positive atomic nucleus at the center, effectively a point charge, screened by the surrounding negative charge distribution from the electrons. The charge distribution can be calculated using first principles calculations via Hartree-Fock theory, and then the electrostatic potential of the atom, $V_a(\mathbf{r})$, can be calculated using electromagnetic theory[13]. From this potential, the angle-dependent scattering amplitude for an incident electron upon a single atom, called the atomic scattering factor, can be calculated. These scattering factors are typically expressed as functions of the scattering vector $\mathbf{q}$ with magnitude $q = \frac{2\sin\theta/2}{\lambda}$: This employs the convention that reciprocal space coordinates are defined by $k_i = 1/x_i$ and that θ, refers to the full scattering angle. In later chapters and in other works, the scattering vector may be defined as $\mathbf{s}$ with magnitude $s = 2\pi q = \frac{4\pi\sin\theta/2}{\lambda}$

A popular form for the atomic scattering factor is obtained using the first Born approximation, in which an incident plane wave yields an outgoing plane wave of identical amplitude and phase plus a scattered spherical wave: $\psi_t = \psi_i + f_e(\mathbf{q})\frac{e^{2\pi i\mathbf{q}\cdot\mathbf{r}}}{r}$. This approximation holds when the scattering field is small compared to the incident field. In this case, the scattering amplitude is independent of the electron energy, given simply by the three-dimensional Fourier transform of the atomic potential[13]:

$$f_e(\mathbf{q}) = \frac{2\pi m_0 e}{h^2}\int V_a(\mathbf{r})e^{2\pi i\mathbf{q}\cdot\mathbf{r}}d^3r \tag{2.1}$$

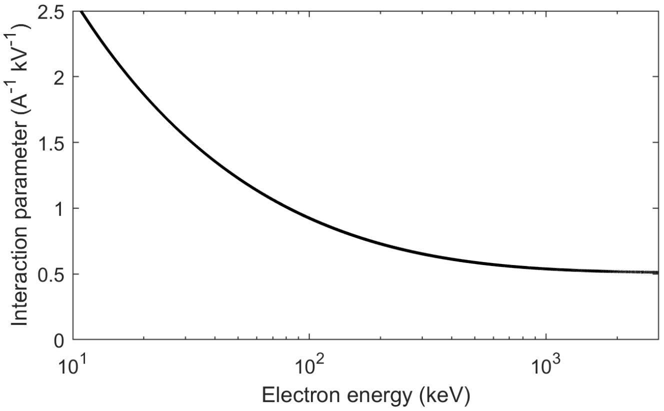

Figure 2.1: Relativistic electron interaction parameter as a function of kinetic energy.

The Fourier transform relationship implies that denser atoms will scatter electrons over a broader angular range.

An improved expression is obtained using the weak phase object approximation, where the potentials are treated as phase shifting elements such that the transmitted electron wave function $\psi_t = t(\mathbf{r})\psi_i$ and the transmission function $t(\mathbf{r}) = e^{i\sigma_e V_a(\mathbf{r})} \approx 1 + i\sigma_e V_a(\mathbf{r})$ (the final step is a Taylor expansion, where higher order terms are neglected in the weak phase object limit). The electron interaction parameter, σ_e, is the energy-dependent proportionality constant giving the amount of phase shift induced by the potential, and is given by the following expression:

$$\sigma_e = \frac{2\pi}{\lambda E_0}(\frac{m_0c^2 + eE_0}{2m_0c^2 + eE_0}) \tag{2.2}$$

This expression is derived using relativistic quantities, and holds assuming the specimen potential is much smaller than the beam energy. Notably, the interaction parameter decreases with energy, and plateaus as electron energies enter the relativistic regime, illustrated in Figure 2.1. This behavior implies that for electron microscopy and diffraction, electron-specimen interactions and dynamical scattering effects can be reduced by increasing the electron energy, but with diminishing returns at relativistic energies.

In the weak phase object approximation, the scattering factor becomes a complex function:

$$f_e(q) = \frac{2\pi i}{\lambda}\int_0^\infty J_0(2\pi qr)(1 - e^{i\sigma_e \int V_a(x,y,z)dz})rdr \tag{2.3}$$

where J_0 is the zeroth order Bessel function. This form is essentially the Fourier transform of the transmission function in the weak object approximation. Heavier atoms at lower electron energies impart significant phase shift in the electron wave, which manifests in the scattering factor as an imaginary component which is not accounted for in the Born approximation. This phase shift can modify measured diffraction patterns if multiple atom species with large variation in atomic number are present in the specimen. Examples of scattering factors computed using Born and weak phase object approximations are shown in the Figure 2.2. While the scattering magnitudes are consistent, the weak phase object approximation yields a significant imaginary component for heavier atoms, lower electron

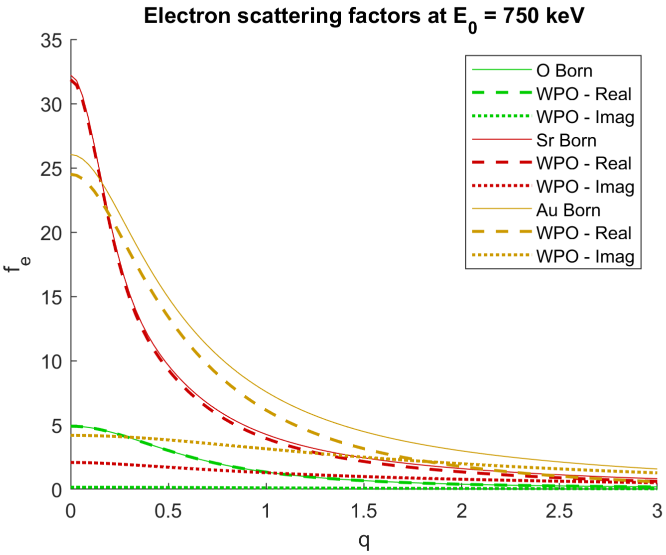

Figure 2.2: Atomic scattering factors for selected elements of varying atomic number. Scattering factor is plotted against the scattering vector, q. Real scattering factors computed using the Born approximation (solid lines) as well as complex scattering factors (dashed lines) computed using the weak phase object (WPO) approximation are shown for gold, strontium, and oxygen atoms.

energies, and higher scattering angles.

In solid materials, then, electron scattering patterns are produced by coherent interference of scattering from the overall electrostatic potential of the material. First principles calculations could be used to calculate the 3D electrostatic potential throughout the solid, but instead the independent atom model is typically invoked. In this model, the electrostatic potential in the material is simply the sum of the potentials of the individual atoms. While this model does not account for changes in the valence electron distribution due to bonding or other interatomic interactions, these are typically expected to be minor corrections since the scattering mainly occurs near the atomic nucleus. This model is also easy to use since scattering factors have been calculated for most atoms and are readily available in a database[13], and so this approach can be implemented without performing first principles calculations.

2.2.2 Scattering from a crystal

A periodic arrangement of scatterers, as in a crystalline solid, leads to constructive interference of the scattered waves at certain angles. This leads to the two-dimensional diffraction patterns recorded from crystals in electron diffraction studies, including UED. The angles of constructive interference for an array of scatterers with interplanar spacing d are given by Bragg's law:

$$n\lambda = 2d \sin\theta_s \tag{2.4}$$

Where θ_s is the scattering semi-angle. Importantly, the wavelength of the incident radiation must be smaller than the spacing between the scatterers to observe this constructive interference, and smaller wavelengths lead to smaller scattering angles. Relativistic electrons have much smaller de Broglie wavelength ($\lambda = 0.0107\,\text{Å}$ for 750 keV electrons) than typical spacings between atoms (one to few Å). So, for relativistic electrons, elastic scattering angles are typically within the small angle approximation, ie. $\sin\theta \approx \theta$. It is also worth noting that larger interplanar spacings produce diffraction at smaller angles, requiring a smaller angular spread to resolve them. The transverse coherence length can be defined as $L_x = \frac{\lambda}{2\pi\sigma_\theta}$, and this should be much more than π times larger than the interplanar spacing to clearly distinguish diffraction peaks[14]. This will be discussed further in following chapters, as for quantum materials, UED probes must be prepared with large enough coherence lengths to resolve large emergent superstructures.

The positions of Bragg diffraction peaks can be determined by considering the interaction of the incident wave with the reciprocal lattice of the crystal. In three dimensions, an array of scatterers provides constructive interference for a 3D array of conditions. Only scattering vectors which are perpendicular to a set of planes and have magnitudes which are multiples of the inverse spacing will interfere constructively. For a lattice defined by lattice vectors **a**, **b**, and **c**, these scattering vectors are defined by the corresponding reciprocal lattice vectors, ie.

$$\mathbf{q_{hkl}} = h\mathbf{a}^* + k\mathbf{b}^* + l\mathbf{c}^* \tag{2.5}$$

where h, k, and l are integer Miller indices which specify a lattice plane.

In general, a reciprocal lattice basis is defined by:

$$\mathbf{a}^* = \frac{\mathbf{b} \times \mathbf{c}}{\mathbf{a} \cdot (\mathbf{b} \times \mathbf{c})} \tag{2.6}$$

and so on for the other two reciprocal lattice vectors. Graphically, this appears as an array of points in reciprocal space. The incident wave vector can be drawn with its orientation relative to the scattering crystal. Due to energy conservation ($|\mathbf{k_{scat}}| = |\mathbf{k_0}|$), possible scattered waves lie on a sphere in reciprocal space, the so-called Ewald sphere. Then, intersections between this sphere and the reciprocal lattice represent possible elastic scattering events. So, a diffraction pattern from a single crystal consists of an array of diffraction peaks with positions given by the $\mathbf{q_{hkl}}$ which intersect the Ewald sphere.

2.2.3 Kinematical scattering model

In situations where the incident electrons scatter at most once from the material, kinematical scattering theory can be applied to calculate the relative diffraction peak intensities. For a range of UED experiments on weakly scattering polycrystalline or amorphous materials, this theory is valid and can be applied for quantitative analysis. However, in the UED experiments described in this work on strongly scattering, single crystal materials, signals deviate from kinematical theory and require a full dynamical treatment as developed in section 2.3. Still, even in those cases, kinematical models provide initial intuition and will be used as a point of comparison throughout this work. The components of kinematical theory that are relevant for calculations that follow are described here.

Structure factor

In the kinematical scattering model, the amplitude and phase of the total scattered wave at a scattering vector is given by the coherent summation of the scattered waves from all atoms in the crystal. This is the structure factor, F_{hkl}:

$$F_{hkl} = \sum_j f_j(q_{hkl}) e^{-2\pi i \mathbf{q_{hkl}} \cdot \mathbf{r_j}} \tag{2.7}$$

Where j is the index for an atom in the crystal unit cell and r_j is the position of that atom in the cell. Typically, diffraction patterns are directly recorded on a camera such that the intensity is proportional to $|F_{hkl}|^2$ and the phase information is lost.

It follows that by tracking diffraction peak intensities as a function of time following a stimulus, UED is sensitive to changes in the atomic positions within the unit cell. For instance, structural phase transformations often change the symmetry of the unit cell, causing diffraction peaks to appear or disappear. In cases where the kinematical model is valid, the atomic coordinates can be retrieved via iterative Fourier transform-based algorithms (ie. Gerchberg-Saxton method).

Shape factor

Because the crystals studied in UED are typically very thin (tens of nanometers), shape effects become important. The small thickness leads to significant broadening of reciprocal lattice spots in the thickness dimension to form so-called “relrods,” expanding the range of diffraction spots that can simultaneously meet the diffraction condition at a given orientation and thereby increasing the number of spots observed in a diffraction pattern. That numerous diffraction spots can be simultaneously observed is a valuable feature of relativistic UED measurements, allowing detailed analysis of structure change across a range of reciprocal space all at once.

The functional form of a relrod for a thin, flat crystal is given by the Fourier transform of a square pulse with total width equal to the thickness, t, ie. a sinc function:

$$f_{rod}(q_z) \propto \mathscr{F}\{\mathrm{rect}_t(z)\} = t\mathrm{sinc}(q_z t) = \frac{\sin(\pi q_z t)}{\pi q_z} \tag{2.8}$$

The diffracted intensity becomes:

$$I_{hkl} = \frac{\sin(\pi \Delta q_{z,hkl} t)}{(\Delta q_{z,hkl} \xi_{hkl})^2} \tag{2.9}$$

where $\Delta q_{z,hkl}$ is the excitation error, ie. the distance in reciprocal space between the Ewald sphere and the Bragg condition for Miller indices h, k, and l and angle β between the beam and the surface normal:

$$\Delta q_{z,hkl} = \frac{-\mathbf{q_{hkl}} \cdot (2\mathbf{k_i} + \mathbf{q_{hkl}})}{2|\mathbf{k_i} + \mathbf{q_{hkl}}| \cos(\beta)} \tag{2.10}$$

and ξ_{hkl} is the extinction distance:

$$\xi_{hkl} = \frac{\pi V_{cell} \cos(\theta_s)}{\lambda |F_{hkl}|} \tag{2.11}$$

where V_{cell} is the unit cell volume.

Debye-Waller factor

Scattering amplitudes are also sensitive to thermal motions of the atoms. Higher temperature increases incoherent thermal motions, effectively broadening the electrostatic potential. It also introduces some randomness into the potential observed by each incident electron, reducing the overall coherence of the scattering events and increasing inelastic scattering at angles between the Bragg spots. Recalling from the previous section that the scattering amplitude is related to the Fourier transform of the electrostatic potential, it follows that larger thermal motions reduce high-angle scattering. In a case where all atoms are identical in a crystal with a position distribution given by a 3D gaussian, then the angle-dependent damping of diffracted intensity due to temperature is given by the Debye-Waller factor:

$$DWF(q) = e^{-4\pi^2 q^2 u_{rms}^2} \tag{2.12}$$

Where u_{rms} is the 1D root-mean-square atomic displacement perpendicular to the Bragg planes (note that other works may use the 2D (in-plane) or 3D (total) displacements, which will change the constant prefactor). In general, thermal motions can differ between atomic sites in the unit cell, leading to more complex expressions for DWF.

In UED, the change in u_{rms} is often extracted by fitting the following equation to the measured diffraction intensity changes:

$$ln(\frac{I_{hkl}(t_1)}{I_{hkl}(t_0)}) = \Delta u_{rms}^2(-4\pi^2 q_{hkl}^2) \tag{2.13}$$

This can be done via linear regression to retrieve Δu_{rms} from the slope.

This analysis only considers the Bragg peaks formed due to elastic scattering, neglecting contributions from inelastic scattering. In thin single crystals, the elastic scattering is typically much stronger than the inelastic scattering background and so it is often reasonable to neglect inelastic contributions. Between the Bragg peaks in a single crystal, as well as between and beneath diffraction rings in a polycrystal, inelastic scattering can be significant or even dominant, allowing detailed study of thermal motions. This is not explored in this work, but is an area of great interest and several UED studies have focused on this aspect[15].

2.2.4 Orientation effects in crystals

The orientation of the crystal relative to the incident radiation has a significant effect on the diffraction pattern observed. Rotating the crystal effectively rotates the reciprocal lattice relative to the Ewald sphere, changing the measured diffraction intensities and even changing which reflections are observed. In general, the thin crystal films prepared for UED are rippled, consisting of multiple orientations relative to the incident radiation, and UED probes are typically so large (tens of microns to millimeters in size) that all of these orientations are probed simultaneously.

Te total diffracted intensity is a weighted average of the diffraction patterns from the distribution of orientation angles θ_x and θ_y:

$$I_{hkl,avg} = \iint_A p(\theta_x, \theta_y) I_{hkl}(\theta_x, \theta_y)\, d\theta_x\, d\theta_y \tag{2.14}$$

There are a few important consequences of this for UED measurements. Firstly, if the sample ripples or buckles during the experiment, it can lead to changes in the scattering pattern. This typically comes about from thermal strain, which can lead to complex changes that either need to be compensated[16] or, in some cases, are a subject of study [17]. Secondly, samples with significant rippling will bring more relrods into diffraction condition: this can expand the q range over which diffraction peaks can be simultaneously recorded, but can also complicate interpretation if the rippling is sufficiently large such that peaks from multiple zone axes are simultaneously excited and overlap. Finally, by averaging over a range of orientations, sample rippling reduces sensitivity of the recorded peak intensities to the sample stage tilt. This last effect is especially important in situations with significant multiple scattering, which will be discussed in the next section.

2.2.5 Onset of multiple scattering

Up to this point, the discussed theory assumes sufficiently thin specimens such that electrons effectively scatter just once. However, the elastic scattering cross sections for electrons from individual atoms are high, and so multiple scattering events are likely in a dense solid. An *upper bound* on the onset of multiple scattering can be obtained by calculating the elastic mean free path (MFP)[18]:

$$\lambda_{MFP} = \frac{1}{\sigma_{total}} = \frac{1}{\sum_i N_i \sigma_{atom,i}} \tag{2.15}$$

Where N_i is the number density of atoms of species i in the solid and $\sigma_{atom,i}$ is the total elastic scattering cross section of each atom. For these calculations, the following formula was used[18]:

$$\sigma_{atom} = 2\pi \int_0^\pi \frac{d\sigma}{d\Omega} \sin(\theta) d\theta = 2\pi \int_0^\pi |f(\theta)|^2 \sin(\theta) d\theta \tag{2.16}$$

Where $f(\theta)$ is the energy and species-dependent atomic scattering factor calculated using the weak phase object approximation. The calculated σ_{atom} are in good agreement with those tabulated in the NIST elastic scattering cross section database, which includes values for energies up to 300 keV.

Calculated MFPs for a selection of materials are shown in Table 2.1. notably, many of the quantum materials and metals studied in this work have elastic MFPs near or below 50 nm even for MeV-scale electrons. Pushing to MeV-scale electron energies provides diminishing returns to increase the MFP. Indeed, a tenfold increase in energy from 300 keV (high TEM energy) to 3 MeV (common MeV-UED energy) only provides about a 50% increase in mean free path.

All that said, it is crucial to note that the MFP is an upper bound for the onset of multiple scattering. The MFP estimates the average distance traveled by all incident electrons before scattering, but correlation between scattering events must also be taken into account. For instance, consider electrons incident upon a crystal along a high symmetry zone axis. Electrons which impinge upon an atomic column will have a much smaller free path than electrons which impinge between the columns, and so electrons that impinge upon atomic columns are likely to experience multiple scattering effects at depths much smaller than the

Table 2.1: Elastic mean free paths computed for electrons of selected energies impinging on selected materials.

	Elastic mean free path (nm)				
	60 keV	200 keV	300 keV	750 keV	3 MeV
Graphite	72.4	175	218	302	354
Silicon	45.5	109	136	187	219
VO_2	24.6	58.0	72.0	99.4	116
$SrRuO_3$	15.5	34.5	42.5	57.9	67.4
$TaSe_2$	12.6	26.5	32.2	43.3	50.0
Bismuth	11.1	21.8	26.1	34.4	39.5
$TaTe_2$	10.6	22.0	26.8	35.9	41.5
Gold	6.08	11.9	14.3	18.8	21.6

MFP. This is a crucial point: After all, diffraction peaks are comprised only of electrons which have been scattered at least once, and so if the only electrons are scattering are those that are likely to scatter again, the diffraction pattern will be dominated by multiple scattering effects. This effect is exacerbated in single crystals due to the attraction of electrons to the atomic nuclei, leading to “channeling" of electrons along the atomic columns and further complicating scattering behavior[9, 13].

Knowing this, it becomes apparent that diffraction from oriented crystals will deviate from kinematical theory at thicknesses much smaller than the MFP, as will be demonstrated in section 2.3. Even for amorphous materials, multiple scattering effects emerge for film thicknesses greater than 0.2 times the MFP[19].

These effects demand application of dynamical theory to quantitatively model diffraction signals when probing dense crystals oriented along high symmetry zone axes, even when using relativistic UED probes. These conditions are met routinely: many quantum materials are grown as high purity single crystals to preserve delicate superstructures and low-energy excitations, and even simple metals and semiconductors are often studied as single crystals in effort to access intrinsic carrier relaxation dynamics free of grain boundary scattering. Unfortunately, dynamical theory loses the simple Fourier transform relationship between the real-space electrostatic potential and the reciprocal-space scattered wave of kinematical theory. Instead, a more detailed forward model must be invoked and different optimization procedures must be applied to retrieve the atomic structure information.

2.2.6 Schrödinger equation for fast electrons

In the full dynamical treatment, electron scattering patterns are obtained by solving the Schrödinger equation for fast electrons in the material[13]:

$$\frac{\partial \psi(\mathbf{r})}{\partial z} = \left[\frac{i\lambda}{4\pi}\nabla_{xy}^2 + i\sigma V(\mathbf{r})\right]\psi(\mathbf{r}) \tag{2.17}$$

Here, ψ is the electron wave function, λ is the electron de Broglie wavelength, σ is the interaction parameter, and V is the electrostatic potential of the material. The two terms on the right-hand side correspond to propagation of the electron wave (left term) and interaction with the electrostatic potential (right term).

Two approaches have generally been taken to solve this equation. The first is to expand the crystal potential and electron wave function into components with periodicity of the crystal and to set up and solve the resulting matrix equation. There are an infinite number of components in this basis, so for practical computation only a set of the most significant components are included, essentially giving the number of diffracted beams included in the calculation. This approach has been applied to UED data analysis in some limited cases, but usually for studying individual, strong reflections rather than computing entire patterns with quantitative accuracy. A likely reason for this is that the time to solve the matrix equation scales with N^3, where N is the number of diffracted beams considered[13].

The second approach is a multislice calculation. In this case, the diffraction process is modeled as sequential interaction with and propagation through slices of projected electrostatic potential of the atoms. A plane wave electron beam is propagated through the crystal, and then the scattering pattern is computed as the Fourier transform of the exit wave. This approach scales with NlogN and so can be more efficient when many diffracted beams need to be accounted for[13]. Quantum materials with weak superlattice peaks are an important example: superlattice peak intensities are strongly affected by multiple scattering, and so accurate quantitative modeling requires inclusion of both the superlattice peaks and most of the strong primary Bragg peaks. So, the multislice approach is taken in this work, with some modifications to suit UED experiments.

2.3 Multislice calculation of UED patterns

2.3.1 Multislice computation method

Simulations start with a plane wave beam (spatially uniform envelope) and advance the beam through each slice of material. This is done by applying the interaction and propagation terms separately as operators[20, 21]. First, an interaction operator is applied in real space:

$$\psi_{p+1}(\mathbf{r}) = \psi_p(\mathbf{r}) e^{i\sigma V_p^{2D}(\mathbf{r})} \tag{2.18}$$

where $V_p^{2D}(\mathbf{r})$ is the projected electrostatic potential within the slice. The parameterized projected potentials as determined by Kirkland [22] are used in this work. Second, a propagation operator is applied in reciprocal space:

$$\psi_{p+1}(\mathbf{q}) = \psi_p(\mathbf{q}) e^{-i\pi\lambda|\mathbf{q}|^2 t} \tag{2.19}$$

An anti-aliasing filter is applied at this step by setting to zero all values at reciprocal space positions larger than $q_{max}/2$. These two steps are repeated until the beam reaches the end of the material. The diffraction is then obtained from the Fourier transform of the exiting envelope:

$$I(\mathbf{q}) = |\mathcal{F}(\psi(\mathbf{r}))|^2 = |\psi(\mathbf{q})|^2 \tag{2.20}$$

Lattice temperature is accounted for by applying Debye-Waller damping to the projected potentials. This approximation models the electron beam traveling through a time-averaged electrostatic potential, and has been shown to account for the influence of thermal motions on the coherent Bragg diffraction[23]. Thermal diffuse scattering is not included here, but is much weaker and broader than the Bragg diffraction peaks and will generally be removed from experimental UED patterns when analyzing primary diffraction peak dynamics. Consider atoms that move randomly with an rms displacement of u_{RMS} along each dimension. This forms a 2D gaussian distribution of positions:

$$p(r) = \frac{1}{2\pi u_{RMS}^2} e^{-\frac{r^2}{2u_{RMS}^2}} \tag{2.21}$$

This distribution is convolved with the electrostatic potential in real space, effectively acting as a Gaussian filter. This filter in Fourier space is:

$$p(q) = e^{-2\pi^2 u_{RMS}^2 q^2} \tag{2.22}$$

noting that the form of this filter is similar to the kinematical Debye-Waller factor, but with half of the constant prefactor (Debye-Waller factor applies to scattered intensities whereas this filter applies to the scattering potential). This approach is readily generalized to anisotropic or anharmonic thermal motions by applying the corresponding two-dimensional filter.

2.3.2 Example calculations for flat single crystal gold

To illustrate the multislice method and compare the behavior to kinematical predictions, example calculations of single crystal gold are shown here. The films were oriented along [001] zone axis, and so each unit cell could divided into two atomic slices. The projected potentials of these slices are illustrated in Figure 2.3. With zero temperature, the projected atomic potentials are sharp with long tails. After applying Debye-Waller damping for thermal atomic displacements near 300 K, the potentials are greatly broadened and approximately Gaussian.

Each simulation parameter was tuned by performing a series of simulations increasing that parameter until the diffraction signals converge. The crystallographic R factor is used as the metric, given by:

$$R = \frac{\sum_{hkl} |\sqrt{I_{hkl}^{i}} - \sqrt{I_{hkl}^{i_{max}}}|}{\sum_{hkl} \sqrt{I_{hkl}^{i_{max}}}} \tag{2.23}$$

which compares step i and the final step, i_{max}. All simulations in this work are converged until the R factor computed over the first seven diffracted orders is less than 1%. The

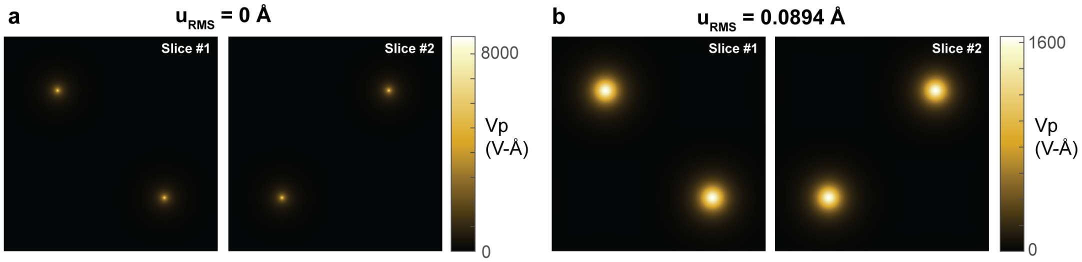

Figure 2.3: Projected potential slices for multislice calculations of single-crystal gold films viewed along [001] for **a** zero temperature and **b** room temperature.

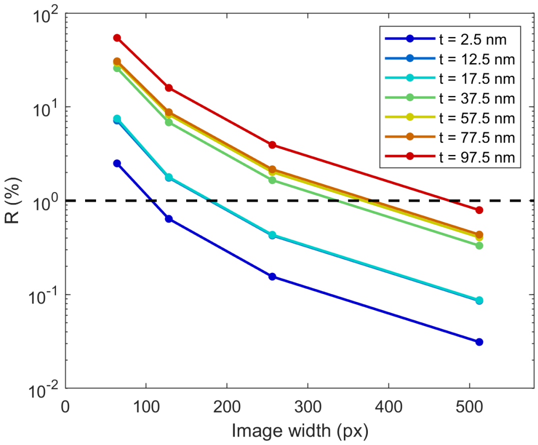

Figure 2.4: Convergence of multislice diffraction for a flat, single-crystal gold film probed with a 750 keV electron wave.

main parameter to converge is the real-space pixel size (q range), which must be sufficiently small (large) to include enough of the scattered beams for accurate diffraction calculations. The image dimensions are chosen to be powers of 2 to maximize the speed of the fft-based calculations.

A multislice calculation for 750 keV electrons is illustrated in Figure 2.5. The magnitude and phase of the electron wave as it travels through the material are shown in panels a-b. Despite the high electron energy, the gold atoms impart large local phase shifts on the electron wave, leading to strong channeling down the atomic columns within just a few unit cells. Interference of waves scattered from each slice leads to oscillations in the wave function magnitude with depth. Note that inelastic and diffuse scattering are not included here, which would attenuate the electron wave as it progresses. Altogether, this leads to a complex modulation of diffraction peak intensities as a function of thickness (Figure 2.5c).

Similar calculations for a set of selected beam energies are shown in Figure 2.6. While the channeling periodicities are longer for higher beam energies, diffraction peak ratios still show complex behaviors within a few nanometers. As such, the R factor between multislice and kinematical calculations rapidly diverges within a few nm (shown in Figure 2.7).

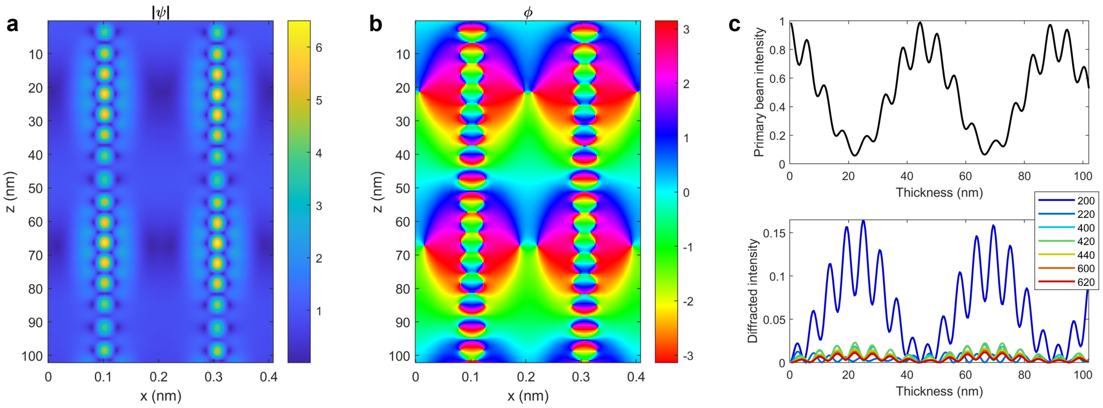

Figure 2.5: Multislice simulation of 750 keV electron wave traveling through single-crystal gold along [001]. **a-b** Channeling plots showing magnitude and phase of the wave function throughout an x-z slice of material. **c** Evolution of the 000 and diffracted beam intensities.

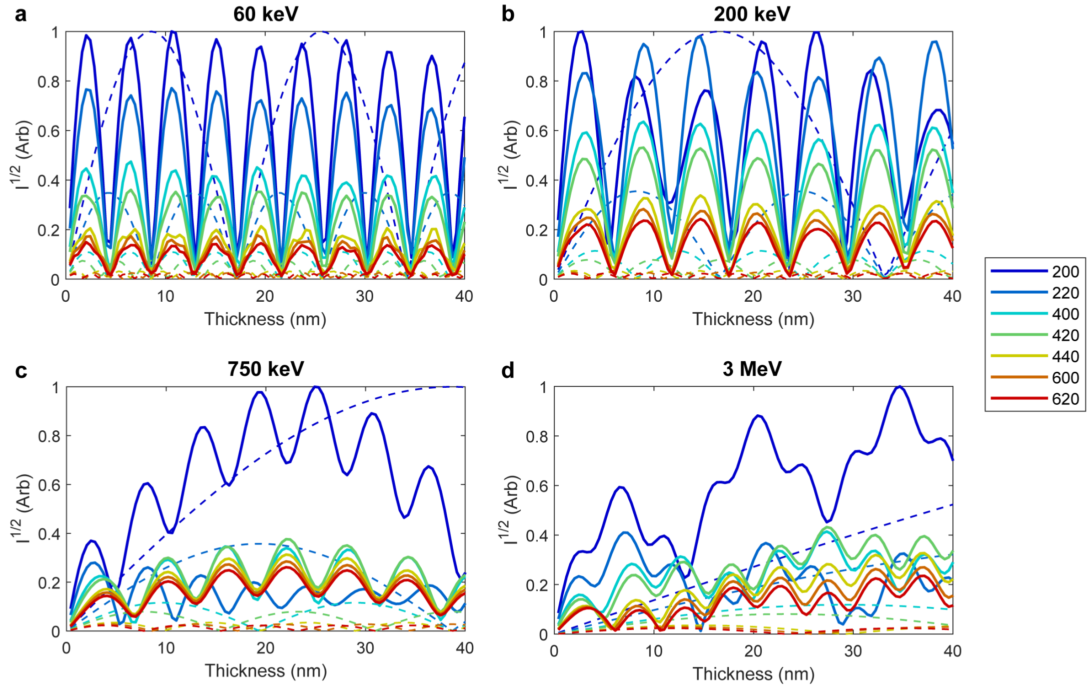

Figure 2.6: Simulated thickness dependence of the square root of diffracted beam intensities for four selected kinetic energies through a flat, single-crystal gold film.

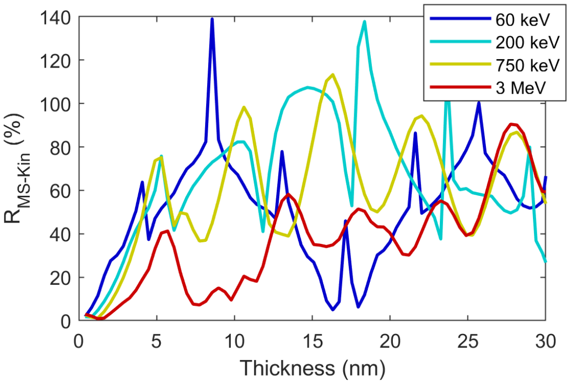

Figure 2.7: Difference between multislice and kinematical diffraction patterns of a flat, single-crystal gold film for four selected beam energies. The R factor of the first seven diffracted orders is the depicted metric.

2.3.3 Averaging orientations in rippled crystals

In UED, the mm-scale electron probes average signals from a sample with macroscale topography, ie. rippling. On one hand, this aspect can be advantageous: averaging over a range of beam-sample orientations can smooth out the highly sensitive, oscillatory behavior of dynamical diffraction signals. For instance, precession electron diffraction (PED), attained by spinning the electron beam around a cone of incident angles and recording the averaged diffraction pattern, is shown to have reduced sensitivity to sample tilt and thickness. This smoothness can extend the validity of kinematical approximations[24], and has also facilitated successful refinement of structural parameters using dynamical models[25].

On the other hand, sample rippling complicates the multislice modeling as a distribution of tilt angles must be computed and incoherently summed. Essentially, the problem is to compute the following integral:

$$I_{hkl,avg} = \iint_A p(\theta_x, \theta_y) I_{hkl}(\theta_x, \theta_y)\, d\theta_x\, d\theta_y \tag{2.24}$$

Which is an integral of the diffraction signal I_{hkl} at each orientation given by the tilt angles θ_x and θ_y, weighted by the distribution of orientations, p.

There are two main challenges with computing this integral as compared to that used to model PED. Firstly, it is a 2D integral compared to the 1D integral used for PED; this alone increases the sampling needed by a factor of order N. Secondly, the UED sample necessarily includes orientations that are nearly on-zone, where numerous diffraction orders are simultaneously strongly excited and multiple scattering effects are maximized, leading to a complex, highly sensitive behavior of I_{hkl}. PED, on the other hand, can benefit from using a large enough precession angle to avoid sampling near the zone axis.

For the calculations that follow, the integral is computed using an iterative 2D trapezoidal quadrature algorithm[26]. On the first iteration, a square sampling grid is initialized with just four samples: one at each corner. Then, on each successive iteration, points are added to complete a sampling grid with half the spacing in each dimension. A running integral is computed by adding 3/4 of the newly integrated points to 1/4 of the previous integral value.

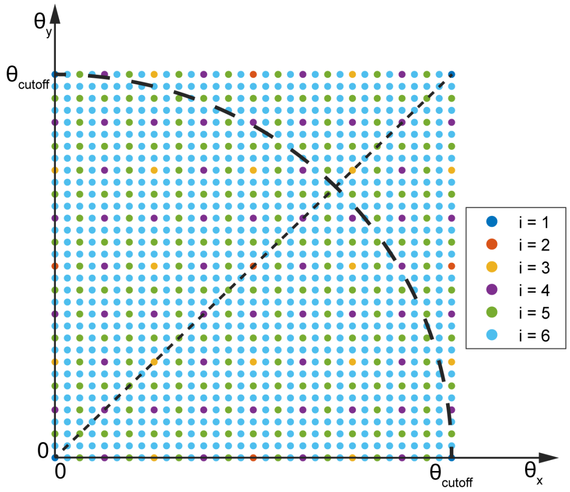

Figure 2.8: Schematic of the iterative sampling grid used for trapezoidal quadrature integration of the diffracted intensities of a rippled film. Each iteration halves the sample spacing. Tilt distributions with varying σ_{theta} can be calculated in parallel by Gaussian weighting of the samples. Samples above the cutoff angle θ_{cutoff} are not included. For zone axes with four-fold and mirror symmetry like [001] of FCC gold, only samples below the $\theta_y = \theta_x$ line need to be calculated. Contributions from other angles are symmetrically equivalent and effectively included by applying the symmetry operations to the calculated diffraction pattern.

Though simple, this algorithm is robust to the complex variations of the diffraction intensities with tilt angle. Especially convenient is the hierarchical nature of this algorithm. Each sampling grid can also be used to calculate tilt-averaged diffraction patterns for smaller tilt spreads, ie. the grid used to compute the Nth iteration for σ_θ is the same to compute the (N-1)th iteration for $\frac{\sigma_\theta}{2}$. This property allows us to compute a library of tilt-averaged patterns with varying σ_θ largely in parallel, with additional iterations applied to the successively smaller tilt spreads once the larger tilt spread calculations are converged (again to R $< 1\%$). Using this library, we can build an interpolated model with which to refine the tilt spread if not precisely known.

Also in these calculations, $p(\theta)$ is approximated as a circularly symmetric Gaussian distribution. For a given σ_θ, the sampling grid spans from -$3\sigma_\theta$ to $3\sigma_\theta$. Points located more than $3\sigma_\theta$ from the center are set to zero to maintain circular symmetry. In this way, $\approx 99\%$ of the Gaussian volume is sampled. In addition, the symmetry of the crystal allows to reduce the number of samples. For instance, if sample is oriented along a zone axis of the crystal which exhibits 2-fold rotational symmetry, then only one quadrant of the sampling grid is required: the rest can be accounted for by simply applying the 2-fold rotational symmetry to the computed diffraction patterns. Or, if the sample is oriented along a 4-fold symmetry axis, then only 1/8 of the grid is required.

The sample tilt in each iteration is implemented by applying the Fourier shear theorem to the propagation operator, as follows[13]:

$$\psi_{p+1}(\mathbf{q}) = \psi_p(\mathbf{q})e^{-i\pi t(\lambda|\mathbf{q}|^2+2(tan(\theta_x)q_x+tan(\theta_y)q_y)} \tag{2.25}$$

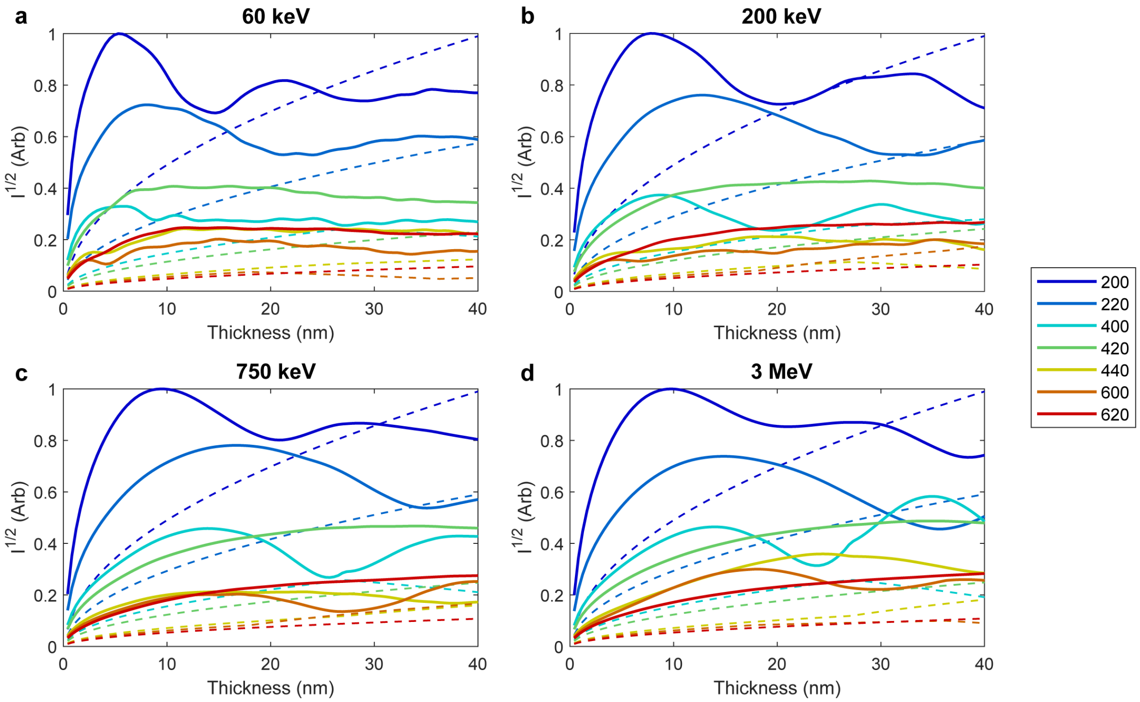

Figure 2.9: Simulated thickness dependence of the square root of diffracted beam intensities for four selected kinetic energies through a rippled ($\sigma_{theta} = 100$ mrad), single-crystal gold film.

This allows to sample arbitrary tilt angles without changing the electrostatic potential slices. Prior works have noted this approximation introduces error at angles beyond 1 degree[13], while freestanding films studied in UED commonly have on the order of 5 degrees RMS tilt spread. So, while this approximation is invoked here, future works should seek to implement approaches that improve accuracy for larger tilt spreads[27, 28].

The behavior of the diffraction peak intensities for a rippled gold foil oriented along [001] as a function of thickness is illustrated in Figure 2.9. The film rippling does smooth out some of the oscillations as compared to those observed in the flat foil. That said, the intensities still differ dramatically from those predicted by the kinematical model within several nanometers. This is again illustrated by the thickness dependent R factor, shown in Figure 2.10. Higher beam energies show improved agreement at low thicknesses, but still have the same issue, and there is minimal gain to be had once relativistic energies are reached. So, the dynamical model is still necessary to accurately match experimental patterns even with large rippling.

2.4 Quantification of lattice temperature dynamics in single-crystal gold films

In this section, the utility of these multislice calculations for quantitative matching and analysis of experimental UED patterns is demonstrated. The example here is quantification of photoinduced lattice temperature dynamics in ultrathin single-crystal gold foils. Accurately tracking the lattice temperature during UED measurements is important for several reasons. For one, the final equilibrated temperature rise provides a measure of the excita-

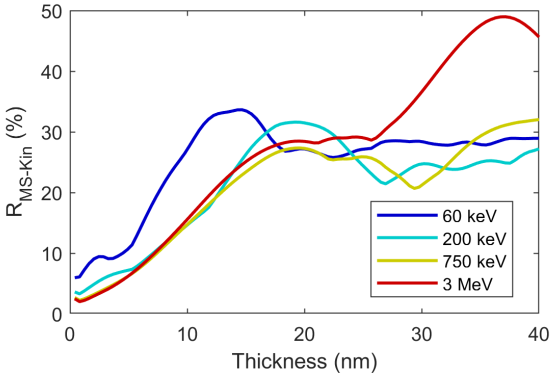

Figure 2.10: Difference between multislice and kinematical diffraction patterns of a rippled (σ_{theta} = 100 mrad), single-crystal gold film for four selected beam energies. The R factor of the first seven diffracted orders is the depicted metric.

tion density used, which could inform whether induced dynamics are thermal or athermal. Also, the time-dependence informs about the energy flow dynamics in the system, and likewise the timescale of temperature rise could indicate whether observed structural behaviors are thermally or athermally driven. Further, accurate lattice temperatures are needed to accurately retrieve intralayer electron-lattice coupling constants as well as defect scattering constants and interfacial scattering and thermal conductivity. In this example, we find that a dynamical treatment is necessary to accurately match observed diffraction signals, and that naive application of the Debye-Waller factor leads to large errors in the measured lattice temperatures.

2.4.1 Matching static UED patterns

As a first test of the applicability of the multislice calculations, a library of diffraction patterns was computed for gold at room temperature ($u^2 = 0.026\,\text{Å}^2$[29, 30]) using both kinematical and multislice models, and then quantitatively matched to a static UED pattern recorded experimentally. The experimental reference pattern shown in Figure 2.11a was recorded using the HiRES UED beamline with 750 keV electron pulses over a single-crystal gold foil from Ted Pella. The diffraction peak intensities for the first seven diffraction orders were extracted by Gaussian peak fitting of the complete Friedel pairs; Peaks recorded without a corresponding Friedel pair were not included to minimize possible errors from misorientation relative to the zone axis.

The agreement between simulations and experiment is illustrated in the R factor maps shown in Figure 2.11b-c. Remarkably, the multislice calculations achieve a tenfold reduction in R factor, yielding an R of 2% at the optimal thickness and rms tilt spread compared to an R of 20% obtained with kinematical models. Furthermore, the optimum parameters are physically reasonable: a thickness of 13.5 nm is in good agreement with the 11 nm quoted by Ted Pella, and the large 105 mrad rms tilt spread is consistent with the optically visible wrinkling of the freestanding film and is in the range of values I have extracted from AFM topography maps for other freestanding single-crystal foils prepared on TEM grids. It is

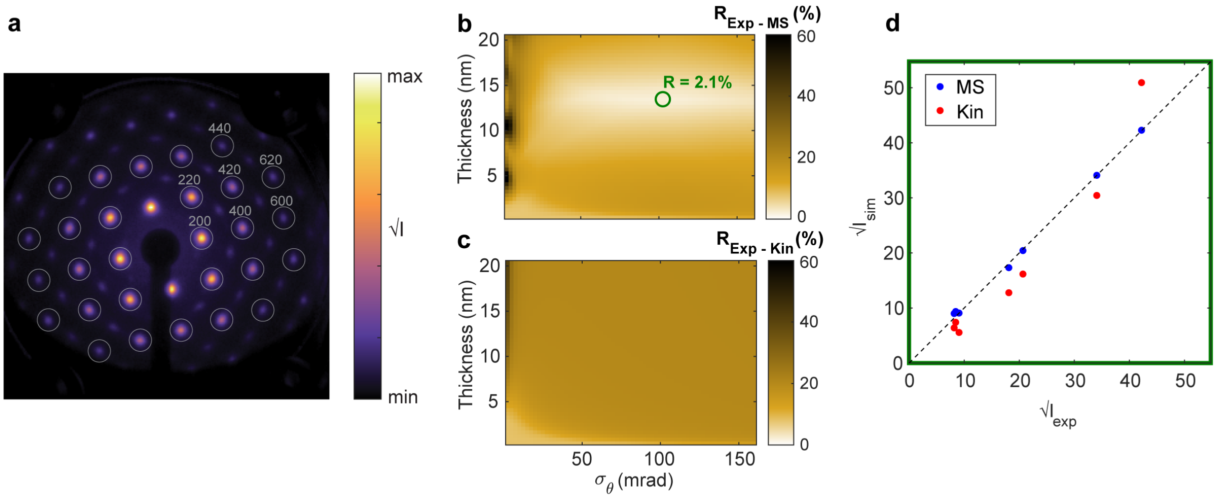

Figure 2.11: Quantitative matching of diffraction simulations to a static UED pattern from single-crystal gold at 750 keV. **a** Experimental pattern labeled with the diffraction orders studied. **b-c** R factor between simulated and measured patterns as function of crystal thickness and rms tilt spread (σ_θ). **d** Scatter plot of the best-fit simulated and measured intensities: points closer to the dashed line ($\sqrt{I_{sim}} = \sqrt{I_{exp}}$) are a better fit.

worth noting that the R factor for the multislice calculations is only weakly dependent on tilt spread beyond 5-10 mrad rms after many of the dynamical effects have already been smoothed out.

The difference in agreement for the best-fit thickness and rms tilt spread are detailed further in scatter plots of the simulated vs measured intensities shown in Figure 2.11d. Notably, the diffracted intensities predicted by kinematical model show larger intensity differences between weak and strong peaks than experimentally measured. This can be because multiple scattering effects tend to level out the intensity distribution somewhat as more intense diffracted orders are more likely to be scattered to weaker orders than the other way around. By evolving the full Schrödinger equation for fast electrons, the effects of multiple scattering and channeling are included, providing a much more accurate distribution of diffracted intensities.

2.4.2 Matching photoinduced difference patterns

Having demonstrated improved matching of the static UED pattern, multislice simulations were then performed with varying thermal displacement parameters to elucidate the temperature dependence of diffraction peak signals and, ultimately, to retrieve the photoinduced lattice temperature. As an example, the simulated diffraction intensity changes for $\Delta u^2 = 0.014$ Å^2 and $\sigma_{theta} = 100$ mrad for a range of film thicknesses are shown in Figure 2.12. The black dashed line marks the kinematical Debye-Waller factor prediction. For a film only one unit cell thick, the simulated changes follow the Debye-Waller factor. However, even within just a few nm, the simulated changes deviate significantly from this prediction. Wide variations in changes between diffraction orders develop, to the point that at some larger thicknesses, some diffraction orders are predicted to increase in intensity while others

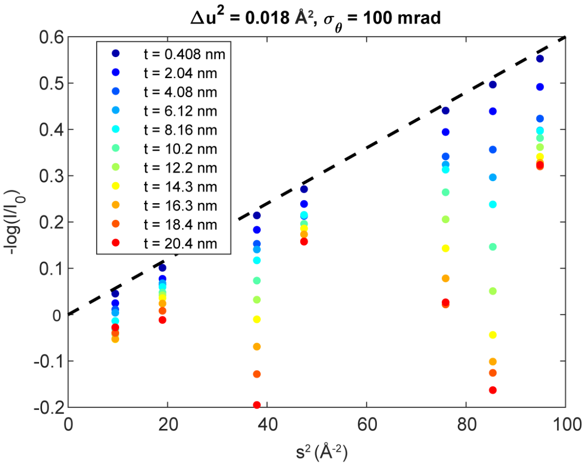

Figure 2.12: Simulated diffraction peak changes induced by thermal atomic motions in rippled single-crystal gold films of varying thickness. The black dashed line is the Debye-Waller prediction for the input $\Delta u^2 = 0.014$, and the dots are changes simulated using the multislice approach.

decrease. Even more important is that the overall shift of diffraction changes to more positive values, such that fitting a line as prescribed by the Debye-Waller model would greatly underestimate the true lattice temperature rise.

Photoexcited UED patterns from the same single-crystal gold film were measured for a series of $\lambda = 1030$ nm pump laser fluences at a 0.5 kHz repetition rate. At each fluence, UED patterns were recorded as the pump-probe delay, Δt, was scanned from -17.3 to +56.0 ps using 6.67 ps steps. A coarse sampling was used in these measurements with a focus on extracting fluence-dependent temperature rise rather than the fine temporal dynamics, which were studied in later measurements (see the next section). The average difference pattern recorded after the arrival of laser pulses with 6.3 mJ cm^{-2} (from +22.5 to +56 ps) is shown in Figure 2.13a as an example. The coherent Bragg diffraction peaks are generally suppressed and the diffuse scattering background generally increases as expected for an increase in incoherent thermal motions. However, the primary Bragg peak changes deviate from the scaling of the Debye-Waller Factor: For instance, the 200, 400, and 600 peaks show little change while the 220, 420, and 620 peaks show large changes. Such deviations call for the application of dynamical scattering theory to accurate match the intensity changes and quantify the lattice temperature rise.

The time-dependent diffraction peak intensities were extracted from the UED datasets with Gaussian peak fitting, and average peak intensities before and after $\Delta t = 0$ were obtained by fitting exponential curves for each peak. The change in mean square atomic displacements was then retrieved before and after time zero by fitting the Debye-Waller factor and multislice models. For multislice models, this fit is performed by keeping the thickness and rms tilt spread of the film fixed, and optimizing Δu^2 by interpolating the peak intensities between multislice calculations performed over a discrete set of u^2 values. Both kinematical and multislice models are fit by minimizing the mean square error of $-\log(\frac{I_{hkl}}{I_{0,hkl}})$.

The results of this procedure for the after time zero diffraction intensities are illustrated by Figure 2.13b. Indeed, the intensity changes predicted using the multislice method (di-

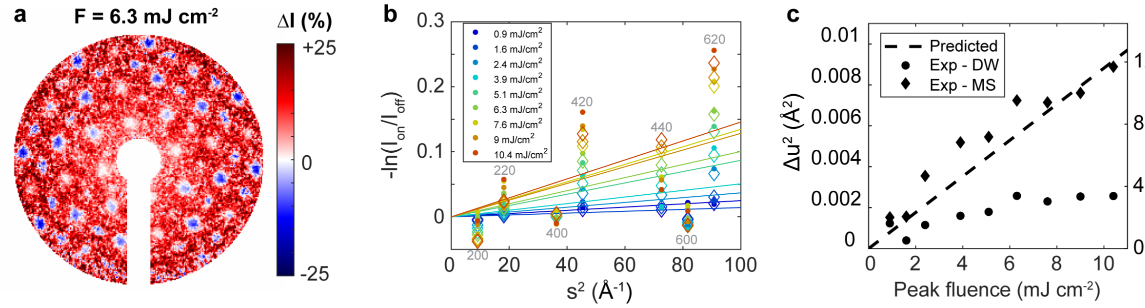

Figure 2.13: Quantifying light-induced lattice heating from UED of single-crystal gold. **a** Example of a photoinduced difference pattern recorded at HiRES using a peak laser fluence of 6.3 mJ cm^{-2}. **b** Photoinduced diffraction changes for varying laser fluences (dots), Debye-Waller factor fits (lines) and multislice model fits (diamonds). **c** Extracted fluence-dependent changes in total rms atomic displacements (Δu^2) and lattice temperature (ΔT) using Debye-Waller (DW) and multislice (MS) models. Estimated changes based on known optical constants of gold are superimposed as a dashed line for comparison.

amonds) are a better match to the observations (dots) than are those predicted by the Debye-Waller model (dashed line), reducing the least-squares residual by about a factor of 3. The variations in intensity change between orders are largely captured by the multislice approach, though differences still remain, perhaps due to differences between the simulated and actual orientation distribution of the sample.

The photoinduced change in mean square displacements and lattice temperature rise are plotted in Figure 2.13c. The relationship between mean square displacements and lattice temperature rise in gold is approximately linear in the studied range of lattice temperatures (about 3.947×10^4 K/ Å^2)[29, 30]. Strikingly, the multislice models retrieve photoinduced lattice temperatures that are about 2.5 times higher than those retrieved using the Debye-Waller factor approach.

Comparing to estimations of lattice temperature rise for the given peak fluence using the known optical constants of gold supports the accuracy of the multislice approach. The lattice temperature rise $\Delta\, T = T_f - T_i$ was calculated by relating the absorbed energy density (ie. in J/mol) U_{abs} to the heat capacity of the material C_p:

$$U_{abs} = F_{inc} A \frac{V_{mol}}{t} = \int_{T_i}^{T_f} C_p(T) \tag{2.26}$$

where F_{inc} is the incident laser fluence, A is the absorbance of the material at the incident photon energy, V_{mol} is the molar volume, and t is the thickness of the film. The absorbance in the 13.5 nm film of $\lambda = 1030$ nm light, using n = 0.153 and k = 6.654[31], was calculated using the coherent transfer matrix method[32] to be 3.7%. Using this and the measured temperature-dependent heat capacity of gold[33], the temperature rise per unit of incident laser fluence was found to be 11.6 K / (mJ cm^{-2}). Fitting a line to the temperatures retrieved with multislice gives a slope close to this of 12.3 K / (mJ cm^{-2}) whereas the kinematical approach gives 4.0 K / (mJ cm^{-2}).

2.5 Conclusions and outlook

Altogether, the calculations shown in this section demonstrate the importance of dynamical theory for quantitative retrieval of atomic motions from UED measurements of single-crystal films, even when using relativistic electron energies. The multislice approach developed here can be applied to a wide range of UED experiments where single-crystal films are examined. For instance, this approach could be used to quantify and separate simultaneous crystal structure change and thermal motions during photoinduced structural phase transformations. It could also be extended to multilayered systems to accurately quantify thermal boundary resistance of the interfaces.

In the long term, the dramatically improved matching of UED patterns could enable retrieval of atomic coordinates from diffraction tilt series, and subsequently allow detailed structure refinement of photoinduced nonequilibrium phases. To recover complete 3D movies of the atomic coordinates and thermal motions in single crystals would mark a major milestone for UED and provide detailed structural knowledge of transient intermediates, metastable phases, coherent lattice responses, and the overall energy flow and structural dynamics.

Chapter 3:

High Repetition-rate Electron Scattering

3.1 Demand for bright relativistic ultrafast electron diffractometers

Over the past 30 years, stroboscopic ultrafast electron diffraction (UED) has emerged as an insightful tool for chemistry and condensed matter physics. This technique employs synchronized pairs of laser or other excitation pulses and electron probe pulses to record a time series of electron diffraction patterns following a stimulus. Since electron diffraction provides detailed information about the atomic structure of a specimen, UED records the evolution of atomic structure over femtosecond timescales. This has been applied to study a range of phenomena including excited carrier thermalization, electron-lattice coupling mechanisms, coherent phonon generation, light-induced phase transformations, and formation of nonequilibrium structures.

Throughout these three decades, scientists around the world have made remarkable developments in the design of UED instruments, continually accessing new frontiers of experimentation and uncovering new dynamic phenomena. The first transmission ultrafast electron diffractometer was demonstrated in 1992 by Prof. Ahmed Zewail's group at Caltech to capture dynamics of gas-phase chemical processes[34, 35]. This setup generated 19 keV electron probe pulses with $< 10^4$ electrons from flat gold photocathodes at 30 Hz repetition rate and attained ≈ 10 ps temporal resolution. Several minutes of integration were needed to record one diffraction snapshot. Several generations of kV UED instruments in reflection and transmission geometries followed with increasing temporal and spatial resolution as well as repetition rate[36, 37], but were generally limited to ps-scale temporal resolution and around $10^4 - 10^5$ electrons per pulse due to space charge-induced broadening.

In 2003, Siwick et al. demonstrated a compact 30 keV UED system which achieved both 10^4 electrons per pulse and sub-ps temporal resolution by positioning the sample holder 4.2 cm from the end of the accelerating gap to avoid space charge effects. With this configuration they recorded a single-shot diffraction time series of photoinduced melting of polycrystalline Al [38]. Further innovations would push the technique to achieve higher bunch charge and shorter pulse durations: for example, the introduction of radiofrequency compression in keV guns to achieve sub-100 fs pulses with 10^6 electrons per pulse [39, 40].

Another breakthrough was modifying a transmission electron microscope with laser entry ports to enable photoemission of 100-200 keV single electron pulses with sub-ps duration at hundreds of kHz to MHz repetition rates[41, 42]. The electron pulses produced in this case can have superb transverse coherence on par with static TEMs, but are limited to less than one electron per pulse and require long integration times.

Meanwhile, radiofrequency photoguns were being developed around the world to produce high current pulses for electron accelerator applications, such as free electron lasers[43–

45]. RF cavities permit higher extraction fields than DC guns before dielectric breakdown across the cathode-anode gap, since the high field amplitudes only persist for a short time and then are quickly reversed. Higher extraction fields then lead to more charge per pulse that can be extracted before the fields are counteracted: for instance, in the case of an infinite planar vacuum diode, the Child-Langmuir Law gives the space-charge-limited current density varying as the 3/2 power of the applied field. RF photoguns typically use large, flat photocathodes excited with tens of micron to millimeter scale laser pulses to achieve the high charge per pulse required for accelerator applications. GHz RF is used to attain tens of MV/m extraction fields at the cathode, much higher than achieved in DC instruments.

These RF photoguns soon found application as high flux UED machines. Musumeci et al. used a 3.5 MeV photoinjector to demonstrate relativistic single-shot UED measurements of single crystal gold melting[46, 47]. Researchers at SLAC utilized a 3.68 MeV photoinjector to develop a UED system which is currently the center of a user program[48, 49]. A 2.8 MeV UED system is operating at Brookhaven National Laboratory[50].

However, these RF photoguns have some notable limitations. The main limitation is that they are typically limited to kHz or lower repetition rates. This is because the high frequency, high amplitude RF drives high currents in the conductive cavity walls, leading to significant heating. To avoid overheating, these guns are usually operated in a pulsed mode, with repetition rates limited to a few hundred Hz. It is also worth noting that because flat, large-area photocathodes are typically used, the transverse brightness and coherence of the emitted beams is much lower compared to DC tip emitters.

A few years ago, the APEX gun, developed at LBNL for the LCLS II FEL at SLAC, marked a significant advancement in relativistic RF photoguns: by using lower frequency RF, it was able to operate in continuous wave mode, achieving MHz repetition rates[51]. It operates with 186 MHz RF, using smaller extraction fields of 20 MV/m and yielding lower energy (0.75 MeV) electrons than GHz RF guns. On the other hand, the gun cavity is then much larger (about 1 meter in diameter) and generates less thermal load during operation. A CsK_2Sb-coated photocathode with high quantum efficiency is used to maintain high charge per pulse from high repetition rate drive lasers. So, while lower extraction fields and electron energies lead to reduced peak brightness within a single pulse, the ability to operate at higher repetition rate provides an advantage in the average brightness.

The High Repetition-rate Electron Scattering (HiRES) beamline employs the bright, high-current pulses of the APEX gun for scientific experiments, including UED. High average brightness permits resolving weak diffraction signals associated with small structural perturbations, such as charge density wave and other superstructures found in quantum materials as demonstrated in Chapter 2. It also permits formation of collimated, nanoscale probes for ultrafast nanodiffraction as demonstrated in Chapter 5. When other sources of noise are mitigated, it provides a path towards resolving finer variations in diffracted signals. In this chapter, details of the pump-probe UED setup at HiRES and initial demonstrations are presented which show the ability to perform high repetition rate pump probe experiments.

3.2 HiRES beamline design and specifications

3.2.1 Electron beamline

The HiRES beamline is designed to generate and deliver relativistic (≈ 750 keV) electron bunches with tunable charge, transverse properties, and longitudinal properties at variable repetition rates to enable a broad range of UED experiments. At the low charge limit, the beamline can be configured to generate single-electron, low emittance pulses for high reciprocal space resolution measurements or for nanoprobe experiments (demonstrated in Chapter 5). At intermediate charges, the beamline can be used to perform high signal-to-noise ratio UED experiments of reversible dynamic processes in solids and gases. At the high charge limit, the beamline can be used for single-shot UED measurements of irreversible processes. The range of electron beam parameters accessible using the beamline is summarized in Table 3.1.

Table 3.1: Typical operational parameters for HiRES

Parameter	**Value**
Beam energy	700-900 keV
Repetition rate	single shot → 1 MHz
Bunch charge	1-10^8 electrons per pulse
Bunch length	100-1000 fs
Momentum Resolution	0.1 $\mathring{A}^{-1}$
Transverse coherence length	~ 10 nm
Spot size at sample	$50 - 500\ \mu$m
Momentum transfer range (s)	$\pm 10\,\mathring{A}^{-1}$

The versatility of the machine is enabled by the application of the state-of-the-art APEX CW RF photogun as well as the flexibility of the overall beamline design. Rapid acceleration to relativistic energy and radiofrequency compression to mitigate space charge broadening permits use of an $\approx$4.5 meter long beamline, in which a variety of electromagnetic lenses and apertures are available for electron beam manipulation and collimation. Photographs of the electron beam paths annotated with some of the key elements are shown in Figure 3.1.

Temporally stretched 515 nm laser pulses are directed to the front of the CsK_2Sb-coated photocathode, from which emitted photoelectrons are rapidly extracted and accelerated to relativistic energy using 20 MV/m RF fields. Shortly after, an RF bunching cavity imparts a time-energy correlation which compresses the electron bunch as it propagates through the beamline, coming to a longitudinal focus at the sample plane. The optimal parameters of

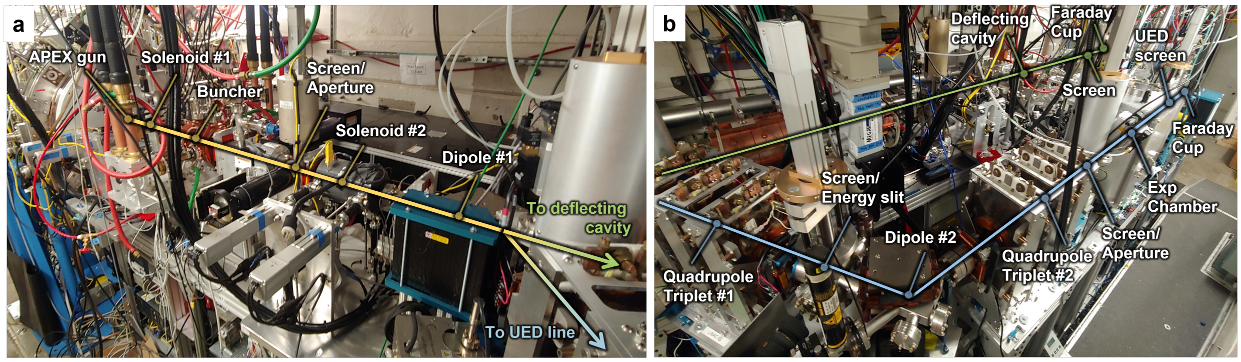

Figure 3.1: Photographs of the HiRES beamline with annotated components as utilized for the experiments in this work. **a** Initial electron beam path out of the gun. Dipole 1 can be set to send the beam down either of two paths. **b** UED experiment path (in blue) and deflecting cavity path (in green) for bunch length characterization.

the bunching cavity depend strongly on operating conditions including initial pulse duration and charge.

Beams are then directed through an initial aperture (0.5 mm) to filter out dark current generated by field emission via the high amplitude RF. After this, the beams can be directed along either of two beamlines. The straight line, originally developed for characterizing the transverse and longitudinal properties of bunches emitted by APEX, continues to serve this purpose for HiRES particularly for longitudinal characterization. An RF deflecting cavity imparts a time-dependent transverse momentum which streaks the beam horizontally at the final screen, enabling measurement of the beam temporal profile. This allows direct measurement and optimization of the electron beam pulse length. A sample chamber is also installed on this line which could be employed for future scientific studies, such as streak camera-based UED as has been explored and demonstrated previously at other facilities[52, 53].

The dogleg guides the electron beam to the UED experiment line. This dogleg path disperses the beam in energy due to the energy dependence of the bending in the dipole, enabling characterization of the kinetic energy distribution of the electron beam at the installed screen. A triangular slit can also be inserted there, permitting energy collimation. Two quadrupole triplets manipulate how the transverse beam properties evolve, and can be used to optimize the probe shape and size at the sample as well as the detector. A second aperture is typically inserted after the second quadrupole triplet to further filter dark current and spurious x-rays, and in some cases to collimate the beam to achieve smaller spot size or improved q resolution.

The experimental chamber is where samples are mounted and positioned for pump probe UED studies. It is a 0.412 m x 0.284 m x 0.429 m chamber with windows for laser entry, laser exit, and optical sample viewing as well as a door for sample exchange. The large volume and optical breadboard base allow the chamber to be readily configured for a variety of experiments: Configurations for room temperature solid-state, cryogenic solid-state, gas-phase, and nanofocusing experiments have all been demonstrated so far, and numerous other

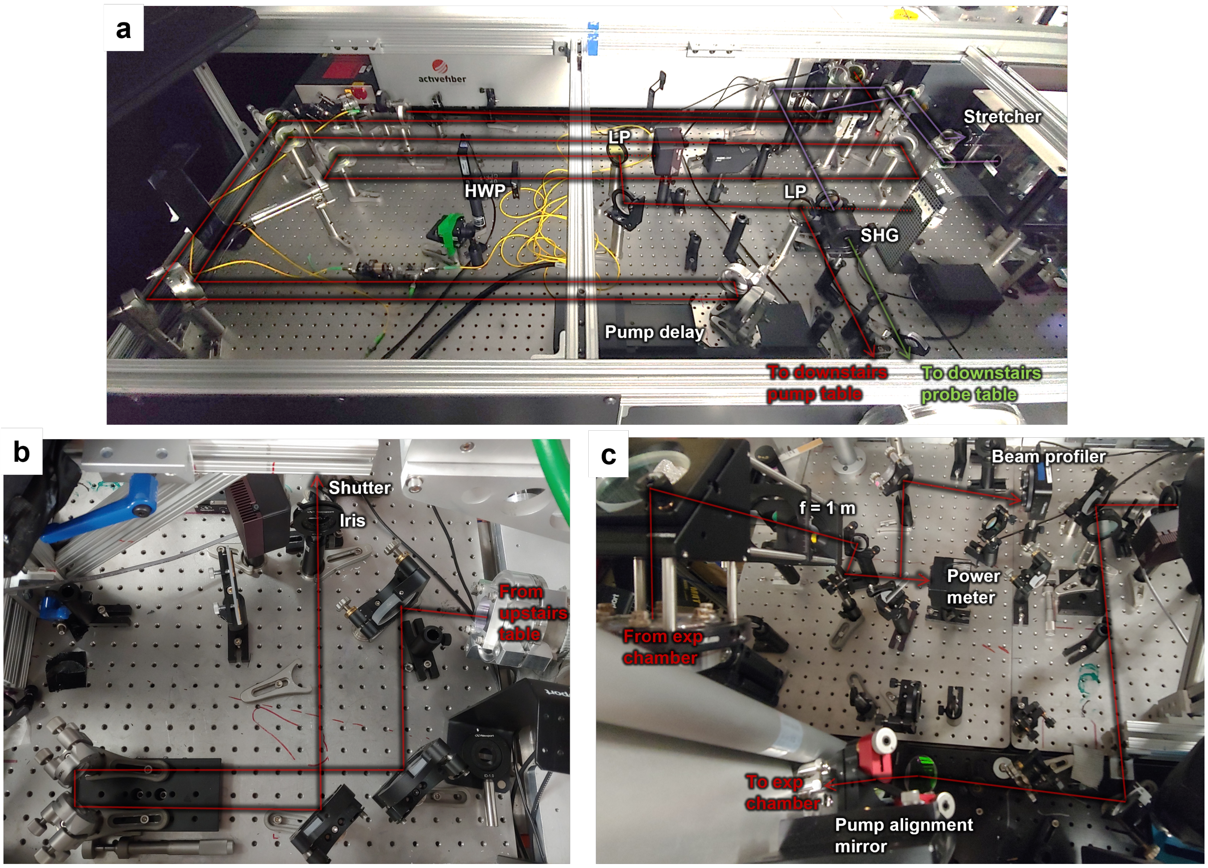

Figure 3.2: Laser paths at HiRES. **a** Upstairs laser table for pump and probe. LP = linear polarizer, HWP = half wave plate, and SHG = second harmonic generation crystal. Red line represents the pump path, purple represents initial probe line, and green represents upconverted probe. **b** First part of downstairs pump laser table. **c** Second part.

configurations have been proposed for future experiments.

3.2.2 Pump laser configuration

A commercial Ytterbium-based femtosecond fibre laser system is used to generate the synchronized pump and probe pulses. The essential parameters of the optical setup are reported in Table 3.2. A train of 315 fs laser pulses centered at 1030 nm (1.2 eV) deliver a power of 50 W at 250 kHz thus providing high pulse energies on the order $\approx 200\ \mu$J.

Initial laser preparation occurs within a dedicated laser hutch (Figure 3.2a). Pump pulses are directed to a retroreflector on a motorized delay stage with ≈ 160 mm of travel, providing an ≈ 1 ns temporal range. The pump pulses are directed through a motorized half wave plate and reflected from a polarizing beamsplitter to allow automated control of the pump pulse energy during experiments, such as for performing excitation fluence scans.

The pump beam is then transported to an optical table next to the sample chamber (Figure 3.2b-c). Lenses can be added and adjusted to achieve a range of spot sizes, typically in the hundreds of μm range to ensure uniform excitation within the electron probe. The

Table 3.2: Laser Parameters

Parameter	Value
Central wavelength	1030 nm
Repetition rate	0.01 - 250 kHz
Pulse energy	$\leq 200\ \mu$J
Pulse duration (FWHM)	$\approx$ 315 fs
Beam size at sample	200-1000 μm
Maximum optical delay	1 ns

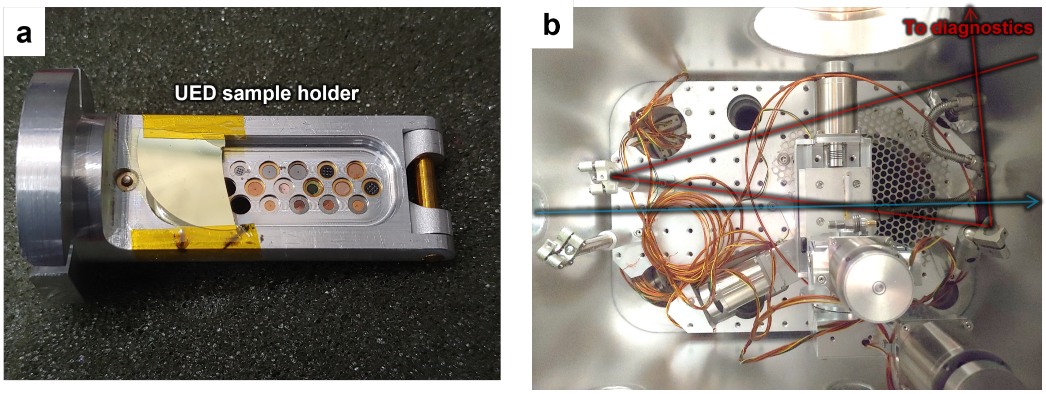

Figure 3.3: UED sample holder and experimental chamber. **a** Room temperature sample holder. **b** Experimental chamber. Red line represents the pump path, blue represents the electron path.

present configuration without a lens produces a 273 μm x 415 μm FWHM spot at the sample. With upwards of 110 μJ per pulse at the sample achievable, This allows peak excitation fluences greater than 60 mJ cm^{-2}.

The pump laser enters the chamber through the entry window downstream from the holder, and reflects off a mirror upstream to impinge upon the sample at about 6 degrees relative to the electron beam. Transmitted pump beam is deflected by another mirror out of an exit window to diagnostics, including a power meter and a beam profiler. The transmitted beam is imaged onto the profiler using a 1 m focal length lens, permitting alignment through a sample window, spot size characterization, and real-time monitoring of the pump laser position.

3.2.3 Solid-state sample holders

The room temperature solid-state sample holder is a custom holder with 22 circular slots for mounting 3 mm diameter samples, including TEM grids and silicon chips (Figure 3.3a). A lid with a hinge opens to exchange individual samples, and is secured with a screw. Samples of varying thicknesses can be secured in the slots by mounting them with 3 mm diameter

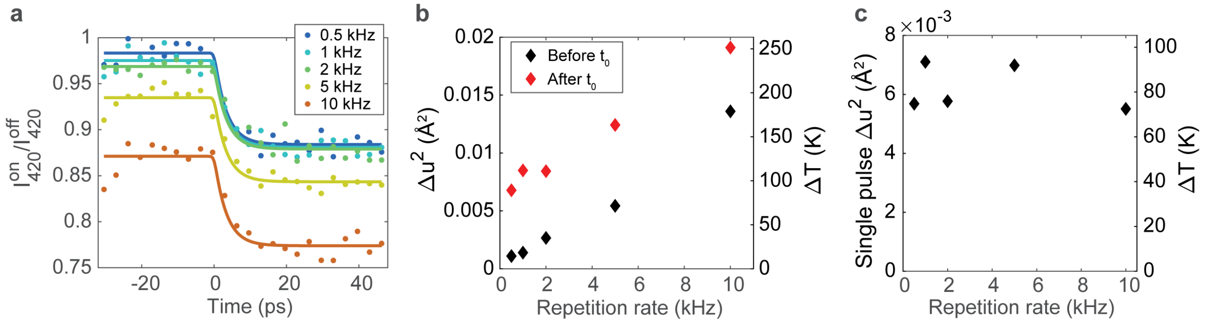

Figure 3.4: Initial repetition-rate dependent lattice heating tests on single-crystal gold films at HiRES. Peak fluence of the $\lambda = 1030$ nm laser was around 3.9 mJ cm^{-2}. **a** Time-dependent 420 peak intensity ratio between laser on and laser off. **b** Extracted lattice temperature rise from fitting the first seven diffraction orders with multislice simulations before and after arrival of the laser pulse (t_0). **c**. Lattice temperature rise due to the single pulse excitation (ie. the difference between the before t_0 and after t_0 lattice temperatures)

washers such that the stack fills the slot depth of ≈ 0.2 mm. During typical operations, a 1 cm x 1.3 cm YAG screen is mounted on one side of the holder for electron beam alignment, leaving 14 slots available for TEM samples.

Motorized stages enable sample manipulation with four degrees of freedom, including horizontal position, vertical position, horizontal rotation, and vertical rotation (Figure 3.3b). The chamber size permits use of wide stages that provide access to the entire sample holder as well as full tilt ranges in horizontal and vertical. The sample holder contains a Nd magnet which connects it to a holding plate on the vertical translation stage. A photodiode is also mounted nearby on the plate for pump and probe timing measurements.

A closed-cycle liquid helium cryostat with custom sample holder provides an alternative configuration, enabling cooling of solid state samples to below 10 K in under 3 hours. Details of the cryostat setup will be published in a forthcoming article.

3.3 Kilohertz-rate UED demonstration on gold

Pump-probe UED measurements of photoinduced lattice dynamics in single crystal gold films were performed at varying repetition rates to both demonstrate the experimental capability at HiRES and examine the utility of high repetition rate for solid-state UED. Freestanding 11 nm single crystal gold films from Ted Pella were examined in these measurements. Laser pulses with λ of 1030 nm were used to excite the material at a fixed peak fluence of 3.9 mJ cm^{-2} and spot size of 639 μm $\times$ 734 μm FWHM. A coarse time delay scan using 6.67 ps steps was performed at each repetition rate, and 25 diffraction frames were recorded and averaged at each step. Gaussian peak fitting was used to extract the time-dependent diffracted intensities. Multislice models as described in Chapter 2 were then fit to the first seven diffraction orders to extract the lattice temperatures.

The measured dependence of lattice temperatures on repetition rate is summarized in Figure 3.4. As the repetition rate increases, the time between pulses is proportionally reduced and the average power absorbed by the sample proportionally increases, leading to increased cumulative heating of the material. This can be observed in the time-dependent 420 peak intensity (Figure 3.4a) as peak suppression is still observed before the arrival of the next laser pulse. The cumulative heating leads to an overall offset of the diffracted intensities, ie. an increased initial temperature. The lattice temperature rise before and after (Figure 3.4b) shows a roughly linear increase of initial lattice temperature with repetition rate, reaching a condition at 10 kHz where the cumulative temperature rise is roughly equal to the temperature rise induced by a single pulse. It is worth noting that the single pulse temperature rise does not change with repetition rate (Figure 3.4c), showing that the sample is not damaged in the excitation conditions studied here.

The effects of cumulative heating in freestanding thin films can be understood by considering the solution to the 2D heat equation:

$$t_r \propto \frac{\sigma_{abs}^2}{\alpha}(\frac{T_0}{T_f} - 1) \tag{3.1}$$

where t_r is the relaxation time, T_0 and T_f are the initial and photoexcited temperatures, α is the thermal conductivity, and σ_{abs} is lateral size of the absorbing region. While significant cumulative heating was observed at a few kHz in these initial demonstrations, this is largely because the films were more than 1 mm wide and were excited with a large laser beam width. For such large films, the higher repetition rate is not needed to achieve high fidelity patterns anyway. On the other hand, smaller flakes of material that are normally more difficult to resolve would also absorb less power and allow faster heat dissipation, permitting use of higher repetition rates.

Chapter 4:

Light-induced structural switching in $TaTe_2$

*Part of the work presented here is based on an article published in *Communications Physics* [16].

4.1 A family mystery

Once pump-probe UED at HiRES was demonstrated in 2019 and the 10K cryostat was commissioned, it became imperative to employ these new capabilities for scientific exploration. Several quantum materials were considered, but $TaTe_2$ stood out and was ultimately selected for the first detailed scientific study. Among the layered Ta-based dichalcogenide family, $TaTe_2$ tends to be overshadowed by its brethren TaS_2 and $TaSe_2$, which are renowned for their rich polytypism including numerous charge density wave and superconducting phases leading to widely tunable electronic properties. Yet, $TaTe_2$ is interesting and unique in its own right: isostructural to $NbTe_2$ and $NbSe_2$, it forms Ta trimers along one axis in an ABC stacking order, forming an intricate monoclinic crystal structure. Furthermore, when it is cooled below room temperature, additional Ta clustering emerges perpendicular to the trimers. Contrary to charge density order in TaS_2 and $TaSe_2$, emergence of this trimer superstructure leads to an increase in conductivity. Optical manipulation could illuminate the role and characteristics of electron-lattice coupling in this order as well as provide a means to control the material properties.

This chapter describes the first time-resolved UED experiment on 1T'-$TaTe_2$, in which a picosecond-scale light-induced melt-recovery process for the cryogenic order was recorded and characterized. It was found that excitation with 1.2 eV photons could drive melting of the low-temperature order on a $\approx$1.4 ps time scale followed by recovery several picoseconds later into a heated form of the initial phase. Density functional theory calculations hint that a direct optical melting of the bonds may be partly responsible for the initial melting, and so the intial superstructure recovers upon thermalization. These results are published in ref. 16, and further details can be found there in the article and corresponding supplementary information.

4.2 Crystal structure and signatures of structural phase transition

Figure 4.1a illustrates the crystal structure of $TaTe_2$ in its low-temperature (LT) phase. Triple-layer sheets of covalently bonded Ta and Te atoms are separated by weaker van der

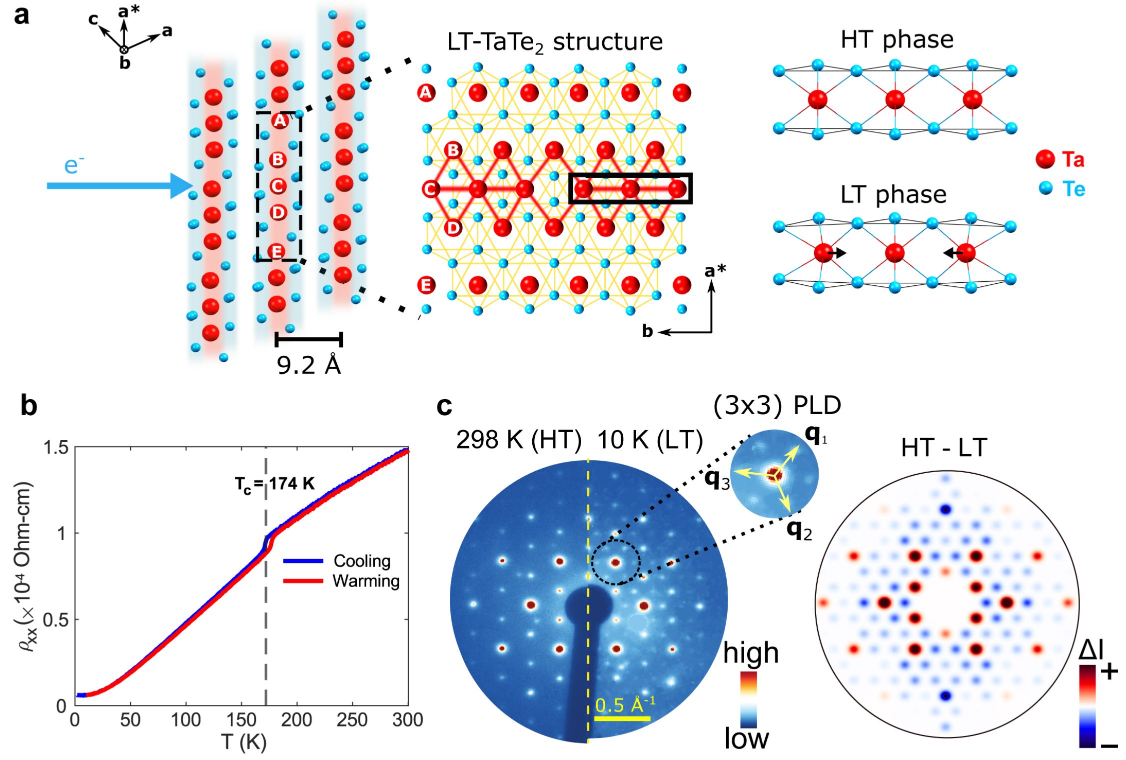

Figure 4.1: Temperature dependent structure and resistivity of TaTe$_2$. **a** Layered crystal structure of the low temperature phase of 1T'-TaTe$_2$. The electron beam is incident perpendicular to Ta and Te planes in the UED experiments. The a, b, and c lattice vectors shown are those of the monoclinic unit cell. The projection perpendicular to the dashed region is indicated. Black box: Ta trimer clusters forming along the b-axis in the LT phase. Representations of LT and HT phases showing enhanced distortions in the LT phase are presented in the top right. Small black arrows denote the movement of atoms towards the central Ta atom. **b** Temperature-dependent electrical resistivity measured on a bulk crystal in the batch prepared for the UED experiments. **c** Static electron diffraction patterns of 1T'-TaTe$_2$ obtained by 0.75 MeV electron pulses at 298 K (HT) and 10 K (LT) along the [$\bar{1}$01] zone axis. The inset shows the (3x3) PLD satellite peaks that arise in the LT phase. A few additional peaks are present due to diffraction from the Si support frame. The difference pattern between HT and LT phases extracted via peak fitting is shown next to the static patterns.

Waals forces along the stacking direction. Prominent structural elements in this material are Ta trimers —sets of three adjacent Ta atoms in a row that cluster together via enhanced Ta-Ta bonding. Already at room temperature, Ta atoms are ordered in-plane into trimers assembled into double zigzag chains along the *b*-axis, which breaks hexagonal symmetry and forms a three-layer stacking sequence. In the LT phase, additional ordering emerges in the chains along the *b*-axis in the form of trimer clusters. This (3×3) lattice superstructure represents a distorted 1T' polytype with C2/m space group symmetry and a monoclinic unit cell [54]. In this configuration, each Ta atom in the unit cell is coordinated to six Te atoms in a periodically distorted octahedral arrangement.

The aforementioned resistivity drop upon cooling was reproduced in temperature-dependent measurements on the bulk crystals grown for these experiments, shown in Figure 4.1b. The critical temperature of 174 K is consistent with prior measurements of the phase transformation[55]. UED samples were prepared from the bulk crystals by exfoliating until appreciable optical transmission could be observed, then using a custom motorized transfer station built in an optical microscope to perform PDMS stamp transfer onto a SiNx TEM window from Norcada[56]. More details about the preparation and characterization of the 60-nm thick, microscale crystal (flake) studied are available in the published article[16].

Figure 4.1c shows equilibrium diffraction patterns of a 1T'-TaTe$_2$ flake which were measured with the 0.75 MeV electron bunches at HiRES, comparing the high-temperature (HT) phase at 298 K and LT phase at 10 K. As illustrated in Fig. 4.1a, the electron beam impinges along the $[\bar{1}01]$ zone axis, i.e. perpendicular to the Ta and Te layers. The measured diffraction patterns exhibit a large number of Bragg spots reaching up to high momentum transfer, demonstrating both a high sample crystallinity and a large scattering range afforded by the relativistic beam energy. It should be noted that the diffraction pattern here has two-fold symmetry, unlike the six-fold symmetry present in many other layered transition metal dichalcogenides.

The pattern at 10 K reveals the appearance of new satellite peaks surrounding the main lattice peaks as a result of the emergent (3×3) periodic lattice distortion (PLD), in concordance with Ta trimer cluster formation and the associated unit cell tripling [55, 57–59]. Their observation also demonstrates that the transverse coherence length of the electron source is sufficient to track the dynamics of the LT superstructure.

To determine the signature in the electron diffraction patterns attributed to the structural phase transition, we calculate the difference between HT and LT patterns following normalisation by the total electron intensity. The resulting changes are shown in Fig. 4.1c. While all superlattice satellites associated with the (3×3) trimer superstructure are suppressed, the main Bragg peaks exhibit a mixture of positive and negative intensity changes. This complex response deviates from observations in TaS$_2$ and TaSe$_2$ where all primary Bragg peaks increased in intensity, opposite to the suppression of the PLD satellites [60, 61]. This positive-negative intensity change signature is due to the symmetry of the superstructure formation within the distorted monoclinic unit cell, which leads to mixed structure factor changes for different diffraction orders.

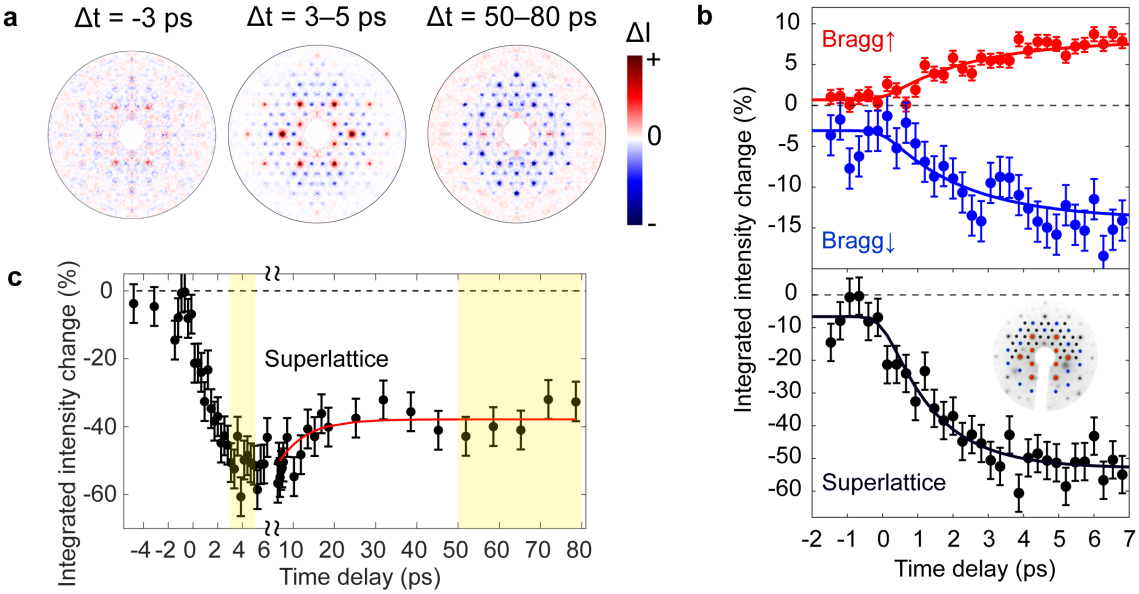

Figure 4.2: Ultrafast electron diffraction of $\mathrm{TaTe_2}$. **a** Photo-induced changes in the diffraction patterns, for selected time delays. The patterns have been symmetrised for visualisation purposes only. For improved signal-to-noise the latter two are calculated by averaging difference patterns over time ranges, i.e. 3–5 ps for early and 50–80 ps for late time delays. **b** Temporal evolution of the signals from the main lattice Bragg peaks, separately for the increasing and decreasing subsets, and of the LT superlattice peaks. Solid lines: fits with an exponential function convolved with the time resolution of 0.75 ps, up to 7 ps delay time. The corresponding time constants are $\tau_{\mathrm{PLD}} = 1.44 \pm 0.27$ ps, $\tau_{\mathrm{Bragg}\uparrow} = 2.44 \pm 0.81$ ps and $\tau_{\mathrm{Bragg}\downarrow} = 2.25 \pm 1.34$ ps. **c** Dynamics of the PLD satellite peaks over an extended time scale. Yellow shading indicates time ranges that were averaged to generate the difference images. A partial recovery is observed, fit with an exponential relaxation with offset (red line) with time constant $\tau = 6.6 \pm 2.6$ ps. The long-lived suppression indicates that the lattice system has thermalised at an elevated temperature. Error bars in the data indicate standard error calculated using the distribution of laser-off signals compared to the mean laser-off signal over the course of the measurement.

4.3 Ultrafast optical melt and recovery of trimer clusters

We then performed the pump-probe UED measurements. The sample was first cooled into the low-temperature ordered phase at 10 K, and then photo-excited with near-IR femtosecond pulses (1030 nm wavelength). Electron diffraction patterns were then recorded with and without excitation at each pump-probe time delay to measure the time-dependent photoinduced structural change.

Difference maps of the diffraction intensity at selected time delays Δt are shown in Fig. 4.2a for a pump fluence of 2.3 mJ cm^{-2}, indicating structural changes on a picosecond timescale. For clearer visualisation, these maps are symmetrised by averaging signals across the vertical and horizontal mirror plane symmetries. At negative time delays, a small signal is observed which may be due to slight accumulated heating of the crystal under the 500 Hz laser excitation, but it is much smaller than the changes that follow.

During the first couple of picoseconds following arrival of the laser, the signals exhibit a characteristic pattern of changes, including a decrease of the (3×3) PLD satellites and a mixture of increased and decreased intensities of the main lattice Bragg peaks. The difference pattern averaged from 3-5 ps strongly resembles that of the HT-LT phase transition obtained from the equilibrium data in Fig. 4.1a. This indicates that the intense near-IR excitation induces a melting of the low-temperature trimer clusters and an ultrafast phase transition to the (3×1) ordered HT state in $\mathrm{TaTe_2}$.

Following the melting of the trimer clusters, further structural dynamics ensues that is marked by the recovery of the (3×3) superstructure due to lattice thermalisation. At these later times, the signature of the phase transition disappears and the pattern recovers the LT superlattice. The broad overall reduction of the peak intensities in this time range is that expected of a heated state with incoherent thermal atomic motions via the Debye-Waller effect [61, 62].

The structural kinetics were extracted in more detail by fitting all peaks for each time-delayed UED pattern, summing the photo-induced changes of specific subsets for optimal signal-to-noise. Figure 4.2b plots the early-time dynamics of the set of lattice Bragg peaks exhibiting an intensity increase (Bragg↑) or decrease (Bragg↓) in the pattern, as well as the changes of the superlattice satellites. Normalised to their intensities before excitation, the PLD satellites undergo ≈55% suppression with a time constant of $\tau_{\mathrm{PLD}} \approx 1.4$ ps. This time constant provides a measure of the (3×3) trimer superstructure melting time in $\mathrm{TaTe_2}$ in our experiments. We note this is likely preceded by a faster electronic melting time which we cannot access here, but could be a subject of future spectroscopic investigations [63].

Alongside the PLD suppression, the primary lattice Bragg peaks also exhibit strong changes with slower dynamics corresponding to time constants of $\tau_{\mathrm{Bragg}\uparrow} \approx 2.4$ ps and $\tau_{\mathrm{Bragg}\downarrow} \approx 2.3$ ps. The underlying diffraction orders show comparable dynamics. Moreover, an oscillation seems to appear in the Bragg↓ trace, with a period of ≈2 ps. While this may be linked to excitation of coherent phonons, the ≈0.5 THz frequency does not match vibrational modes identified by theory (see supplementary info for the published article). The lack of a similar feature on the Bragg↑ curve does not rule out a coherent phonon origin. However, the error bars in the Bragg↓ trace are larger due to its weaker constituent high-q peaks and the fluctuation is comparable to measurement error. While beyond the scope

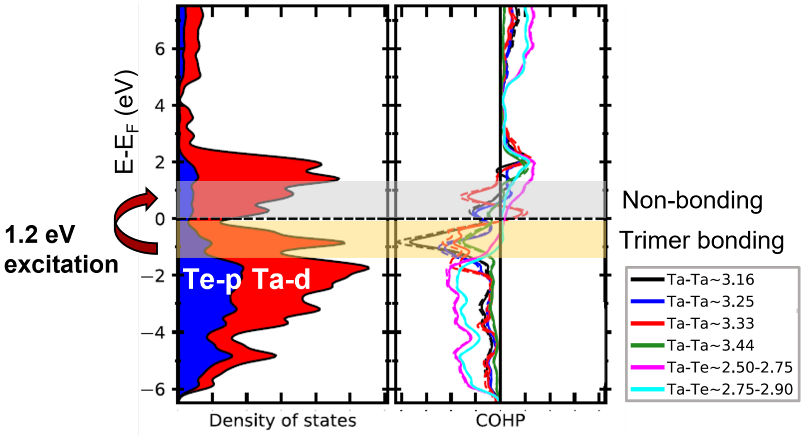

Figure 4.3: A possible pathway for direct melting of Ta-Ta bonds illuminated by first-principles calculations. DFT-calculated density of states projected onto Ta and Te atoms is shown at left. Crystal orbital Hamilton population (COHP) calculations of the projections onto various bonds in the crystal are shown at right. The 3.16 Å Ta-Ta bonds are the tightest bonds in the LT Ta-Ta clusters. Optical promotion from bonding to non-bonding Ta orbitals with 1.2 eV photoexcitation is schematically depicted.

of our present work, future investigations are warranted to clarify the presence of coherent lattice motion. We also note that at negative time delays, a few-percent intensity reduction is observed in both the superlattice and Bragg↓ peaks which we attribute to residual heating accumulated over several laser pulses.

The overall dynamics, including the recovery, are shown in Fig. 4.2c. The suppressed trimer order recovers ≈ 20% of the original intensity with a ≈ 7 ps time constant. We note that this timescale may be influenced by simultaneous contribution from mechanical buckling. The overall suppression of the diffraction peaks relative to the LT ground state indicates the thermalisation of the lattice degrees-of-freedom into a “hot" (3 × 3) trimer superstructure at longer delays. We can estimate the maximum lattice thermalised temperature due to full thermalisation of the absorbed laser energy. For the given 2.3 mJ cm^{-2} fluence this results in a temperature of 177 K, based on the 1T’-TaTe$_2$ heat capacity [55] and the optical constants we measured of our 60 nm thick flake. We also performed experiments on the same sample at 1.75 mJ cm^{-2} and 1.5 mJ cm^{-2} fluence. The signature of structural phase transition was reproduced for these fluences with reduced magnitude.

The dynamics observed here is summarized by the following steps. Photo-excitation with intense pulses leads to the excitation of energetic carriers and picosecond melting of the low-temperature (3 × 3) trimer superstructure phase. The transient phase that results corresponds to a (3 × 1) trimer chain order, as inferred from the close overlap of the photo-induced change in the diffraction pattern with the fingerprint of the LT-HT transition. In the subsequent picoseconds, the lattice degrees-of-freedom thermalise, enhancing Ta-Ta bonds and thereby switching into a hot (3 × 3) superstructure state. The latter persists for extended times (≫ 80 ps) until thermal diffusion transfers heat into the substrate.

4.4 Mechanistic clues from first principles theory

Density functional theory (DFT) calculations clarified the electronic states involved in the photo-excitation. The projected density of states (DOS) and crystal orbital Hamilton population (COHP) were calculated for the relaxed LT and HT structures of $TaTe_2$, revealing the nature of occupied and unoccupied states, as shown in Fig. 4.3. In the LT phase, the lower-energy region of the valence band (i.e. below -4 eV) consists of Te *p*-states with a small contribution from Ta *d*-states, whereas the upper region of the band (i.e. above -2 eV) has mostly Ta character. Negative COHP values in the upper valence band indicate the bonding nature of Ta trimer states in this energy region. Trimer formation is enabled by partial charge transfer from Te to Ta involving d_{xz} and d_{xy} states which leaves uneven charges on Ta sites and enhanced Ta-Ta bonding [57]. Meanwhile, conduction band states near the Fermi level belong to non-bonding states of Ta trimers, with anti-bonding states lying higher in energy ($\approx$4 eV above E_F).

Optical absorption in 1T'-$TaTe_2$ involves mainly two kinds of dipole-allowed charge-transfer transitions: promoting either Te *p* to Ta anti-bonding states (type-I), or depopulating bonding states while populating non-bonding states of the *b*-axis trimers above the Fermi level (type-II). Photo-excitation around 1.2 eV chiefly involves the latter, which weakens the original charge-disproportionation between Ta sites within these trimers, thus triggering the “melting" of the (3×3) order. The calculations also identified several strongly coupled phonons, including a mode around 2.7 THz involving Te motions and displacements of the Ta ions along the trimer axes that may be set into motion after optical charge transfer excitation. This predicts a cooperative mechanism for photo-induced trimer cluster dissolution in $TaTe_2$, which can be addressed in future diffraction studies with higher temporal resolution and time-resolved diffuse scattering to directly track the phonon modes participating in the transformation.

4.5 Implications for future studies

This study was the first ultrafast time-resolved measurement of $TaTe_2$, utilising short MeV electron bunches to resolve a picosecond atomic-scale melting of its intriguing trimer clusters and the subsequent thermalisation into a hot (3×3) superstructure phase. In these and other MTe_2 systems (where M = transition metal), changes in the lattice structure are linked to anomalous changes in conductivity and magnetic susceptibility. The light-driven toggle and recovery seen here to occur between different lattice symmetries may thus enable applications, e.g. for ultrafast switching. Moreover, the associated trimer dynamics in this material opens the possibility for control of the related electronic modulations in $TaTe_2$ on even faster time scales.

This experiment also demonstrates the utility of the HiRES beamline for ultrafast materials science. Granted, this represents a use case at the lower end of repetition rate (0.5 kHz), as a tens of micron flake was being studied at cryogenic temperature on a thin, low conductivity substrate. Future studies of materials on supports with improved heat sinking or of nanoscale materials with a smaller total absorbed energy can take full advantage of the higher available repetition rates. Still, this first study marks an important demonstration of the capability of the beamline to resolve picosecond dynamics of relatively weak and dense diffraction signals like the superlattice diffraction studied here.

Chapter 5:

Nanoscale probing in RF-based UED

---

*Part of the work presented here is based on an article published in *Communications Physics* [64].

5.1 Room at the bottom for UED

Probing ultrafast dynamics in nanoscale volumes is an important emerging research area. In quantum materials, nanoscale heterogeneity may influence the overall behavior of ultrafast processes. For instance, prior UED studies of photoinduced phase transformations in polycrystalline materials have suggested that grain-dependent threshold fluences and transition dynamics could be present within the probed volume[65]. Furthermore, transient local nanoscale defects in charge density waves have been postulated to contribute to recovery dynamics of quantum materials [66]. The ability to probe local dynamics within specific grains and near defects and interfaces could provide great insight on such processes.

Furthermore, low-dimensional nanocrystals likely host unique, size-dependent photoinduced dynamics and transient structures due to quantum confinement, as they are known to have altered electronic and lattice modes. For instance, carbon nanotubes host a rich interplay of dynamics between intralayer and interlayer lattice modes[67]. Nanowires of strongly correlated quasi-1D materials like $NbSe_3$ show size-dependent inter-chain interactions[3]. The ability to perform UED at the nanoscale could reveal heterogeneous dynamics and access novel phenomena at quantum length scales.

However, reducing the probed area from micrometers to nanometers demands much higher brightness of the electron probe. For a given angular divergence, σ_θ, the maximum achievable diffracted intensity I($\mathbf{s}$) is related to the material's intrinsic electron scattering probability S($\mathbf{s}$), the probed sample area, $\mathrm{A_{sample}}$, and the average transverse beam brightness at the sample, $\mathrm{B_{4D,av}}$:

$$I(\mathbf{s}) \propto S(\mathbf{s}) B_{4D,av} \sigma_\theta^2 A_{sample} \tag{5.1}$$

Where the average transverse beam brightness is given by:

$$B_{4D,av} = \frac{i_{av}}{\epsilon_x \epsilon_y} = \frac{i_{av}}{\sigma_x \sigma_{x'} \sigma_y \sigma_{y'}} \tag{5.2}$$

Where i_{av} is the average beam current, ϵ_u is the transverse emittance along u, σ_u is the rms size, and $\sigma_{u'}$ is the rms angle spread. Due to low transverse brightness, typical sub-kHz MeV-scale UED beamlines operate with tens of μm or larger beams and examine thin film samples of similar size. Now that the HiRES beamline can access kHz to MHz repetition rates, the average beam current, and consequently average brightness, is increased by orders of magnitude, permitting MeV-scale UED probing of nanoscale regions.

In this chapter, two approaches are demonstrated to achieve UED at the nanoscale with the HiRES beamline. The first is illuminating an isolated nanostructure with the full microscale UED beam. The second is using a high-strength magnetic lens to form a nanoscale probe beam. Using the full beam does not require significant modifications to the UED setup, but poses a few challenges on the sample preparation which will be described in the following section. While nanoprobes require more engineering of the beamline, they are ultimately more versatile in both types of experiments that are possible and sample configurations that can be studied. For instance, nanoprobes enable spatiotemporal mapping studies, avoid sampling superfluous substrate and background signals, and permit smaller pump spot sizes which reduces the thermal load on the sample.

5.2 High repetition-rate probing of isolated nanowires

Preparing an isolated nanomaterial sample suitable for pump-probe UED experiments requires several considerations. Firstly, the nanomaterial needs to be mechanically supported to limit motion under laser or electron illumination without imposing undue mechanical strain. Secondly, there must be adequate heat sinking to permit high repetition-rate laser excitation. Thirdly, there should be minimal scattering signals from background materials which could limit the dynamic range recorded and complicate pattern analysis.

In this section, I demonstrate a few approaches for preparing and performing UED experiments on isolated nanowires at HiRES, using VO_2 nanowires as an example. In these examples, Lei Jin from Prof. Junqiao Wu's group would grow the wires and then use a micromanipulator to transfer 100-150 nm diameter wires to my sample platforms, which I would then secure using e-beam induced Pt deposition in a focused ion beam scanning electron microscope (FIB-SEM). I then characterized the nanowires in TEM and recorded UED patterns at HiRES. Each sample mounting approach demonstrated here could be suited for a range of UED experiments which will be discussed.

The single crystal VO_2 nanowires here are studied at an ambient temperature near 300 K. Unstrained VO_2 crystals have been measured to undergo a structural phase transformation from a monoclinic structure (M2) to a tetragonal “rutile" structure (R) when heated above 340 K[68]. This transformation essentially involves melting the dimerization of V-V bonds along the rutile c axis. The dimers double the unit cell along that axis and introduce an incilination to the unit cell since the dimer positions are shifted between adjacent atomic columns. These changes are well illustrated in Figure 1b of ref. 68. Consequently, the M2 phase exhibits additional diffraction peaks as compared to the R phase which can be observed in the diffraction patterns that follow and could be used to track the evolution of light-induced structural transformations.

The first approach is placing the wire on a commercially available SiNx window from Norcada, as shown in the SEM micrograph in Figure 5.1a. In this case a 10 μm x 10 μm window is used with a 20 nm thick SiNx membrane. The SiNx provides some mechanical support, preventing sagging of the wire across the window and also through van der Waal's forces limiting lateral movement. It is optically transparent from the visible to near-infrared, avoiding superfluous absorption of the pump. It also provides some heat sinking, though the thin insulating membrane may not permit sufficient dissipation for high repetition-rate

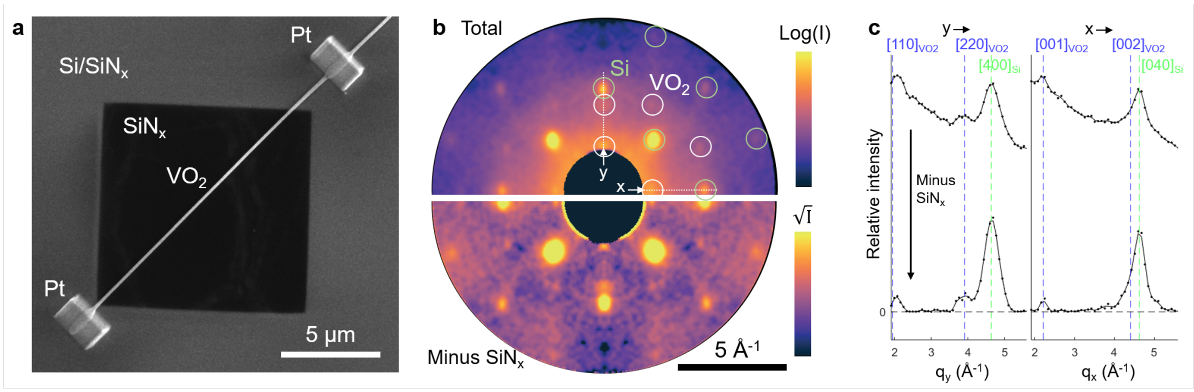

Figure 5.1: Static UED of an individual VO_2 nanowire on a SiNx window at HiRES **a** SEM image of the prepared sample. **b** Diffraction pattern before (top) and after (bottom) isotropic background removal. Si peaks are masked with black circles in the bottom panel. Patterns are symmetrized using the two known mirror planes and Gaussian low-pass filtered ($\sigma = 2$ px) for clearer visualization of diffraction peaks. **c** Line profile extracted from symmetrized, low-pass filtered ($\sigma = 1$ px) pattern before (top) and after (bottom) isotropic background removal. Expected location of the [001] peak based on the measured crystal structure of the room-temperature monoclinic phase is superimposed (blue dashed line). The background-subtracted profile is vertically scaled by 2x for clearer viewing.

pumping.

A UED pattern from this sample recorded at HiRES is shown in Figure 5.1b. The image is an average of 20 frames recorded over 40 seconds total integration time while using 50 kHz repetition rate. Several VO_2 diffraction peaks are resolved, distinguishable from extra peaks from the Si frame as well as isotropic scattering from the amorphous SiN_x removed in the bottom panel. The VO_2 diffraction peak locations are consistent with the reciprocal lattice points known to be visible along the [110] zone axis (using the rutile phase coordinates). The 001 reflection is highlighted in Figure 5.1c, observed at the expected location and distinct from the SiN_x background. This demonstrates the ability of the HiRES beamline to resolve signals from an individual nanostructure in this configuration. However, large amorphous background from SiNx and diffraction peaks from the Si frame hinder the dynamic range, which would make it difficult to resolve small changes to diffraction signals.

For nanowires which undergo structural transformation, there is an additional issue of longitudinal strain imposed by the sample platform. In this case, the VO_2 nanowire was secured at both ends with Pt deposition to mitigate lateral motions of the wire. However, during transformation from monoclinic to rutile phase, these VO_2 nanowires undergo a 1% expansion in length, meaning the Pt patches will impart a compressive strain as the material is transforming. This leads to a significant broadening of the temperature-dependence of the thermal phase transformation, as illustrated in Figure 5.2. This effect would also likely influence the photoinduced phase transition, broadening the fluence-dependent transformed fraction and imparting longitudinal strain waves through the wire. The mechanical constraints of the sample platform should be carefully considered when studying structural dynamics involving large strains.

A second approach to achieve higher signal-to-background ratio is to suspend a free-

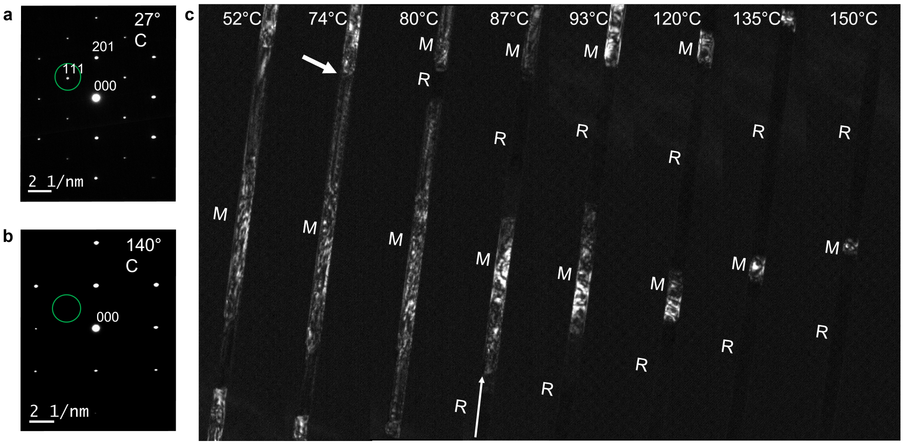

Figure 5.2: In-situ TEM of thermal phase transformation of a VO_2 nanowire prepared on a SiNx window. **a** Diffraction pattern at room temperature with the peak selected for dark field imaging circled in green. **b** The same but above the phase transformation temperature. **c** Temperature-dependent series of dark field TEM images showing the gradual transformation from the low temperature monoclinic (M) phase to the high temperature rutile (R) phase.

standing nanostructure across a gap. This approach has also been used for electrical property measurements of nanomaterials. An example of a VO_2 nanowire across a 50 μm Cu aperture is shown in the SEM micrograph in Figure 5.3a. Again, the nanowire is secured at either end via Pt deposition, but in this case the wire is free to expand (sag) or contract. This accommodates longitudinal strain of the wire after excitation, such as in a structural transformation.

It also allows to acquire high fidelity, background-free UED patterns such as that shown in Figure 5.3b. This was recorded at 50 kHz averaging 100 frames over 40 seconds total integration. This pattern was recorded along the $[2\bar{1}3]$ zone axis which includes some diffraction peaks that disappear upon transitioning from monoclinic to rutile phase and hence could be used to track the structural transition. Several diffraction orders are clearly resolved, again demonstrating the capability of HiRES to record high fidelity patterns of a single nanowire. However, this configuration poses a few challenges for pump probe experiments: absorbed heat must be conducted over long distances across the wire, and the wire is observed to occasionally shift under the electron beam.

A modification to this approach is to suspend the wire across a series of small gaps. Figure 5.4a shows a custom microcomb structure fabricated into the edge of a Cu aperture using FIB. This design provides several contact points which provide mechanical support and heat sinking for the sample while contributing minimal background signal. The gaps are wide enough that the nanowire can be viewed from a range of tilt angles around the longitudinal axis. For these VO_2 wires, this provides access to zones which have peaks that correspond to the monoclinic to rutile transformation.

A UED pattern for this sample configuration is shown in Figure 5.4b. This was recorded at 50 kHz averaging 100 frames over 80 seconds total integration. This pattern was recorded along the $[1\bar{1}2]$ zone axis. Several diffraction orders are clearly resolved as in the previous configuration. Some background signal from the polycrystalline copper aperture is observed,

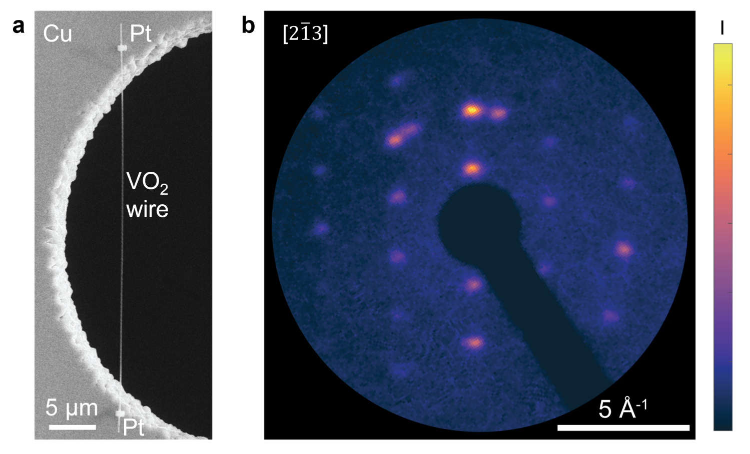

Figure 5.3: Static UED of an individual VO_2 nanowire across a Cu aperture at HiRES. **a** SEM micrograph of the wire. **b** UED pattern

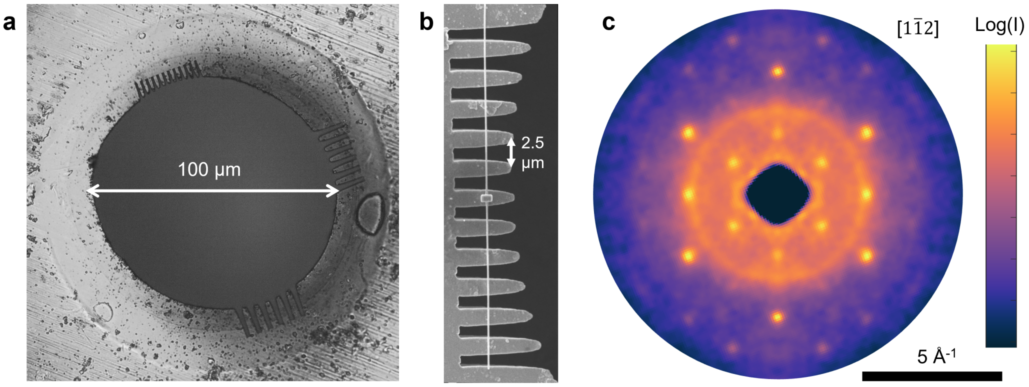

Figure 5.4: Static UED of an individual VO_2 nanowire on a custom Cu microcomb support at HiRES. **a** Optical microscope image of the prototype support used, a Cu aperture with microcombs of varying available dimensions. **b** SEM micrograph of the wire placed along one of the microcombs. **c** UED pattern recorded from the wire. The pattern was symmetrized using the two known mirror planes. The ring background is from the Cu aperture while the peaks correspond to VO_2.

but is readily subtracted by isotropic background removal and has little impact on the dynamic range of the recorded pattern. This configuration also allows to secure the wire to the platform with just one Pt patch in the center, permitting longitudinal expansion or contraction of the wire in either direction. This approach is expected to be most suitable for pump probe experiments.

Altogether, these examples illustrate the potential for studying individual nanowires with high repetition-rate relativistic UED, which could be used to study size-dependent dynamics in one-dimensional quantum materials. Dynamics under weak (perturbative) photoexcitation, such as measurement of electron-lattice coupling constants and coherent lattice modes appear within reach, while high repetition-rate driving of nanomaterials such as through structural transformations poses significant challenges, such as managing the thermal load and mechanical strain. Ultimately, nanoprobes may provide a more suitable approach for strong photoexcitation conditions in some cases.

5.3 Ultrafast relativistic electron nanoprobes at HiRES

As discussed above, shrinking the probe size of relativistic UED from tens of micrometers to the nanoscale permits sampling and mapping of nanoscale regions, enabling a range of nanoscience experiments. However, this imposes stringent requirements on both transverse spatial and angular dimensions of the probe beam while maintaining the usual demand for sufficient flux to achieve acceptable signal-to-noise ratio.

Consider that in the case of diffraction, resolution can be described using the resolving power $\mathcal{R} = R_{hkl}/\Delta R_{hkl}$ [69], where R_{hkl} is the distance of a specific diffraction point/ring with Miller indices (hkl) from the zero-order beam while ΔR_{hkl} represents the minimum distance at which a second point/ring can be discriminated. The resolving power in diffraction is ultimately limited by the angular spread of the beam, $\sigma_{u'}$, which is inversely linked to the spot radius σ_u at the waist by the beam normalized emittance (ie. $\epsilon_{\mathrm{n},u} = \beta\gamma\sigma_u\sigma_{u'}$), with γ and β being respectively the relativistic Lorentz factor and the ratio between the speed of the electrons and the velocity of light. Variables u and u' refer to lateral position and angle coordinates respectively. To achieve a given resolving power at a particular spot size, the emittance requirement is:

$$\epsilon_{n,u} = \frac{\lambda_{\mathrm{c}}\sigma_u}{2d_{hkl}\mathcal{R}} \tag{5.3}$$

where λ_{c} is the electron Compton wavelength and d_{hkl} is the inter-atomic separation distance. For example, to achieve $\mathcal{R} = 10$ with a nanoscale beam ($\sigma_u = 500$ nm) in a sample with an inter-atomic distance $d_{hkl} = 2$ Å, the required normalized emittance is $\epsilon_{n,u} = 300$ pm. Before this work, such a value was more than one order of magnitude beyond the smallest emittance experimentally measured at present date in relativistic ultrafast electron beamlines [70].

Making use of the high repetition rate at HiRES, and employing a specialized permanent magnet lens prototype designed at the Particle Beam Physics Laboratory at UCLA, we achieved ultrafast relativistic electron nanoprobes with transverse emittance values around 500 pm and with probe sizes in the 100-500 nm range. This was made possible by overcoming two main challenges. The first was to determine a configuration of the HiRES beamline that would collimate the electron probes to the small desired emittance. The second was

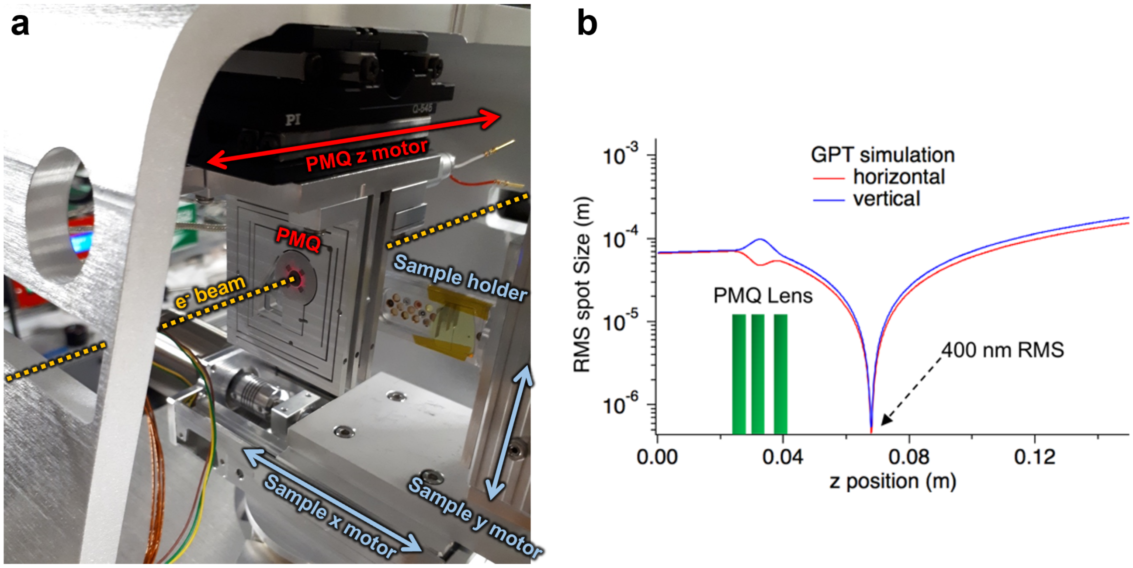

Figure 5.5: Permanent magnet quadrupole (PMQ) lens for ultrafast nanodiffraction and imaging demonstrations at the HiRES beamline. **a** Photo of the setup in the experimental chamber. **b** Particle tracking simulation results predicting focusing to 400 nm RMS spot size for a round input beam with a 50 μm RMS size and 600 pm normalized emittance.[64]

to devise a method for precisely measuring these small transverse beam properties. The following sections describe the approaches devised to achieve and measure nanoprobes, as well as demonstrations of imaging and nanodiffraction capabilities with these probes.

5.3.1 Beamline and nanofocusing lens configuration

Focusing relativistic electron beams to nanoscale spots requires strong confining magnetic fields. In this experimental work we used a prototype in-vacuum lens assembly composed by 3 permanent magnet-based focusing elements[71, 72], which provide a compact alternative to large solenoid lenses. The permanent magnet quadrupole (PMQ) lenses used in these demonstrations were designed with focusing gradients in excess of 100 T m^{-1} ((Fig. 5.5c and inset)) using Neodymium-based permanent magnets ($Nd_2Fe_{14}B$, remanence $B_r = 1.25$ T). They were arranged in a triplet configuration to achieve an overall focal length of $f_e =$ 2.5 cm in both planes. Figure 5.5 shows a picture of the setup as well as the computed transverse evolution of the beam through a configuration optimized using particle tracking simulations [73]. In this example, a round input beam with a 50 μm RMS size and 600 pm normalized emittance is focused down to 400 nm RMS about 2.5 cm downstream the exit of the third focusing element, for relative distances between the quadrupoles of 5 mm and 6.5 mm respectively. More details about the magnet assembly and alignment procedures are published in ref. 64.

The beamline configuration to achieve nanofocused probes, including the computed evolution of longitudinal and transverse dimensions of the beam, is shown in Figure 5.6. Crit-

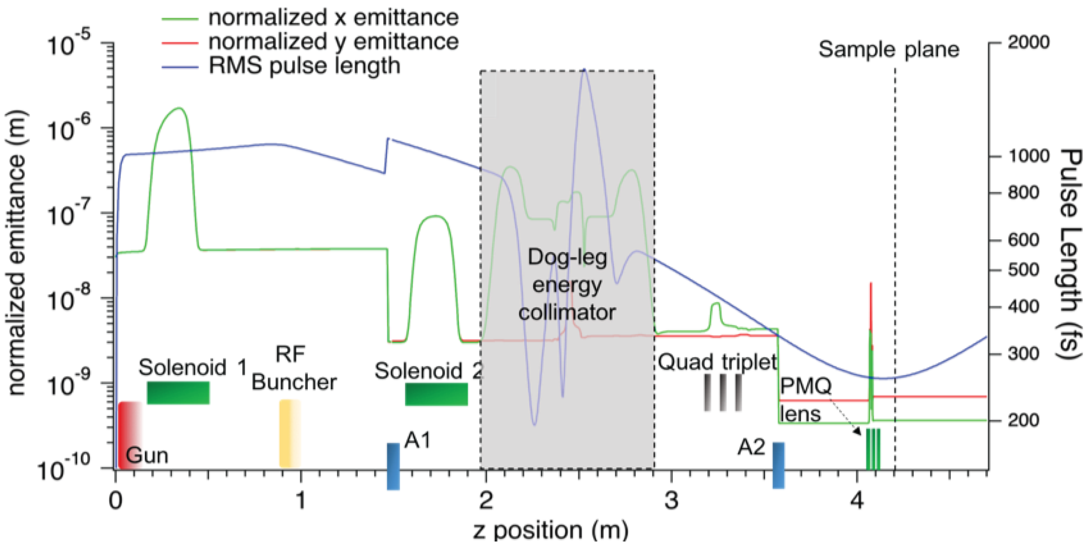

Figure 5.6: Electron beam dynamics simulations showing the behavior of the electron beam emittance and pulse length throughout the beamline. The two apertures A1 and A2 decrease the electron beam emittance by about 1 order of magnitude each. At the same time, a negative energy-time correlation is imprinted on the electron beam by the radio-frequency buncher, which causes the beam to compress in the subsequent vacuum drift, reaching a minimum value at the sample plane.

ically, the transverse emittance is cut roughly tenfold after being directed through each of two pinholes, where the spatial and angular filtering is tuned by adjusting the strengths of the preceding solenoid and quadrupole lenses. This showcases the flexibility of the long beamline permitted in this relativistic electron setup.

In detail, first, a stream of electron beam pulses with an average current of 60 nA is generated using a laser pulse with 300 fs full width at half maximum (FWHM) transversely focused to a 50 μm root-mean-square (RMS) spot on the photocathode. These are then rapidly accelerated by the gun to 735 keV for this experiment. The combination of the first solenoid and a collimating aperture with a fixed diameter of 500 μm (A1 in Fig. 5.6a) downstream from the source selects the particles with low transverse momentum, thereby filtering the transverse phase space. The transverse normalized emittance of the resulting 320 pA beam is about 3 nm, measured by reconstructing the transverse phase space at the aperture position via TEM grid shadowgraph analysis [74]. The the electron beam is spatially filtered again by a second aperture with variable diameter from 1 mm down to 10 μm just upstream of the experimental chamber (A2 in Fig. 5.6a) to reach sub-nanometer emittance values. The electron optics downstream of A1 (not shown) are tuned to modulate the transverse aspect ratio of the beam at A2 and, consequently, partition the four-dimensional emittance to create round or flat beam waists. Typical current values after the second collimator are in the range of 100-200 fA.

In addition, the evolution of the pulse length (blue line in Figure 5.6) highlights how the RF buncher is used to compress the pulses to a longitudinal focus at the sample plane to provide optimal temporal resolution. By tuning the electric field amplitude entering the bunching cavity, the pulse length at the sample can be minimized for a given input beam: in this case, 260 fs RMS at the sample.

5.3.2 Measurement of nanoprobe dimensions and emittance

Measurement and control of relativistic electron beams with nanometer resolution is an active field of research. Recently, measurement of sub-micron electron beams has been reported using the beam-loss monitor signal generated by interaction of the electron beam with a nano-fabricated wire [75]. In our setup we use a similar approach - a knife-edge target is inserted gradually into the beam along the horizontal and vertical direction - but we record the full beam image at the detector for each step (Fig. 5.7a-b). This allowed for a detailed analysis yielding the full phase space reconstruction, uncovering important correlations between the horizontal and vertical plane which would not be seen otherwise. The PMQ lens was moved along the direction of electron propagation, acquiring data at different longitudinal locations (Fig. 5.8a and Fig. 5.8b).

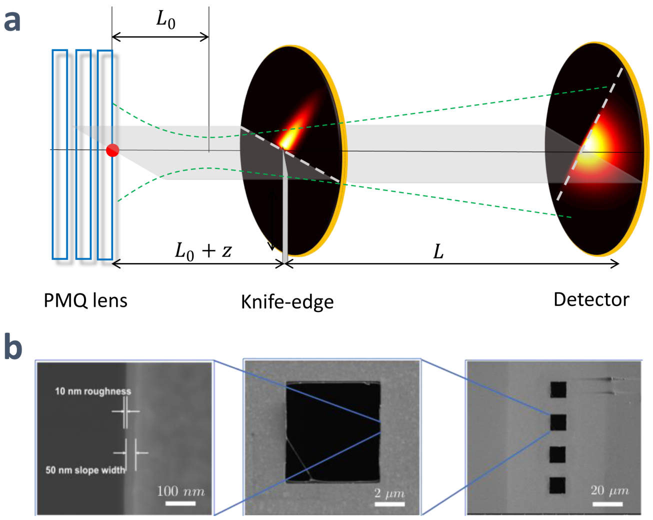

Figure 5.7: Schematic of the measurement technique.**a** The electron beam is focused by the permanent quadrupole lens (PMQ) and is then intercepted by a knife-edge target. The resulting beam image is collected at the detector. The position between the final lens and the target can be varied with < 10 nm precision. **b** Scanning electron microscopy (SEM) image of the knife-edge target.

The knife-edge target used in the measurements is shown in Fig. 5.7b. Focused ion beam (FIB) was used to mill 10 μm x 10 μm square holes from 30 nm SiN windows with 75 nm of gold deposited via thermal evaporation. Scanning electron microscopy (SEM) images of the square edges reveal a roughness of about 10 nm, together with a 50 nm-wide area with rapidly varying gold thickness

We perform a 10-parameter global fit on this dataset to reconstruct the coupled four-dimensional particle distribution in the canonical phase space (x, p_x, y, p_y) [76], the related 4x4 second order beam matrix and its RMS volume $\epsilon_{\mathrm{n4D}} = 0.0144 \pm 0.0065$ (nm rad)^2. The evolution of the eigenvalues of the beam matrix in the xy plane allow the determination of the position and size of the beam waists (Fig. 5.8c), together with its rotation angle. The beam size minima were found to be 363 nm and 609 nm at the specific longitudinal planes shown by the transverse sections in Fig. 5.8d.

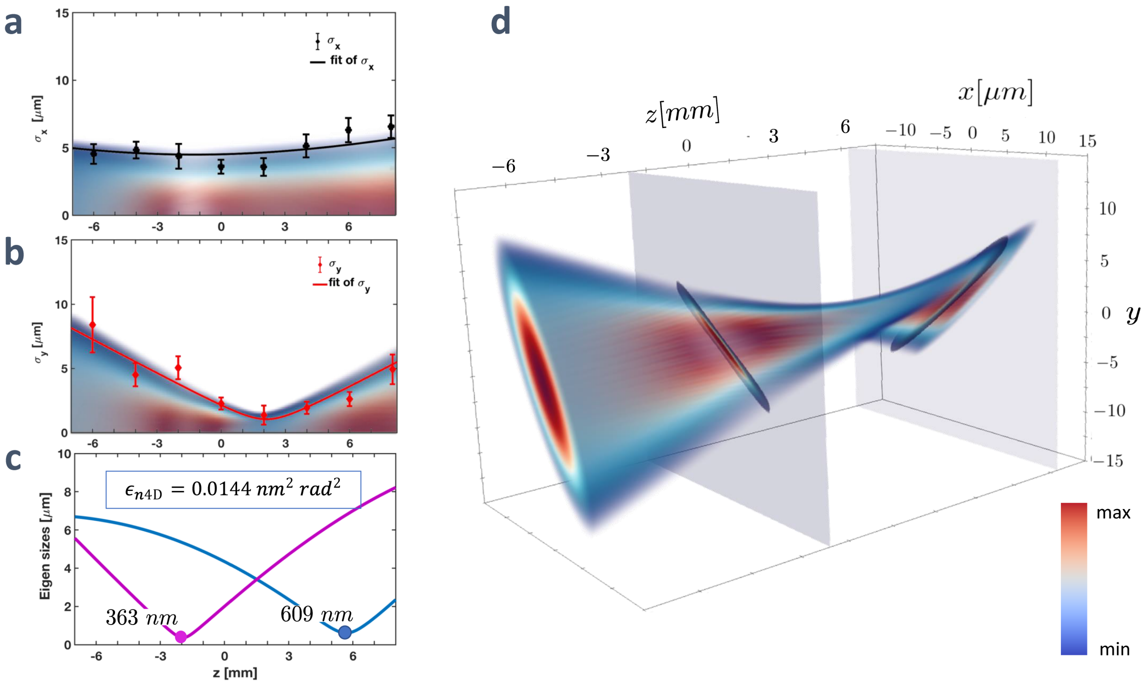

Figure 5.8: Electron beam evolution around the waist. **a** Electron beam evolution projected on the horizontal axis. Black dots represent the experimental data with error bars showing the standard deviation of multiple measurements, while the solid line shows the result of the global fit. Also reported in the plot is the density distribution of the beam, i.e. the projection of the volumetric rendering in **d** onto the horizontal axis. **b** Electron beam evolution projected along the vertical axis, similar to **a**. **c** Evolution of the spatial eigen sizes of the four-dimensional beam matrix. As the beam is rotating in space, a new diagonal matrix is found for each longitudinal position, revealing the beam orientation angle and beam size along diagonal directions. **d** Volumetric reconstruction of the electron beam density evolution. The two longitudinal slices shown represent the positions of electron beam waist.

Asymmetric emittance and spot sizes can be achieved by changing the beam aspect ratio at the second aperture (A2 in Fig.5.6a) to take advantage of the dependence of the apertured beam transverse emittance on the angular divergence distribution before the aperture plane. By re-tuning the upstream quadrupoles to control this divergence, we were then able to generate beams with spot size aspect ratio up to 10 and minimum dimension at the focal point of 91 nm, with a total RMS volume of $\epsilon_{\mathrm{n4D}} = 0.0086 \pm 0.004$ (nm rad)^2. This is reported in more detail in Ref. 64. Such electron probes could be particularly useful in situations where high resolution is only needed in one dimension.

5.3.3 Ultrafast point projection microscopy

When the beam focus position is set upstream the sample plane, the instrument operates in imaging mode, performing ultrafast point-projection microscopy (UPPM). The focal plane is positioned upstream of the sample so the resulting image at the detector represents a magnified mass-contrast shadowgraph of the specimen. To study the resolution of our system in imaging mode, we extended the concept of Ronchi ruling to electron optics [77, 78]. We fabricated horizontal and vertical three-bar rulings with width and spacing ranging from 1.1 μm to 300 nm (Fig. 5.9a). Such rulings provide targets of known spatial frequency composition which can be used to determine the image contrast as a function of frequency, known as the contrast transfer function (CTF). The material is 50 nm of AuPd alloy sputtered onto a 30 nm SiN membrane, and the gaps were milled through with a focused Ga ion beam. With the electron beam focused in the configuration depicted in Fig. 5.8, we formed an image of the target at the detector by accumulating ultrafast point-projection images at 1 MHz repetition rate for 1 second to obtain Fig. 5.9b. The target longitudinal position was chosen to minimize shear and stretching distortions in the final image (z=0 in Fig. 5.8c).

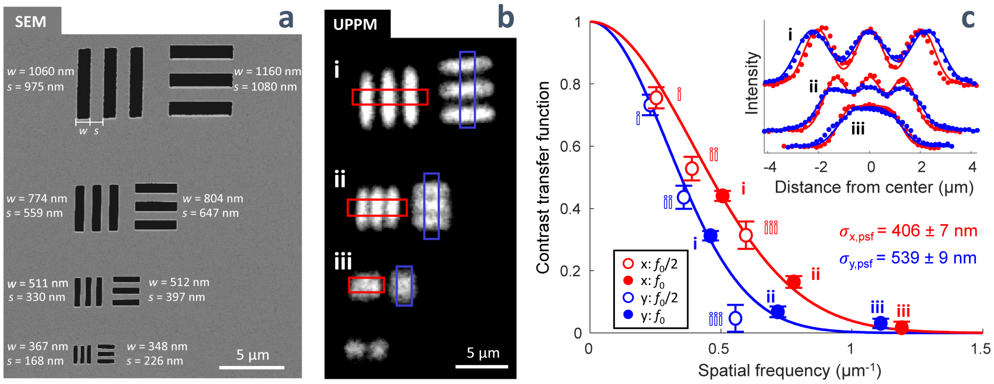

Figure 5.9: Relativistic ultrafast point-projection microscopy calibration. **a** Scanning electron microscopy (SEM) of the resolution target used to determine the contrast transfer function (CTF) of the instrument. The Ronchi rulings are labeled with the mean bar width (w) and spacing (s) as measured by SEM. **b** Ultrafast electron point-projection image of the target. Line profiles were extracted from the red and blue regions for resolution analysis. **c** Contrast transfer function of the instrument for both x and y lateral dimensions. Contrast values obtained from the measured line profiles at f_0, the fundamental frequency, and $\frac{f_0}{2}$ are plotted as points (filled for f_0, empty for $\frac{f_0}{2}$) and fit with Gaussian CTFs (solid curves). Error bars represent one standard error above and below the measured contrast value. $\sigma_{\mathrm{x,psf}}$ and $\sigma_{\mathrm{y,psf}}$ are the standard deviations of Gaussian point spread functions (PSFs) corresponding to the best-fit CTFs. These are shown with the standard error estimated from fitting error. The inset shows the measured ruling profiles (points) superimposed with model profiles (curves) computed by applying the best-fit CTF to step functions with the SEM-measured dimensions. For a detailed description of CTF determination, see the Methods section.

From this image we determine the contrast transfer function of the instrument, shown in Figure 5.9c. We extracted contrast values from the three largest rulings at their fundamental frequency f_0 and $\frac{f_0}{2}$ (see the Methods of ref. 64 for detailed procedure), and we fit a Gaussian

CTF. We verified this CTF by applying it to model gratings with the SEM-measured ruling dimensions to generate the profiles shown in the inset of Fig. 5.9c. These profiles reproduce the shapes of the overlaid measured profiles. From this fit, we find the spatial frequency resolution at 5% contrast to be 0.725 ± 0.012 μm^{-1} in X and 0.960 ± 0.017 μm^{-1} in Y.

The UPPM resolution is set by the angular divergence of the electron probe, which in turn is defined by the beam size at its waist. Therefore we expect the point spread function (PSF) of the system to be closely related to the beam waist size (see Methods section). For the round beam case of Fig. 5.8, we computed the PSF from our fit CTF and found its standard deviation to be 406 ± 7 nm and 539 ± 9 nm respectively in the horizontal and vertical planes, in fair agreement with the minimum beam sizes measurements.

5.3.4 Ultrafast scanning nanodiffraction

When focused at the sample plane, the low-emittance electron beam produces high quality diffraction patterns providing structure and orientation information at the nanoscale. We used the beam described in Fig. 5.8 to map grain orientation and boundaries in a hexagonal close-packed Ti-6 wt.% Al (Ti-6Al in the following) polycrystal. The sample was thinned by jet polishing to create a hole surrounded by ultrathin regions. Electron backscatter diffraction (EBSD) in an SEM was used to create a reference map of the grain orientations near the hole (Fig. 5.10a). Using the point-projection microscopy mode described above, we located and imaged the largest protrusion into the hole to determine the sample in-plane orientation (Fig. 5.10b). We then focused the beam onto the protrusion and obtained a diffraction pattern indicating [0001] in that grain is nearly normal to the sample, matching the orientation determined using EBSD.

We then demonstrated the ability of the ultrafast beam to locate a grain boundary with sub-diameter precision, by scanning the sample stage along one axis and acquiring a diffraction pattern at each 250 nm step. The orientation fraction, the fraction of electrons that pass through a grain, is $f_j = \frac{(I_j/I_j^\circ)}{\sum_k (I_k/I_k^\circ)}$; I_j is the total intensity of a chosen set of diffraction spots due to grain j and I_j° is I_j when the probe is entirely within grain j. We compute I_j by fitting symmetric 2D Gaussian functions to the selected peaks (circled in the figure) and summing their intensities. The orientation fractions of the two grains over the scan are shown in Fig. 5.10c. The scanning interface over the beam produces a cumulative distribution function of the beam intensity along the scan direction. Each orientation fraction is thus expected to follow a Gaussian error function for a Gaussian beam. By fitting Gaussian error functions in the two directions, we identify the crossing point (the center of the interface) with sub-diameter precision: fitting error for the interface position is ± 15 nm standard error. This demonstrates the potential for precise nano-UED studies of interfaces.

Finally, we formed an ultrafast scanning transmission electron microscopy (USTEM) image by mapping the crystal orientation throughout a continuous bend in the sample over a 20 μm x 14 μm area in 2 μm steps (Fig. 5.10d). We identified four on-zone orientations along this bend in the diffraction patterns, made possible by the nanoscale beam size. We approximate the orientation at each location to be an average of these four zone axes weighted by their orientation fraction as defined above. The colors in the USTEM orientation map

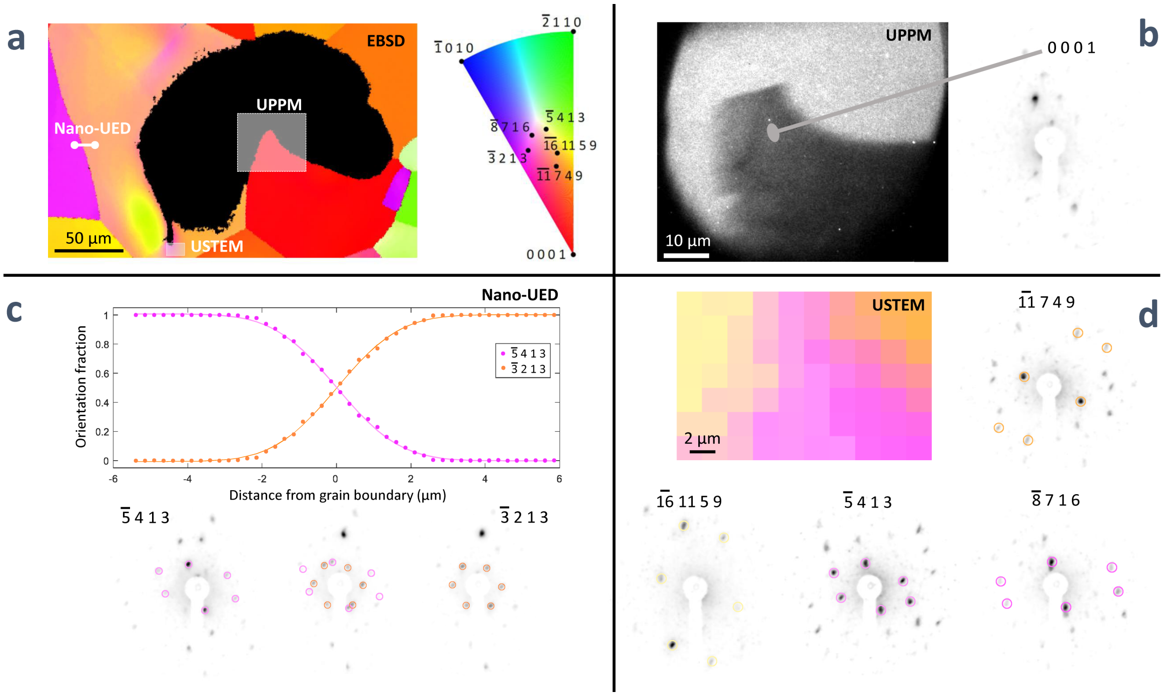

Figure 5.10: Demonstration of ultrafast scanning transmission electron microscopy (USTEM) correlated with electron backscatter diffraction (EBSD). **a** High resolution orientation map of a Ti-6Al polycrystal sample performed using EBSD in a scanning electron microscope. Shape and crystallographic orientation around the hole (black region in map) are used to correlate the probe position in the ultrafast electron diffraction (UED) apparatus with the map. **b** Ultrafast point-projection microscopy (UPPM) of the sample in the UED setup. This location was found by searching for the highlighted feature in panel a in imaging mode and confirming the crystallographic orientation in diffraction mode. Once oriented, a scan along a chosen grain boundary (**c**) and a USTEM map (**d**) were obtained with the relativistic ultrafast electron probe.

correspond to those used in the EBSD map. The USTEM map shows a gradual bend matching the sample bending found around the hole in the EBSD map of the same region. This example demonstrates potential for spatio-temporal mapping with nanoscale spatial resolution.

5.4 The future of nanoscale relativistic UED

Altogether, this work demonstrates the potential of high-brightness relativistic UED facilities like the HiRES beamline to access nanoscale dynamics, either by probing isolated nanostructures or forming nanofocused probes. For approaches that seek to study individual nanostructures without forming nanoprobes, the sample preparation strategies explored here provide a starting point but need to be tested case-by-case and may need further development. That said, the nanoprobe approach provides many advantages, including ability to switch between imaging and diffraction modalities as well as to reduce the pump size. A smaller pump beam will likely be a critical step to reduce the thermal load and enable the use of high repetition rates. Integration of such a focused optical pump with the probe-forming lenses needs to be demonstrated and optimized. While the proof of principle demonstrations here utilized a compact permanent magnet lens configuration, future instruments could benefit from using more expensive but more precise MeV-scale objective lenses to provide greater electrostatic control and reduce aberrations.

Development of brighter sources would allow to reduce the spot size even further. This quest is the subject of the following chapter, where plasmonic nanostructures which can confine and focus incident light intensity to nanoscale regions are explored and tested as low-emittance electron sources.

Chapter 6:

Plasmon-enhanced photoemitters for brighter UED probes

---

*Part of the work presented here is based on an article published in *Physical Review Applied* [79] as well as two SPIE Optics and Photonics conference proceedings[80, 81].

6.1 Potential for brighter ultrashort electron probes

So far, it has been shown that continuous-wave RF photoguns like the APEX gun used at the HiRES beamline provide a high current and high brightness source of pulsed electron beams. While the ability to form sub-micrometer electron probes and to resolve diffraction from individual nanowires marks a significant advancement for ultrafast electron technology, these beams are still not bright enough to access behavior at the few nm scale, ie. in nanowires and quantum dots in size regimes of strong confinement and at the scale of individual defects and interfaces. To reach that scale, another order of magnitude improvement to the beam brightness must be made.

One remaining limitation is the initial beam size. The maximum brightness that can be achieved from an electron source is proportional to $R^{-1/2}$ (for sufficiently long pulses, as elaborated in the following section)[82]. In a flat photocathode, the initial beam size is set by the initial laser spot size. For instance, for a gaussian laser beam, $R_{electrons} = R_{laser}/\sqrt{n}$ for n-photon photoemission. Then, a smaller initial source size not only reduces the amount of collimation needed to achieve a low transverse emittance, but also provides a larger number of electrons per pulse in that final beam. RMS laser spot size is typically on the order of tens of microns, and shrinking the laser size by a factor of 100 could provide a tenfold improvement in the brightness. However, the geometry of most UED beamlines, including HiRES, requires the final focusing lens to be positioned far from the cathode surface, providing limited numerical aperture and forcing large laser spots at the cathode. Lower energy ultrafast electron microscopes employing DC fields utilize tip emitters, but tips have shown major instability under high amplitude RF fields like employed at HiRES.

This section discusses recent work towards a compelling solution to this problem: utilizing plasmonics to shape and enhance photoemission from smaller regions at the cathode surface. Here, gold plasmonic lenses designed for multiphoton photoemission using near-infrared excitation are studied. They can be illuminated with a laser spot of arbitrary size to achieve electron pulses with fs-scale duration, tunable with the number of rings, and 60 nm RMS lateral size, 3 orders of magnitude smaller than typically emitted in RF guns. They can also be fabricated in large arrays, permitting generation of multiple beams simultaneously which could be applied to multi-beam electron diffraction or other applications like multi-beam electron lithography. A DC photogun setup for testing such emitters is also demonstrated on plasmonic nanogroove cathodes, paving the way for similar measurements on plasmonic lens and other novel photocathodes.

6.2 Plasmon-enhanced emitter background

6.2.1 Benefits of small source size for nanoprobe brightness

As discussed in the previous chapter, forming a nanoscale electron probe requires achieving a small transverse emittance (eq. 5.3). For the proof-of-principle demonstration of nanoprobes at HiRES, this was achieved by filtering and collimating a tens of micron diameter beam emitted from a flat cathode. However, this approach only goes so far because the amount of charge per pulse that can be extracted is limited: extracted electrons impart space charge forces that repel the electrons still at the surface, and so a maximum extracted charge is reached when space charge forces are large enough to counter the extraction field. A wider extracted beam imparts greater space charge forces for the same current density, reducing the maximum current density that can obtained from the cathode surface.

Filippetto et al and Bazarov et al derived equations for the space-charge limited current and transverse beam brightness that can be extracted from a flat photocathode[82, 83]. Two regimes are discussed, where the beam size is either larger or smaller relative to its longitudinal length, Δz_e, given by:

$$\Delta z_e = \frac{eE_0}{2m}\Delta t^2 \tag{6.1}$$

For UED at HiRES, where the extraction field is 20 MV/m and the cathode laser is of the order of 1 ps RMS (bunches are then compressed), the longitudinal length is about 1.7 μm. When the beam radius is larger than the longitudinal length (referred to as the "pancake regime"), outer electrons are too far away to affect the inner electrons and so the maximum current density is independent of size. On the other hand, for beams with small radius compared to their longitudinal length ("cigar regime"), the current density scales with $R^{-1/2}$:

$$J_{sat,2D} = C_c I_0 \frac{\sqrt{2}}{9} \frac{eE_0}{\pi R^{1/2} mc^2} \tag{6.2}$$

Here, E_0 is the applied electric field at the cathode, $I_0 = \frac{4\pi\epsilon_0 mc^3}{e}$ is the characteristic Alfven current, C_c is an order-of-unity scaling factor that adjusts for effects not accounted for in the model which can be obtained using particle tracking simulations. This was obtained by solving the Poisson equation for a cylindrical charge distribution with a length set by the effective on-axis distance over which the field from each circular slice acts.

This leads to a proportionality relationship for the transverse brightness:

$$B_p = \frac{Q}{\epsilon_n^2} \propto \frac{E_0^{3/2}\Delta t}{R^{1/2}\sigma_p^2} \tag{6.3}$$

Hence, having a nanoscale initial beam can in principle allow one to form nanoprobes of a given emittance with higher charge per pulse than by collimating a large initial beam. In practice, evolution of the beam during transport must also be considered. It should also be noted that decreasing radius decreases the total charge per pulse. In the cigar regime, maximum charge per pulse scales with $R^{3/2}$:

$$Q_{sat} = \pi R^2 J_{sat,2D} \Delta t = C_c I_0 \frac{\sqrt{2}}{9} \frac{e E_0 R^{3/2}}{mc^2} \Delta t \tag{6.4}$$

So, ideally one should only reduce the initial spot size to match the desired final transverse emittance. For a desired q resolution $\sigma_{q,det}$ we can compute the ideal source size relative to the desired probe size at the sample:

$$\frac{R_{source}}{R_{sample}} = \frac{h\sigma_{q,det}}{\sigma_{p,source}} = \frac{h\sigma_{q,det}}{\sqrt{m_e \text{MTE}}} \tag{6.5}$$

Where h is Planck's constant. For example, to maintain a q resolution of 0.03 Å^{-1} (s resolution of 0.2 Å^{-1} like used at HiRES, see chapter 3) using a cathode material with a mean transverse energy (MTE) of 0.1 eV, the source size should ideally be about 1.65 times the desired probe size. This calculation assumes no transverse collimation of the beam: in practice, the initial source may need to be larger and somewhat collimated to permit more control over the shape at the sample and detector.

Granted, these equations only describe the initially extracted transverse brightness. After extraction, higher charge density beams are subject to stronger Coulomb repulsion during transport, leading to emittance growth and reduced transverse brightness. While longitudinal growth can be partially compensated with compression as energy spread does not usually matter for UED measurements, transverse emittance growth necessarily enlarges spot size or degrades q resolution. A strategy to mitigate these effects could be to expand the beam shortly after extraction and then refocus at the sample plane, transversely and/or longitudinally, to reduce the charge density during most of the transport. That said, effects such as lens aberrations need to be considered[84]. Still, in practice, the maximum brightness at the sample will be lower than originally extracted, especially if multiple crossovers are present before the final focusing at the sample. Beamline design and optimization will be important to achieve higher brightness nanoprobes.

Nonetheless, these equations show that for UED nanoprobes, a nanoscale emitter with low MTE that can withstand high extraction fields is desirable. Tip emitters can be fashioned to achieve few nm initial probe sizes, but their large initial angular spread demands significant initial collimation and the sharp tips are not well suited for high amplitude RF fields. So, while effectively used in DC ultrafast electron microscopes, they typically produce much less than one electron per pulse. Flat photocathodes with tightly focused optical excitation in RF photoguns could provide a route to higher current nanoprobes. Rear illumination of cathodes using a high NA objective is being explored to achieve smaller source sizes near the optical diffraction limit[85]. Plasmonic nanostructures, as explored in the following sections, provide a route to achieve such a source.

6.2.2 Plasmonic physics and design considerations

To effectively design a plasmon-enhanced photocathode, it is important to understand the fundamental physics of plasmons and how they behave in real materials. Here, I discuss relevant theoretical concepts and material properties as well as their impacts on cathode design, including fundamental behaviors of plasmons and how they depend on the material, how plasmons interact with light, and how nanostructuring modifies plasmon behavior.

Mobile valence electrons in a material can collectively oscillate in the bulk or at the surface with a range of frequencies, modulating the local electric field in the process. Plasmons are the quantum mechanical quasi-particles associated with such plasma oscillations. The range of plasmon frequencies depends on the material and the interparticle interactions. In the simple case of a Drude-Sommerfeld free electron model, the sea of free electrons in the bulk has a natural resonance at the plasma frequency due to restoring forces imparted by the local charge imbalance induced during displacement of the electrons:

$$\omega_p = \sqrt{\frac{ne^2}{m\epsilon_0}} \tag{6.6}$$

At a surface, different oscillation modes are available than in the bulk. These surface plasmons have a reduced frequency set by the dielectric response of the material above the surface. For a free electron metal in vacuum ($\epsilon_2 = 1$):

$$\omega_{sp} = \frac{\omega_p}{\sqrt{1+\epsilon_2}} = \frac{\omega_p}{\sqrt{2}} \tag{6.7}$$

Under a sinusoidal electric field, such as that of a light wave, electrons in the bulk or surface can collectively oscillate at frequencies up to the plasma frequency. The frequency-dependent behavior is analogous to that of a driven harmonic oscillator. At low frequencies, the electrons essentially follow the driving field, modifying the phase velocity of the incident field and stopping when the field is removed. Near the plasma frequency resonance, the electron plasma absorbs some of the incident energy and oscillates with enhanced amplitude, persisting for some time after the field is removed. The oscillation strength and decay time is dependent on the bandwidth of the resonance mode. Well above the resonance frequency, the electron plasma is not able to move with sufficient velocity to keep up with the field and has no interaction with the incident field.

When light is coupled with a surface plasma oscillation, it is called a surface plasmon polariton (SPP). SPPs provide propagating optical fields confined to the surface which can be used to form a variety of time-dependent optical field patterns at a material surface. The dispersion relation of SPPs reflects the frequency-dependent behavior of the plasma oscillations described above. At low frequencies, SPPs show linear dispersion similar to free-space light but with slightly reduced group and phase velocity. In this regime, SPPs can have long propagation lengths limited by surface and intrinsic material scattering processes. Near the plasma frequency, the SPP adopts more plasmonic character, dramatically slowing the group velocity and decreasing the wavelength. This also leads to much shorter propagation lengths.

In addition, geometric confinement within sub-wavelength dimensions can support surface plasmon resonances, such as localized surface plasmons in metallic nanoparticles and resonances in nanocavities.

So, these plasma oscillations provide a means for metallic materials to interact with and manipulate the behavior of light in their bulk and at their surface, which can be exploited

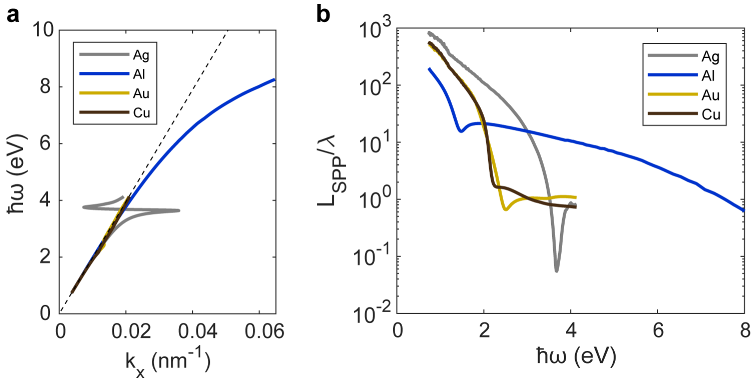

Figure 6.1: Plasmonic characteristics of four commonly used plasmonic metals in vacuum. These were calculated using measured dielectric functions from thermally evaporated, template stripped films[89]. **a** Dispersion relations superimposed with the vacuum dispersion of free-space light (black dashed line). **b** SPP propagation lengths. **c** Localized surface plasmon quality factors.

through intelligent material and geometric design to shape optical fields. Confinement, enhancement, and shaping at the surface is powerful for designing photoemitters with desirable spatial and temporal characteristics.

The response of the electron plasma in the constituent material(s), including the dispersion and propagation length, is important to consider when selecting materials for a plasmonic device. The plasma frequency provides an *upper bound* for the useful range of a material for plasmonics. For commonly used metals, these are typically in the range of visible to UV light: for example, by fitting the Drude model to measured optical constants at infrared wavelengths, $\hbar\omega_p$ was found to be 8.5 eV in gold and 8.9 eV for silver[31, 86].

In reality, the optical response of metals can vary drastically from the Drude-Sommerfeld model, which can be reflected in the electronic bandstructure of the material. Namely, excitations with sufficient energy will generate inter-band transitions in many metals, and these transitions often occur at energies much lower than the plasma frequencies listed above.

For a general dielectric function, the SPP dispersion is given by the following equation[87]:

$$k_x = \frac{\omega}{c}\left(\frac{\epsilon_1\epsilon_2}{\epsilon_1+\epsilon_2}\right)^{1/2} \tag{6.8}$$

The real part of the wave vector indicates the wave periodicity, whereas the imaginary part relates to the SPP propagation length[87]:

$$L_{spp} = \frac{1}{2k_x''} \tag{6.9}$$

An additional figure of merit has been identified for localized surface plasmons, the quality factor[88]:

$$Q_{LSP} = -\frac{\epsilon'}{\epsilon''} \tag{6.10}$$

Values of these calculated for commonly used plasmonic metals based on refractive index measurements of high quality, template-stripped films of Cu, Ag, Au, and Al[89] are shown in Figure 6.1. In general, the plasmonic properties are best at lower wavelengths, ie. below the onset of interband transitions. In this regime, SPP propagation lengths and LSP quality factors are larger and increase with wavelength. The onset of strong interband transitions varies by the material: around 2 eV for Au and Cu, and between 3 and 3.5 eV for Ag. Though having the smallest propagation lengths in the infrared, Al provides the most potential for use of SPPs in the UV range. In the infrared regime, the differences between metals can be understood within the Drude-Sommerfeld model. The key parameters are the electron relaxation rate and the plasma frequency: Slower electron relaxation and faster plasma frequencies provide longer plasmon lifetimes.

One other important selection criterion in practice is the reactivity of the metal. For one, it is easier to prepare high quality films of lower reactivity metals as they are less sensitive to deposition conditions including rates, temperatures, and vacuum pressure[89]. Also, lower reactivity metals are typically less likely to be degraded over time by ambient surface reactions. The near-infrared plasmon-enhanced photoemitters studied in this work were fabricated using gold because it not only provides sufficient plasmonic properties at the design wavelength, but also is a highly noble metal, minimizing risk of degradation during film growth and permitting ambient characterization.

It is important to note that SPPs cannot typically be generated by impinging light upon a flat material-vacuum interface, as the dispersion of SPPs does not directly overlap with the dispersion of light in vacuum. However, scattering processes can provide the momentum transfer to mediate this coupling. For instance, surfaces with sub-wavelength topography, including intrinsic roughness, can permit SPP generation.

This can be leveraged by designing surface nanostructures to generate SPPs with a desired geometry and time-dependent behavior. Gratings are commonly used as they diffract light to specific angles, providing well defined, selective conditions for SPP formation. The condition for SPP formation from a sinusoidal, infinite grating with grating vector g and incident light with a wave vector $\mathbf{k_{inc}}$ and in-plane polarization components parallel to the grating vector is given by the grating equation:

$$\mathbf{k_{spp}} = \mathbf{k_{inc,in-plane}} + n\mathbf{g} \tag{6.11}$$

Which ensures that conservation of momentum is satisfied. Real gratings have finite extent and often non-sinusoidal shape, in which case this relationship can be applied to all spatial frequency components present in the grating: for instance, gratings with only a few lines will have a broad spatial frequency bandwidth and permit coupling of light over a larger bandwidth. This discussion assumes a thin grating that minimally disturbs SPP propagation; thicker gratings can deviate as they disturb the SPP mode and typically require electromagnetic simulation to model accurately, but often the same qualitative principles apply.

While SPPs generated from a linear grating propagate parallel to the grating vector, other grating shapes and light polarization states can be used to create more complex SPP patterns. A particularly relevant example for photoemitters is plasmonic lenses, which use annular gratings coupled with vortex light beams to produce radial SPPs with a strong central node. Examples include coupling radially polarized light to bullseye gratings and circularly polarized light to Archimedean spiral gratings. Both of these structures are theoretically and experimentally studied as photoemitters for bright electron beams with small spot size in this chapter.

Nanostructuring can also be used to introduce geometric surface plasmon resonance (SPR) through confinement at length scales near or below the plasmon wavelength. Examples include metallic nanoparticles and nanoantennae[90] as well as nanogroove cavity resonators which can be used to strongly enhance absorption of a surface[91]. The resonance quality factor, and hence resonance duration, is determined by the quality of the nanostructure and frequency of scattering events from that geometry as well as intrinsic scattering losses in the material.

Individual SPR elements can also be periodically arranged to introduce a diffractive mode that can be hybridized with the SPR modes[92]. For instance, gratings of nanogroove cavities can provide a hybridized mode that allows incident light to be easily coupled while providing a resonance effect not achieved in a typical grating[91]. Such a structure has been demonstrated to enhance the absorption and photocurrent from metallic photocathodes[93], and a similar approach using periodic 2D arrays of nanoscale round holes has also been used[94]. In this chapter, nanogroove cavity arrays will be used to demonstrate a new DC photogun built at LBNL for testing novel photocathodes for next-generation UED/M instruments, and new insights into the properties of electron beams emitted from these structures will be described.

6.2.3 Multiphoton photoemission

The above section illustrates how plasmonic elements used in combination, and with judicious selection of materials, allow engineering of surface optical fields with a broad range of spatiotemporal characteristics, including at sub-wavelength dimensions. To design photoemitters using these elements, it is then necessary to consider the physics of the photoemission process. Generally, photoemission occurs when incident photons provide sufficient energy to an electron to overcome the material's work function, ie. the potential barrier between the material and the vacuum. This process is easiest when the individual photons have energy greater than the work function, such that only one photon needs to be absorbed to eject an electron. However, it is also possible for an electron to absorb multiple photons and be ejected, provided that the sequential absorption events can all occur before the excited electron returns to its ground state. Multiphoton processes allow use of longer wavelength light with photon energies well below the material work function, which allows use of plasmonics below the onset of interband transitions to shape optical fields for photoemission.

Multiphoton photoemission processes generally require much higher optical intensity to induce, and the measured photocurrent scales with the intensity raised to the number of photons that must be absorbed. The likelihood of photoemission for a given photon energy depends on intrinsic material properties, including optical transition probabilities and lifetime of excited carriers, as well as extrinsic characteristics of the incident light including spot size, energy, and pulse length. One formula for calculating photocurrent for an nth order photoemission process invokes the generalized Fowler-Dubridge theory[95]:

$$J_n(h\nu) = a_n A(\frac{e}{h\nu})^n(1-R_\nu)^n I^n T_e^2 F(\frac{nh\nu - e\Phi}{k_b T_e}) \tag{6.12}$$

where $A = 120$ A cm^{-2} K^{-2} is the Richardson constant, e is the electron charge, R_ν is the reflectivity, I is the incident light intensity, T_e is the electronic temperature, Φ is the work function modified by the Schottky effect, and $F(x)$ is the Fowler function. This formula allows computation of multiphoton photocurrents in a broad range of experimental situations once the material-dependent constant a_n has been measured in a test case (or computationally predicted).

The nth power scaling of multiphoton photoemission can be beneficial for photoemitter design. Firstly, photocurrent density from strong intensity regions is greatly enhanced compared to weak intensity regions (the ratio also scales with nth power), providing a natural suppression of emission from optical field tails and defective sites compared to a primary enhancement feature. Secondly, photocurrent features have smaller dimension compared to their optical field counterparts, ie. the RMS spot size of a 2D gaussian peak will shrink by a factor of $\sqrt{n}$. Likewise, temporal profiles of photoemitted beams can have features of reduced duration and suppressed tails. Electromagnetic simulations presented in this chapter for plasmonic lens emitters illustrate how these effects are predicted to shape the emitted beams in that case, including the ability to emit sub-100 nm RMS electron pulses with comparatively low emission from grating edges from a near-infrared plasmonic lens.

That said, there are also practical matters to consider when utilizing multiphoton photoemission. One is that the beam charge is more sensitive to laser fluctuations by a factor of n (differential error analysis provides that $\frac{\sigma_J}{J} = n\frac{\sigma_I}{I}$). This imposes stricter requirements on laser stability. Also, higher laser intensities are required to achieve electron pulses of a desired charge density, so this approach is typically best suited for short and small electron pulses. Achieving larger, longer, and higher charge beams using multiphoton photoemission may be limited by stability of the material, including ablation resistance from single shots as well as thermal stability over a series of shots.

If the local optical field is strong enough, it can have further impacts on the photoemitted beam. For one, strong enough optical fields can modulate the work function of the material, permitting emission of attosecond electron bunches at the peaks of the incident field[96, 97]. Also, strong evanescent fields can act on the emitted electrons as they leave the surface and impart time-dependent energy to the particles. Multiphoton photoemission in strong-field, nonlinear regimes is an area of active research which could be useful for generating attosecond electron pulse trains for attosecond electron imaging and spectroscopy.

6.2.4 Plasmon-enhanced photoemission

Several prior works have explored the use of plasmonic nanostructures to develop enhanced photoemitters. For instance, gratings have been patterned into the shafts of metallic tip emitters. The gratings couple the light into SPPs which travel to the tip and are squeezed to sub-wavelength dimensions, providing highly coherent, ultrashort plasmon-enhanced emission[98, 99]. Multiphoton photoemission has also been demonstrated from nanostructures with strong SPR, even permitting detectable photocurrent from continuous-wave illumination[100]. While such designs can be employed for DC photoemission, they may not be stable in high-amplitude RF photoguns and will be limited to less than one electron per pulse.

Other works sought to enhance the performance of large-area photocathodes through producing nanopatterned surfaces. In one example, nanogrooves were patterned into gold-coated cathodes and were found to increase the multiphoton photocurrent yield from 800 nm pulsed laser excitation by 6 orders of magnitude compared to bare gold [93]. These structures used coupled grating and cavity surface plasmon resonances to effectively trap the incident laser light, providing nearly 100% absorption whereas bare gold typically absorbs less than 1% at this wavelength. A similar approach using nanohole arrays designed to have a grating resonance was demonstrated in copper cathodes, increasing photocurrent yield 120 times over bare copper [94].

These examples to improving the emission characteristics are compatible with high accelerating fields. However, the photoemitted beams in these cases still had limited quality [94]: The optical fields were concentrated at edges, inducing emittance growth similar to the effect of surface roughness [101]. Also, their temporal response was not studied in detail, and may be limited by the cavity-resonance damping time. In addition, the emission is still dispersed over several micron areas in these initial demonstrations.

Altogether, these works provide initial demonstrations of how plasmonics can be employed to enhance photoemission, but do not yet fulfill the quest to increase maximum brightness in relativistic UED. Thankfully, many concepts in plasmonics remain that can be leveraged to improve designs for relativistic UED photocathodes.

6.3 Plasmonic lens emitters

This section details theoretical and experimental investigation of bullseye plasmonic lenses for ultrafast, nanoscale photoemitters. Such structures concentrate optical fields to a single, central spot on a flat surface [102, 103], potentially providing aberration-free electron emission and enabling the use of nanoscale photo-triggered emitters in high-field environments. We first show electromagnetic simulations to demonstrate how to control the spatiotemporal characteristics of the optical fields and the corresponding photoemission by geometric design. Then, we demonstrate fabrication of actual bullseye lenses in gold films by two methods and characterize their plasmonic behavior using cathodoluminescence spectro-microscopy. We show that spatial and spectral plasmonic characteristics are like predicted in simulation, supporting that ultrafast nano-emission can be achieved. Altogether, the results support the potential for bullseye lenses as high brightness electron sources and establish a new research direction in the field of plasmon-enhanced ultrafast electron nano-emission.

6.3.1 Principles and design of plasmonic lens emitters

Lens material and geometry

The system under study is a nanopatterned photocathode excited by ultrafast laser pulses with an 800 nm center wavelength. The pattern consists of equally-spaced, concentric annular grooves forming a bullseye plasmonic lens. The geometry is defined by the five parameters illustrated in Figure 6.2a: The number of rings N, grating period p, groove width w, groove depth d, and center plateau radius r_i. Such gratings couple the component of incident light with electric field perpendicular to the grooves into surface plasmon polaritons (SPPs). A

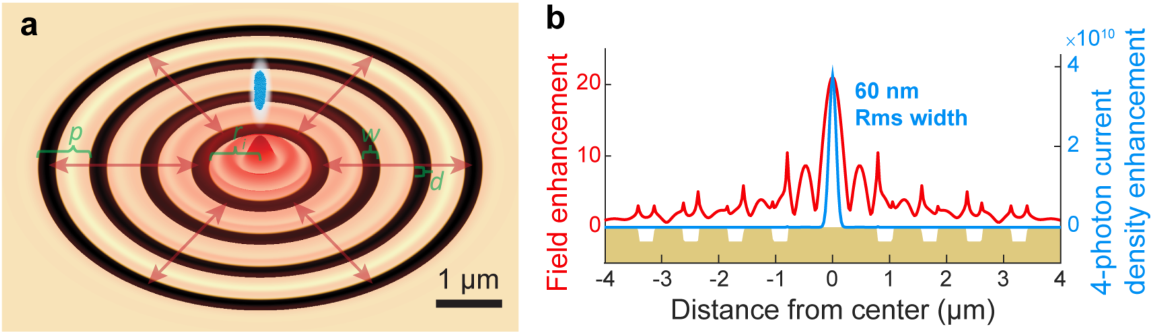

Figure 6.2: Simulated electric field and photoemission profiles during excitation of a Au plasmonic bullseye lens with a radially polarized, 800-nm, continuous-wave (cw) laser. **a** Illustration of the bullseye lens geometry. The parameters shown include the grating period p, groove width w, groove depth d, and center plateau radius r_i. For the simulation results in following subpanels, $p = 783$ nm, $d = 90$ nm, $w = 270$ nm, and $r_i = 783$ nm. The number of rings $N = 4$. **b** Total ($|E|$) electric field enhancement and 4-photon photocurrent (J_4) density profiles. The field enhancement is defined relative to the peak field in the incident beam. The bullseye topography is superimposed on the plot for reference: grooves are 90 nm deep. FWHM is full width at half maximum.

radially polarized laser at normal incidence is used so that the electric field direction is always perpendicular to the grooves and the launched SPPs are in phase. These SPPs then propagate and interfere to give maximum field enhancement at the structure center.

We use gold as the plasmonic material, enabling four-photon photoemission at 800 nm wavelength. Gold is oxidation resistant and provides effective photoemission surfaces; in fact, four-photon photoemission from gold cathodes patterned with linear gratings has been demonstrated [93]. Gold also provides long SPP propagation lengths in the red and near-infrared range: 10-15 μm in as-deposited polycrystalline films [104, 105] and greater than 60 μm in template-stripped and single-crystal gold films [89, 106, 105].

Nanoscale field enhancement and photoemission

We first simulate the electromagnetic fields for a lens under continuous-wave (cw) illumination to study their spatial distribution and the expected emission spot size. An 800-nm wavelength laser is focused at the surface using a numerical aperture (NA) of 0.07, giving a donut-shaped in-plane intensity with peak-to-peak diameter of 4.5 μm. The lens has 4 rings with period p of 783 nm, which is the corresponding SPP wavelength in gold. This aims to satisfy momentum conservation between the normal incidence photons and the SPPs as given by the grating equation (Eq.6.11). We set r_i to be 783 nm to coincide with antinodes of the two-dimensional (2D) standing wave formed by the interfering SPPs. This causes reflections from the edge to resonate, further increasing field enhancement. With these parameters fixed, we then performed a series of finite-difference time-domain (FDTD) simulations in Lumerical [107] to optimize the depth and width of the rings for maximum field enhancement at the center. The optimum is found for $d = 90$ nm and $w = 270$ nm.

The electric field magnitude profiles for the optimized structure are shown in Figure 6.2b.

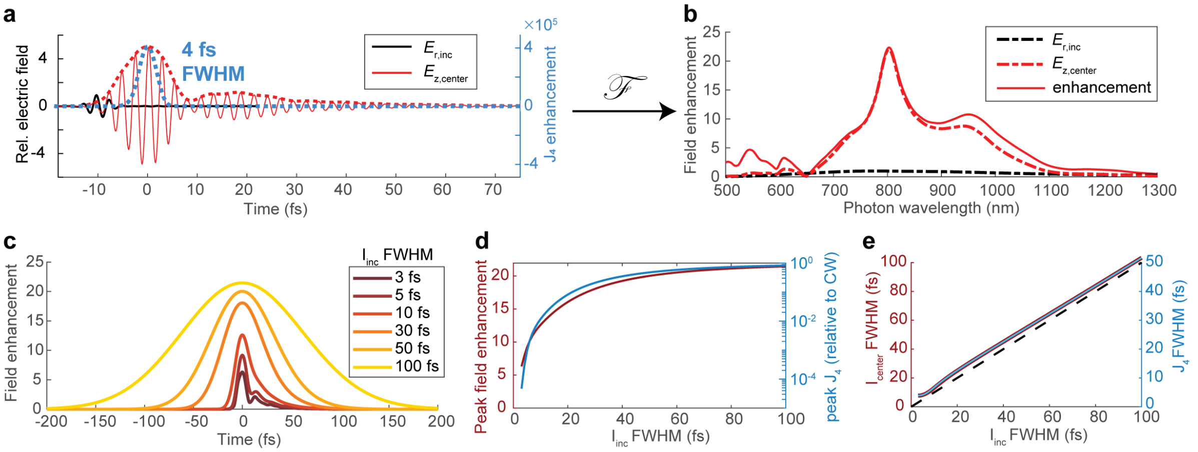

Figure 6.3: Simulated ultrafast temporal response of the Au plasmonic bullseye lens studied in Figure 6.2. The number of rings $N = 4$, grating period $p = 783$ nm, groove width $w = 270$ nm, groove depth $d = 90$ nm, and center plateau radius $r_i = 783$ nm. **a** Impulse response computed using an incident radially-polarized laser pulse with a temporal full width at half maximum (FWHM) of 3 fs. $E_{r,inc}$ is the maximum lateral electric field of the incident pulse, and $E_{z,center}$ is the normal electric field at the bullseye center. The electric field is normalized to the maximum $E_{r,inc}$. Time-dependent 4-photon photocurrent density (J_4) is superimposed. **b** Transfer function obtained by Fourier transform of the impulse response. Enhancement, ie. the magnitude of the transfer function, is shown along with the magnitudes of the Fourier transforms of $E_{r,inc}$ and $E_{z,center}$. Enhancement is obtained by dividing the Fourier transform of $E_{z,center}$ by that of $E_{r,inc}$. **c** Field enhancement temporal envelopes for varying incident pulse durations. I_{inc} FWHM is the temporal full width at half maximum of the incident pulse intensity. **d** Peak field enhancement and photocurrent density (J_4) at the bullseye center as a function of incident pulse duration. Peak J_4 is plotted relative to the J_4 under cw illumination. The top of both y axes correspond to the value under CW illumination. **e** The temporal FWHM of the field intensity at the bullseye center (I_{center}) and J_4 as function of incident pulse duration.

The field enhancement relative to the peak field of the incident laser is maximized at the center (21.0). Also, the lateral electric field E_r is zero at the center and remains small relative to the normal field E_z within the four-photon photoemission peak shown in Figure 6.2c.

The anticipated four-photon photocurrent density $J_4 \propto |\mathbf{E}|^8$ [108]; the photocurrent density enhancement is shown in Figure 6.2b. Remarkably, the J_4 enhancement at the center is 3.8×10^{10}. Also, using multiphoton photoemission practically eliminates contributions from the side lobes and edges of the structure, creating a single, tightly focused emission spot with full width at half maximum (FWHM) of 140 nm in the flat center plateau.

Ultrafast temporal response

To study the emitter's temporal response and how it depends on the lens geometry, we performed impulse-response FDTD simulations. Using incident laser pulses with 3-fs FWHM duration, we simulate the time-resolved electric field at the structure center, $E_{\text{z,center}}(t)$. The spectral response in the linear intensity regime is described by the complex transfer function

T(ω), obtained from the Fourier transforms of the time-dependent incident and enhanced fields[109]:

$$E_{\mathrm{z,center}}(\omega) = T(\omega) E_{\mathrm{x,inc}}(\omega) \tag{6.13}$$

The frequency-dependent field enhancement is then given by $|T(\omega)|$. We also use eq. 6.13 to compute the temporal response for Gaussian incident pulses of varying duration.

We first study the four-ring bullseye lens optimized above (see Figure 6.2). The simulated incident and enhanced electric fields over time are shown in Figure 6.3a. Notably, the plasmonic field is stronger than the incident laser field, but lasts more than 10 fs longer. In the next section, we will show that some of this broadening is due to the delay in arrival of plasmons generated from outer rings relative to inner rings. This leads to a spectral response with finite bandwidth, shown in Figure 6.3b as a function of incident photon wavelength. There is a strong peak at 800 nm, which we attribute to a surface plasmon resonance in the center plateau. The grooves in this structure are deep enough to disturb SPP propagation and modify their dispersion, leading to additional peaks and valleys in the response (see Figure 6.13). Additional peaks have been observed experimentally in transmission spectra of plasmonic lenses with a central aperture [110] and computational work finds significant dispersion modification in deep gratings, such as opening of plasmonic bandgaps [111].

Effects on the response shape for varying incident pulse length (I_{inc} FWHM) are shown in Figure 6.3c. Longer pulses generate a Gaussian response with peak field enhancement identical to that for cw illumination. On the other hand, for pulse lengths of tens of femtoseconds, there is substantial temporal broadening and the plasmonic field amplitude is reduced. These effects on the response strength and duration are quantified in Figure 6.3d-e. We note that the FWHM durations in Figure 6.3e are set by the main peak in the temporal envelope, while the tails are suppressed due to the scaling of four-photon photoemission with the intensity ($J_4(t) \propto I^4(t)$) [108]. As a result, the response duration is mostly linear with the input pulse duration, always about 3.5 fs longer due to the propagation delay between rings. For few-femtosecond pulse lengths, there are deviations from linearity which may be related to beating and envelope asymmetry. Still, this lens is predicted to be capable of producing sub-10 fs photoelectron pulses.

Tuning the response by geometric design

We now present a series of impulse-response simulations while varying geometric parameters to clarify design rules for ultrafast photoemission applications. We first vary the number of rings, N, obtaining the simulated spectral response shown in Figure 6.4a. For $N = 1$, the bandwidth extends over the entire wavelength range studied, and there is a plasmonic resonance peak at 800 nm. Adding more rings increases the field enhancement by coupling more light, but it shrinks the bandwidth by increasing the SPP propagation distance, and hence delay time, between inner and outer rings. This generally increases the peak field enhancement for varying incident pulse length shown in Figure 6.4b while increasing the response duration as shown in Figure 6.4c. For few-femtosecond pulses, however, there is a limit to the number of added rings that increase field enhancement, beyond which the delay time between inner and outer plasmons is too long for them to overlap. In this limit, adding additional rings only increases the pulse duration without increasing field enhancement, shown

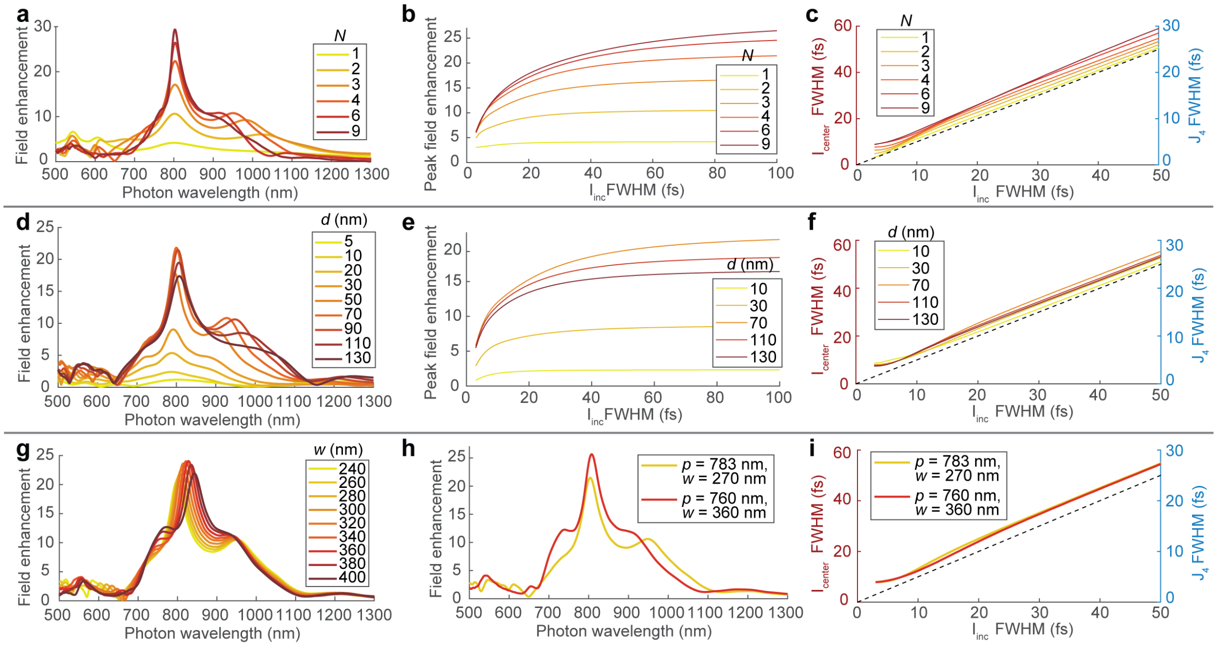

Figure 6.4: Geometric tunability of the simulated enhancement and temporal response. Top row varies number of rings, N. The grating period $p = 783$ nm, groove width $w = 270$ nm, groove depth $d = 90$ nm, and center plateau radius $r_i = 783$ nm. **a** Transfer function computed for lenses with N ranging from 1 to 9. **b** Maximum field enhancement at the lens center for incident pulses with varying temporal full width at half maximum (FWHM). **c** Temporal FWHM of the electric field intensity at the lens center (I_{center}) for incident pulses with varying temporal FWHM. The temporal FWHM of the four-photon photocurrent density J_4 is half of the I_{center} FWHM. **d-f** are the same, but for varying d, keeping $N = 4$. **g** Transfer function computed for lenses with varying w and grating period $p = 783$ nm. **h** Transfer function computed for the lens studied in Figure 6.2 ($p = 783$ nm, $w = 270$ nm) and for a lens with w chosen to maximize field enhancement and p adjusted to center the peak wavelength near 800 nm ($p = 760$ nm, $w = 360$ nm). **i** Response duration for the two lenses in panel h.

in Figure 6.4b-c at the shortest pulse durations.

We then vary the depth of the grooves, d, obtaining the spectral response shown in Figure 6.4d. As d increases, the field enhancement increases, saturates, and eventually decreases. While deeper grooves couple more incident photons to SPPs, they also inhibit SPP propagation to the center, leading to an optimal depth that maximizes field enhancement. The resonance peak at 800 nm emerges and grows with increasing d as reflectivity of plasmons from the grooves increases. Other peaks and valleys also emerge, suggesting the deeper grooves are disturbing plasmon propagation and modifying their dispersion and interference. The peak field enhancement for varying incident pulse length scales similarly with d as shown in Figure 6.4e. Again for few-femtosecond pulses, plasmons from the outer rings cannot reach those from the inner rings and so the field enhancement is reduced. There is also a noticeable effect of d on the temporal response duration as shown in Figure 6.4f. For longer pulses, the duration seems to scale with the strength of the resonance contribution, which would extend the plasmonic field duration. Overall, d has less of an effect on the pulse duration than N.

Next, we vary the ring width, w, computing the transfer functions shown in Figure 6.4g. Maximal field enhancement is achieved for $w = 360$ nm, close to half the period. Adjusting the width also shifts the resonance peak. Wider groove obstacles may more strongly obstruct plasmon propagation, affecting the plasmon dispersion relation. This shift in resonance peak can be compensated by adjusting the bullseye grating period, p. The transfer function and temporal response of a four-ring lens optimized by allowing variable p is shown with the one obtained by fixing $p = 783$ nm in Figure 6.4h. The peak field enhancement and the symmetry of the transfer function are improved by using $w = 360$ nm and compensating for the resonance peak shift by setting $p = 760$ nm. This provides a factor-of-4 increase in the estimated four-photon photoemission yield. This comes without cost in response duration, as shown in Figure 6.4i.

These results lead to a few design rules for ultrafast applications. The depth and width of the grooves should usually be optimized for maximum field enhancement. The period can then be adjusted to center the resonance peak at the desired wavelength. Finally, the structure should have as many rings as possible to maximize photocurrent while maintaining enough bandwidth to achieve the required pulse duration. The optimal geometry ultimately depends on the photocurrent and pulse duration required.

6.3.2 Prototyping and electro-optical characterization

Fabrication

Table 6.1: Topographic comparison between EBL and FIB bullseye lenses via AFM

	FIB	EBL
Groove depth (nm)	51	54
Center RMS roughness (nm)	1.4	0.4
Groove RMS roughness (nm)	3.2	0.6

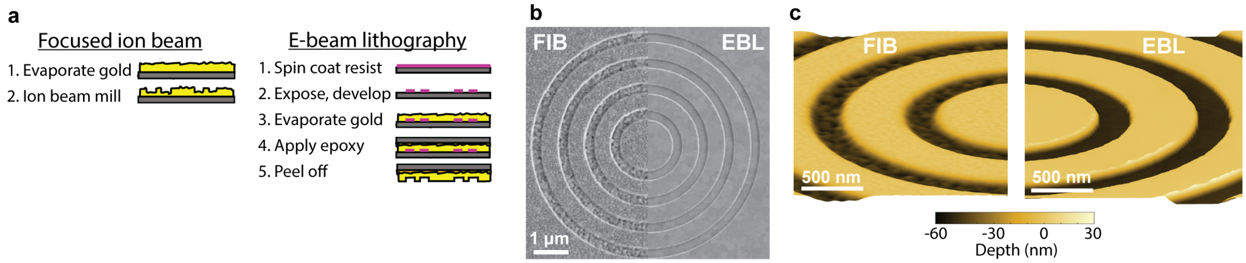

Figure 6.5: Bullseye lenses fabricated by two methods. **a** Process steps for FIB milling and for EBL with template stripping. **b** In-lens SEM images shown of the bullseye lenses made using FIB and EBL. **c** AFM surface topography maps shown of lenses made using FIB and EBL. Maps are displayed to-scale in 3D at a 40° tilt.

Bullseye lenses were fabricated using two processes illustrated in Figure 6.5. One process involves thermally evaporating 5 nm of titanium as an adhesion layer and 150 nm of gold onto a Si wafer, then carving out the rings using focused-ion-beam (FIB) milling. A Zeiss Crossbeam 1540 EsB was used for the FIB. The other process used electron-beam lithography followed by template stripping to produce high-precision, smooth cathode surfaces [112]. A negative e-beam resist hydrogen silsesquioxane (HSQ) 2% was spun at 1000 rpm onto a Si wafer. The resist was then exposed using a Vistec VB300 electron-beam lithography (EBL) system and developed, leaving the designed pattern in the form of amorphous silica on the wafer. Then, 150 nm of gold was deposited onto the template, entirely covering it. Finally, the patterned gold was peeled off using an electrically and thermally conductive ultra-high-vacuum compatible epoxy resin. Atomic force microscopy (AFM) measurements confirm that similar groove depths can be made in both structures, but the EBL and template stripping process yields smoother surfaces and grooves. In fact, structures made by EBL have nearly atomically flat central areas, which minimizes degradation of the emitted electron beam from surface roughness and imperfections [101] (see Table 6.1). In these lenses, the gratings are 50 nm deep with parameters otherwise matching the first case (783-nm period, 270-nm width, four rings): its simulated spectral response is shown in Figure 6.4.

Examining plasmonic properties

Cathodoluminescence (CL) spectromicroscopy measurements were then used to measure plasmonic characteristics of fabricated lenses. In CL, an electron beam is focused on the sample and, by one or more mechanisms, light is emitted from the material [113]. For plasmonic structures, the relevant mechanism is the broadband generation of SPPs by the fast-moving electrons as they strike the material surface. The SPPs propagate radially outward from a nanometric spot, which can then couple out to light through the bullseye grating [114, 115]. When the electron beam is at the bullseye center, circularly symmetric SPPs are excited like those that would be generated by a radially polarized laser.

CL allows to study a few key plasmonic properties in such structures. For one, the plasmonic resonance in the central region can be mapped using CL spectromicroscopy. CL intensity has been linked to the radiative local density of optical states (LDOS) at the electron

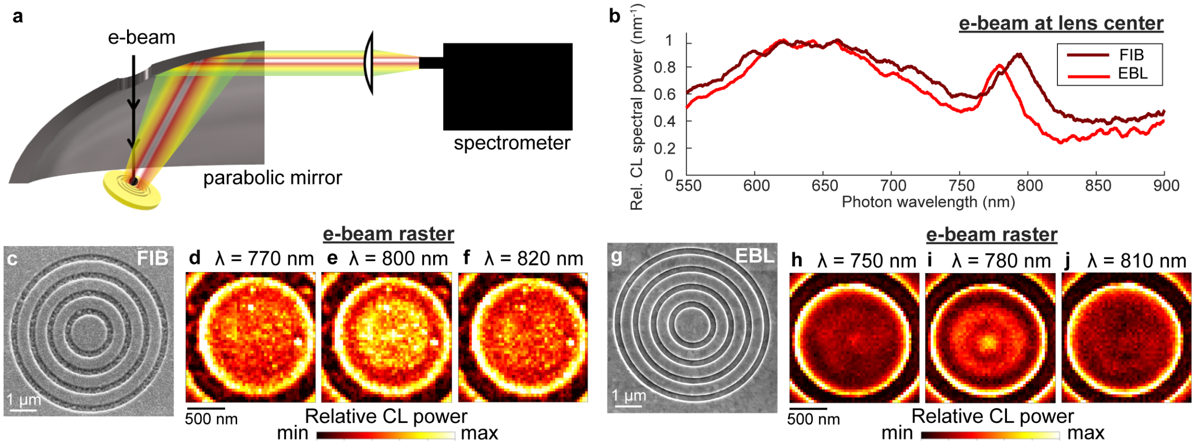

Figure 6.6: Cathodoluminescence (CL) spectromicroscopy of the plasmonic resonance. **a** A schematic of the CL spectromicroscopy technique. The electron-induced multicolor luminescence from a tilted lens is collected by a parabolic mirror and focused by a lens into a spectrometer. The electron beam is scanned and a full CL spectrum is collected at each beam position. **b** The average of CL spectra collected within 75 nm of the structure center, shown for one lens made by FIB milling and one by EBL. **c** A SEM image and **d-f** CL spatial maps of the lens made by FIB. **g** SEM image and **h-j** CL spatial maps of the lens made by EBL. CL spatial maps are obtained from the spectromicroscopy dataset by integrating over Gaussian wavelength bands with $2\sigma = 10$ nm. Each map is labeled with their corresponding center wavelength, λ.

beam position, ie. the number of optical modes available at the excitation position that produce light [114, 116]. The LDOS is enhanced by plasmonic resonance, so CL can be used to spatially and spectrally resolve resonance modes [117, 118]. Spatial homogeneity, circular symmetry, and a strong, sharp central peak are desirable for photoemission applications. The center wavelength and bandwidth of this resonance can be extracted from the CL spectrum obtained at the structure center. Also, the radial extent and circular symmetry of plasmon propagation and grating coupling can be inferred by angle-resolved imaging of the CL far field, which is essentially a Fourier transform of the real-space emission profile of the structure. These are important to characterize since significant propagation losses or asymmetries in coupling would reduce the field enhancement under laser illumination.

We used a modified Zeiss Gemini SUPRA 55 SEM for our CL measurements. The sample was positioned at the focal point of a horizontal Al parabolic mirror with 1 mm focal length. A 10-keV electron beam was focused onto the sample, and the emitted light was collected by the parabolic mirror over a wide angle range (0° - 80° from normal) and over the entire visible spectrum and beyond. The sample was tilted by about 25° so that the highly directed, normal emission would not escape through the entry hole in the mirror for the electron beam. We do not expect this tilt to change the plasmonic response; there will not be significant arrival time delay across the electron beam since it is much smaller than the plasmon wavelength. Also, the electron beam only generates SPPs at the surface, so the source size is only made about 10% larger along the tilt direction.

CL spectromicroscopy of plasmonic resonance

We used scanning CL spectromicroscopy to probe the spectral and spatial characteristics of the surface-plasmon resonance in our fabricated lenses. The electron beam is rastered step by step over the central plateau of the structure, and a full CL-emission spectrum is collected at each beam position. Spectra are obtained by focusing the reflected light from the mirror onto a multi-mode optical fiber with a 200 μm diameter and then dispersing it using a spectrometer consisting of an Acton 2300i monochromator (150 line/mm, 500 nm blazed grating) and Andor Newton electron-multiplied charge-coupled device (CCD). The dark current background is subtracted and spectra are normalized by the instrument response over the measured wavelength range. The open-source Python-based ScopeFoundry software developed to control this experiment is available online for further reference [119, 120]. From this 3D data set, we extracted average emission spectra from regions of interest. Average spectra over the region within 75 nm of the bullseye center are shown in Figure 6.6a. Spectra shown here are smoothed using a second-order Savitsky-Golay filter with 15-nm window. The CL emission spans the entire detection spectral range. This is because a SPP of any wavelength from the broadband range generated by the electron beam can satisfy the grating equation and couple to light at a wavelength-dependent emission angle, and nearly all emission angles are collected by the parabolic mirror. However, there is a notable emission peak near 800 nm where a surface plasmon resonance is expected.

We can then examine the spatial profile of the plasmonic resonance. We apply virtual Gaussian bandpass filters with $2\sigma = 10$ nm to the entire dataset, yielding maps of CL emission over narrow spectral bands as a function of beam position [see Figure 6.6c-j]. For maps of emission near the resonance wavelength, a zero-order Bessel-function spatial profile is observed corresponding to a cylindrical plasmonic resonance of the central plateau. For the maps at wavelengths just outside of the resonance peak, such a spatial profile is not observed, confirming that it is a resonance effect. For the structure made by EBL, the CL intensity is higher when the structure is excited at the central peak antinode than at the nearby annular antinode. For the structure made by FIB, however, the CL intensity is similar when exciting at either antinode. This suggests that the constructive interference of SPP modes from different directions is improved in the EBL structures, leading to a stronger central peak.

Other features in the maps are also present off resonance. For instance, bright spots are present in the map of the FIB-milled structure [Figure 6.6d-f] which correspond to bright signals in the secondary electron image [Figure 6.6c]. The groove edges are brighter in both structures regardless of wavelength. These correspond to topographic features with locally high surface area and roughness, which can enhance the radiative LDOS by scattering more SPP modes out to light. The near-atomic smoothness of the central region in the EBL structures eliminates the scattering sites observed in the FIB structure. This will reduce damping of the resonance and thereby improve the field enhancement under laser illumination and consequently the amount of emitted electrons.

We note that there are key differences between CL mapping and the FDTD simulations used in section II. The excitation mechanism is different: FDTD simulates a radially polarized laser excitation and calculates the field enhancement at all positions, whereas CL

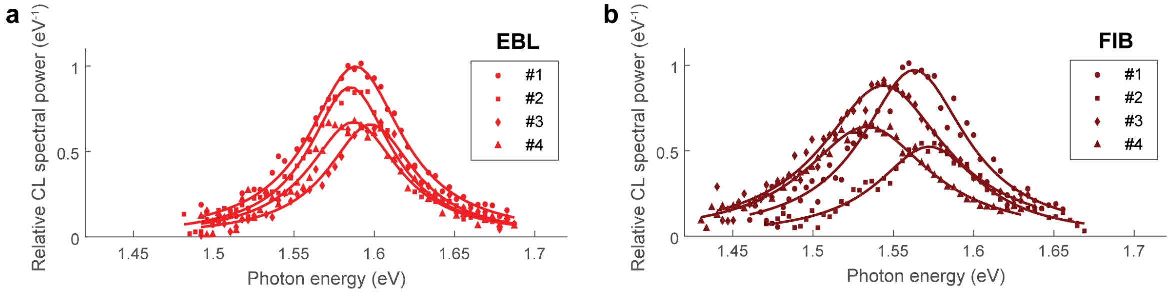

Figure 6.7: A comparison of the plasmonic-resonance characteristics of bullseye lenses made by EBL and FIB milling using CL spectroscopy. Resonance peaks are shown for four lenses made using **a** EBL and **b** FIB. The spectra are fitted with a parabolic background plus a Lorentzian over a 0.2-eV range centered at the peak. Points indicate data over the fitting window after the background is subtracted, while lines indicate the Lorentzian peak fit to the data.

mapping rasters an e-beam and collects the integrated light output as a function of e-beam position. This scanning local excitation provides a different spatial profile than expected for a global laser excitation based on FDTD. For instance, the CL emission is stronger when the electron beam is positioned at edges than the structure center, but this is not expected for the case of radially polarized illumination. Still, we can use CL mapping to visualize scattering sites and study the symmetry and smoothness of the plasmonic resonance mode, as discussed above. For more detailed discussion of the CL dependence on electron beam position, see the Appendix of the published article[79].

To quantify and compare the resonance characteristics of structures made by FIB and EBL, we fit the resonance peaks in CL spectra collected using an e-beam at the lens center (where the plasmons generated match the circular symmetry of the structure) to determine the resonance wavelength and the FWHM. Average spectra from scan positions within 75 nm of the bullseye center are extracted from spectromicroscopy scans. The spectra are then re-binned into 2-nm wavelength bins and converted from wavelength to energy scale. The resonance peak is fit using a Lorentzian plus a parabolic background. Four structures made by each fabrication method were measured and analyzed. The converted spectra and peak fitting are shown in Figure 6.7. The average resonance wavelength is 798.4 ± 8.8 nm standard deviation for the FIB-milled structures and 779.6 ± 2.4 nm for the EBL structures. Both are near the 794-nm resonance wavelength predicted by FDTD for structures with the fabricated dimensions. The average measured frequency-to-FWHM ratio, or Q factor, is 17.8 ± 2.0 for the FIB-milled structures and 23.9 ± 1.9 for the EBL structures. The more precise resonance wavelength and higher Q factor (lower damping) of the EBL structures can be attributed to the reproducibility of the structure dimensions and their smoothness.

Angle-resolved CL and photon-plasmon coupling

We then studied the angle-resolved CL emission to infer the radial extent of effective plasmon propagation and grating coupling in the fabricated lenses. We both simulated and measured the CL far field for four- and 12-ring bullseye lenses. The far field is measured by positioning the electron beam at the structure center and imaging the parabolic mirror [121, 122]. Because the emitting structure (several micrometers) is small compared to the distance from the mirror (1 mm), the position where an emitted photon reflects from the mirror is determined by the emission angle. The parabolic mirror brings the emission to infinity focus, which is filtered by a bandpass filter centered at 800 nm with 40 nm bandwidth and then magnified and imaged onto a ThorLabs DCC3260M CMOS camera. For each measurement, 30 one-second exposures of the CCD are acquired and averaged. A background image with the beam blanked is acquired under the same conditions and is subtracted from the beam-on image. Then, each pixel in the image is mapped to an emission angle, and the signal is normalized by the solid angle collected by that pixel to give an intensity map. The measured far field is then corrected for tilt and rotation of the sample relative to the mirror.

Using FDTD, the CL process can be numerically modeled [107]. An impinging 10-keV electron at the center of the bullseye is modeled using a series of dipoles normal to the surface. The dipoles are delayed in phase to create a propagating, localized source of electric field. This generates a time- and z-dependent current density close to that of a moving electron [123]: $\vec{J}(t,z) = -ev\hat{z}\delta(z-vt)\delta(x-x_0)\delta(y-y_0)$. Here, e is the fundamental charge, v is the speed of the impinging electron, $\hat{z}$ is the unit vector in the z direction, and x_0 and y_0 give the lateral position of the impinging electron. The resulting field decays laterally, and vanishes within a few nm in the metal; therefore, no field can directly couple to the grooves, and all observed emission is due to generation, propagation, and outcoupling of SPPs. To avoid abrupt appearance and disappearance of the dipole field, which would create stray fields, a raised-cosine filter is used to gradually increase and decrease the amplitude oscillations of the starting and ending dipoles in time. The simulation box was gradually increased in order to collect larger angles and mesh dimension was decreased to achieve convergence.

Simulated and measured far-field CL of four-ring lenses are shown in Figure 6.8a-c. A donut beam is observed in all cases, supporting that the emission is radially polarized. Other work performing CL polarimetry on bullseyes has resolved the angle-dependent polarization state and verified that the emission is radially polarized [124]. Both the angle of maximum emission and the overall angular distribution measured for lenses made by EBL and FIB closely match that predicted using FDTD (see Figure 6.8d). This indicates that the radial distribution of CL emission from plasmon-photon coupling is robust to fabrication imperfections, including the surface roughness of the FIB-milled structure. These measurements also show that this normally directed emission is captured effectively at 25° sample tilt; this supports the validity of the spectra shown above and demonstrates the need for tilting the sample to study this emission.

We also fabricated and studied a 12-ring bullseye lens using FIB as shown in Figure 6.9a. The simulated and measured far-field for this structure are shown in 6.9b-c. Again, a donut beam is produced as expected. The far field is more asymmetric than for the four-ring structures, which may be due to challenges in making the outer rings accurately concentric with the inner rings using FIB. Still, the angular breadth of emission is greatly reduced, indicating that the plasmons can outcouple over a greater radial extent. As highlighted in Figure 6.9d, the peak emission angle is 3°, whereas in the four-ring lenses it was 7°. The distribution matches well between simulation and experiment overall, especially at less than 5°. This suggests that additional plasmon propagation losses due to polycrystallinity are not

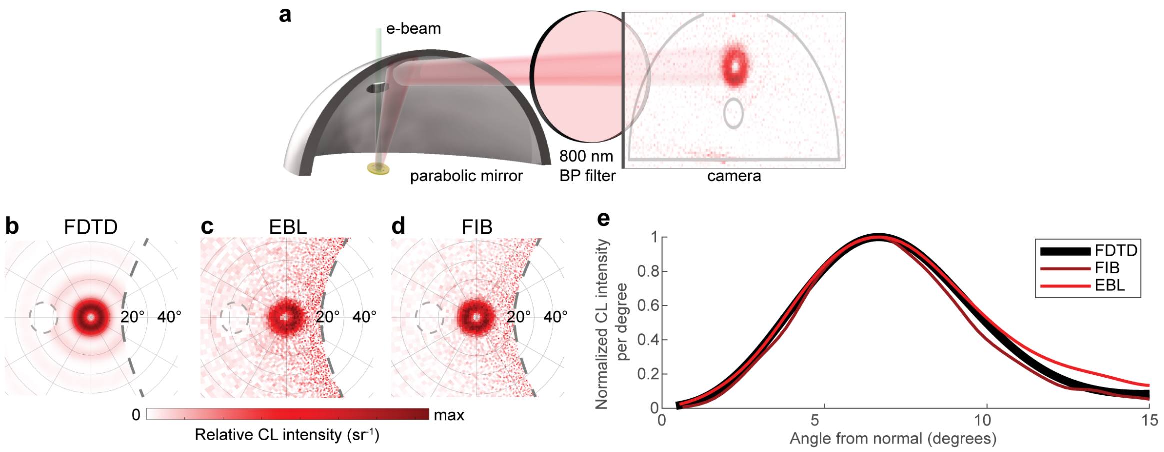

Figure 6.8: Angle-resolved cathodoluminescence (CL) with e-beam at the structure center. **a** A schematic of the Fourier imaging technique. The parabolic mirror is imaged through a band-pass (BP) filter centered at 800-nm wavelength with 40-nm bandwidth. Far field plots are then generated by transforming mirror coordinates to angular coordinates. The sample is tilted at 25° so emission is not lost through the entry hole for the electron beam. **b** The FDTD-simulated far field. CL far field polar plots for lenses made using **c** EBL and **d** FIB. The gray dashed lines trace the electron-beam entry hole and the open face of the parabolic mirror. **e** CL distributions per degree from normal obtained by azimuthal integration of the far field.

a limiting factor even for this 12-ring structure.

6.3.3 Implications for future source development

This work introduced the concept of using plasmonic lenses as ultrafast nanoscale electron emitters and identified important aspects of geometric design and fabrication for this purpose. Importantly, it predicts that a single dominant central peak in optical intensity can be generated to generate electron pulses with 140-nm FWHM (60-nm RMS) lateral size. This size is independent of most geometric parameters, which are free to be tuned to optimize the photocurrent and temporal response for application requirements. Also, the computations and experiments shown here support that the plasmonic properties and the spectral bandwidth of such structures are compatible with emission of sub-10-fs pulses. Finally, it shows that by using a template stripping procedure, the emission surface can be made nearly atomically flat to minimize SPP scattering and avoid surface-roughness induced emittance growth.

These plasmonic lenses could also facilitate emerging high-intensity modes of operation. For instance, they reduce the laser power required to access the optical field emission regime, in which the fields are strong enough to modulate the work function at the optical frequency. This operating regime is of great interest because it allows control of the photocurrent density at attosecond timescales, providing the potential to generate attosecond electron-pulse trains [96]. In addition, the compatibility of these lenses with few-cycle pulses could allow control of the photocurrent intensity by tuning the carrier envelope phase, as has been demonstrated for tip emitters [97].

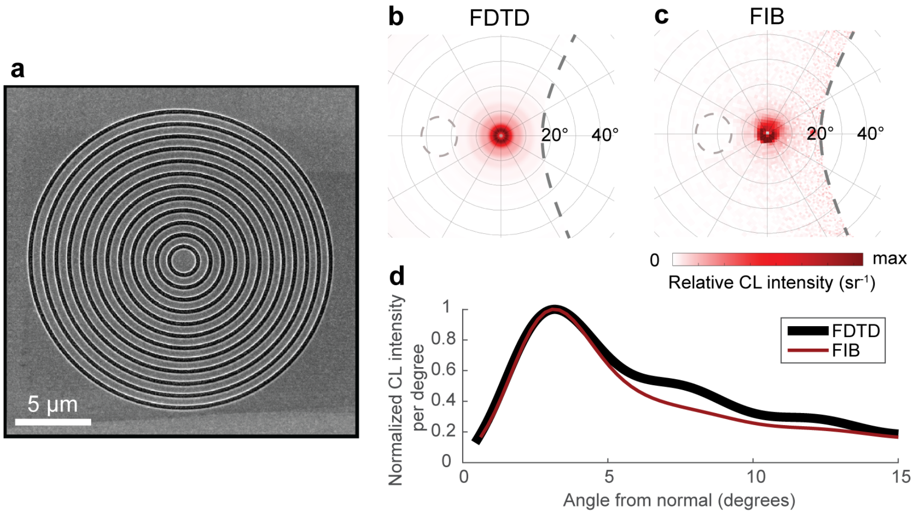

Figure 6.9: Angle-resolved cathodoluminescence (CL) for a 12-ring lens milled using focused ion beam (FIB). **a** A SEM image of the 12-ring lens. The FDTD-simulated (**b**) and experimentally measured (**c**) CL far-field polar maps for the electron beam positioned at the center. The gray dashed lines trace the electron-beam entry hole and the open face of the parabolic mirror. **d** The emission distribution along angle from normal obtained by azimuthal integration of the far field.

The transverse brightness of such nanocathodes is expected to be more than 1 order of magnitude better than present state of art flat cathodes. Such sources have applications beyond UED including RF photoinjectors for advanced acceleration devices [125]. As for UED, such sources could be the key to generate brighter ultrafast nanoprobes and improve ultrafast nanodiffraction and nanoimaging capabilities.

Improvements to the design shown here are being actively pursued. For instance, using spiral plasmonic lenses instead of bullseyes relaxes the requirement for precise alignment of the incident laser to the plasmonic structure[126, 127]. Also, the geometry can be modified to compensate for the angle of incidence of the laser.

6.4 DC photogun for testing and characterizing plasmon-enhanced photoemitters

Having optimized and optically characterized the plasmonic lens design, the next critical step to demonstrating this novel photocathode is to measure and characterize photoemission from such prototypes. These structures pose a few measurement challenges. For one, the maximum charge per pulse will be on the order of a few electrons due to the space charge limit, demanding high repetition rates and low-noise detection to record the signals. Second, the small transverse emittance will be difficult to characterize. Thirdly, due to the multiphoton photoemission process used, the measured signals will be highly sensitive to energy and position jitters of the laser excitation, demanding precise laser stability on the sub-micron scale.

This section describes the development and demonstration of a DC photogun setup at

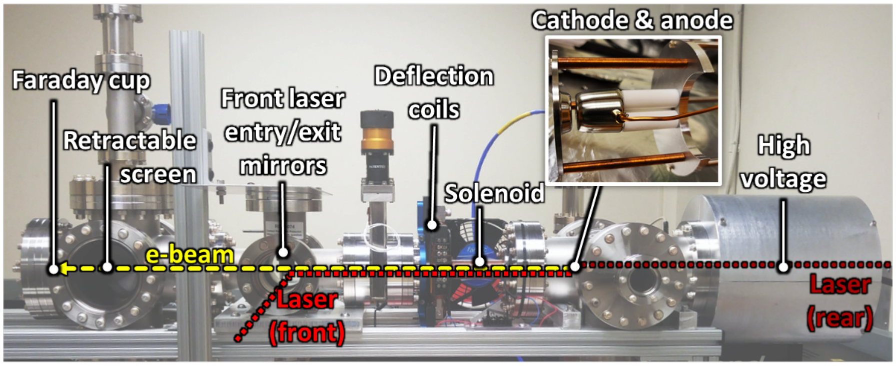

Figure 6.10: Photograph of DC photogun at LBNL with schematic labeling of components and beam paths. Inset shows the cathode and anode assembly.

LBNL which has been specially equipped to characterize low-charge, coherent emitters such as these. The photogun was tested using a polished Cu photocathode as well as a gold plasmonic nanogroove cathode.

6.4.1 DC photogun setup and characteristics

The DC photogun setup at LBNL is shown in Figure 6.10. Up to 30 kV DC can be applied to the emitter as well as both rear and front optical illumination. The emitted electron beam first traverses a solenoid electromagnet, enabling focusing and solenoid-scan emittance measurement, followed by horizonal and vertical dipole steering electromagnets. Electron beams can be characterized by imaging using a phosphor screen or collecting them with a Faraday cup to measure photocurrent. Low-noise photocurrent measurements can also be performed between the cathode and anode directly under a low DC bias (tens of volts) using a lock-in amplifier locked to the frequency of a chopper.

At present, the setup is equipped with a Femtolasers Ti:Sa oscillator well suited for ultrafast nanoemitters. The 80 MHz repetition-rate allows to extract pA-level currents from single to few-electron emitters. This is important because positive charge left behind at the surface imposes a restoring field, limiting the number of electrons per pulse that can be extracted, especially in a low-voltage gun from a nanometric area. The formula for this space charge field is $E_{sc} = \frac{Q}{A\epsilon_0}$, where Q is the charge per pulse, A is the emission area, and ϵ_0 is the vacuum permittivity. Using this, we can estimate the space charge field contributed by each additional electron within a pulse being extracted from a nanoemitter. Using the plasmonic lens described in section 6.3.1 as an example, we determine the emission area by approximating the emission as a flat-top distribution with radius equal to the half-width at half-maximum (about 71 nm), giving an area of 1.6×10^4 nm^2. Then, each electron extracted contributes 1.1 MV/m. The DC gun applies at most 30 kV across a 3 mm gap, providing a maximum field of 10 MV/m. This suggests the emitted charge in this case will be limited to less than 10 electrons per pulse, or less than 125 pA at 80 MHz repetition rate. The limit on charge per pulse is independent of the pulse energy available, motivating the use of high repetition rate lasers and high extraction fields where high currents are needed from such nanoemitters.

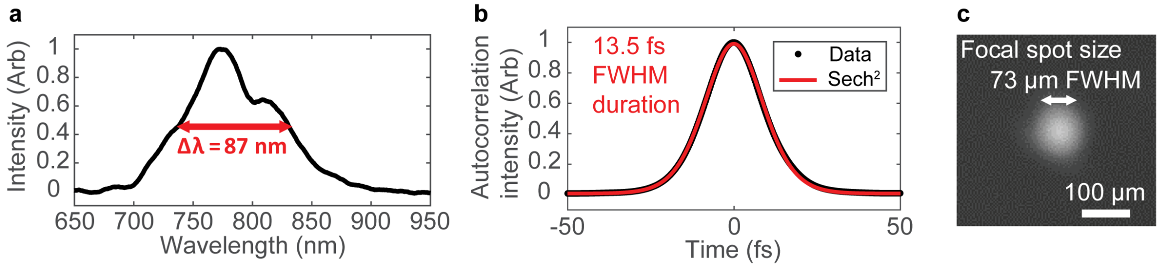

Figure 6.11: Characterization of the Ti:Sa oscillator used for photoemission experiments. **a** Spectrum. **b** Autocorrelation at the output of the laser. **c** Beam image at the virtual cathode camera.

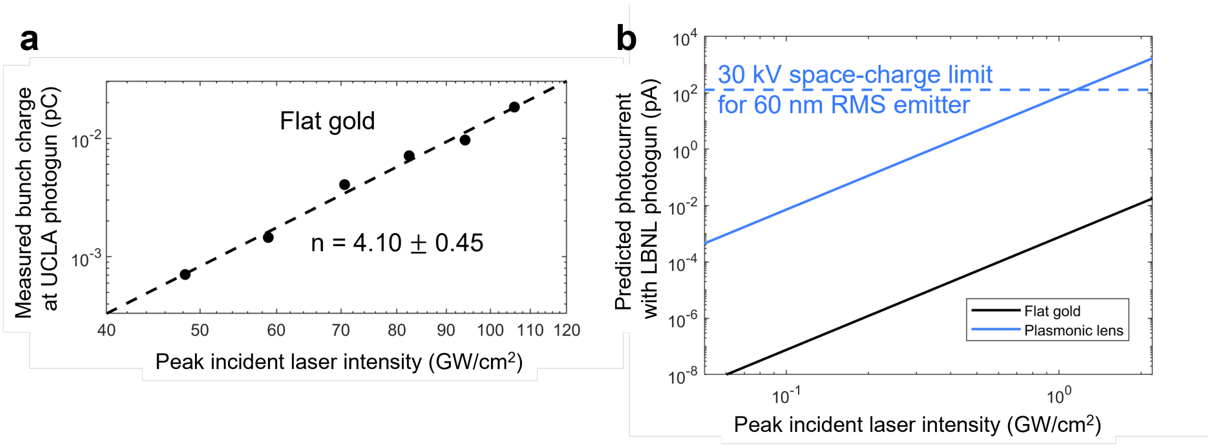

Figure 6.12: Determination of expected photocurrent from plasmonic lens nanoemitters in the LBNL DC photogun. **a** Measurement of multiphoton photoemission from a flat gold film on a similar setup at UCLA to verify 4-photon process and extract photoemission probability. **b** Calculations of expected photoemission at LBNL setup from a plasmonic lens compared to flat gold.

For multiphoton photoemitters, high optical field intensity is crucial and so short pulse duration and small focal spots are an advantage. These were characterized for our setup and are shown in Figure 6.11. The Ti:Sa oscillator produces 500 mW of power with a bandwidth of about 87 nm FWHM and a pulse duration of less than 13.5 fs FWHM. We have so far achieved focal spots at the cathode as small as 71 μm FWHM. While it is challenging to focus smaller with bulk optics given the geometry of the setup, particularly the distance between the laser entry viewport and photoemitter, plasmonic lens emitters help to overcome this limitation by concentrating the light incident over the entire lens area to a wavelength-scale central spot.

6.4.2 Predicted photocurrent from plasmonic lenses

We can show that the laser parameters are sufficient to reach the space charge limit for the plasmonic lens nanoemitter described in Section 6.3.1. For an n-photon photoemission process, the charge per pulse Q is related to the optical pulse parameters by $Q = CAtI^n = C\frac{E^n}{\tau^{n-1}A^{n-1}}$ where I is the peak optical intensity, E is the optical pulse energy, τ is the optical intensity duration ($\sqrt{2\pi}\sigma_t$ for a Gaussian pulse, where σ_t is RMS pulse duration), A is the optical intensity spot area ($A = 2\pi\sigma^2$ for a Gaussian beam, where σ is the RMS spot size), and C is a wavelength- and material-dependent proportionality constant[95]. To determine C for 800 nm wavelength light on flat gold, we performed photoemission measurements at a similar DC photogun at University of California, Los Angeles (UCLA). These measurements used an amplified Ti:Sa laser with about 50 μm RMS spot size, 100 fs FWHM pulse duration, and incident pulse energy varied from 0.8 μJ to 1.8 μJ. we were able to verify a 4-photon process by performing a power law fit to Q as a function of I, shown in Figure 6.12a. Then, by fixing n to be 4 and fitting the curve again (not shown in the plot), we determine $C = 10^{-5.02\pm0.02}\ \frac{\mathrm{A}}{\mathrm{cm}^2}/(\frac{\mathrm{GW}}{\mathrm{cm}^2})^4$.

We then calculated the expected photocurrent for flat gold and the 4-ring gold plasmonic lens for the LBNL setup. Photocurrent, i, is given by $i = f_{rep}Q$, where f_{rep} is the repetition rate (80 MHz for our laser) and Q is the charge per pulse. We consider a range of pulse energies from 0.02 nJ to 2 nJ (about a third of the full laser power). For the flat gold, we consider the laser parameters discussed above to compute Q: 71 μm FWHM spot size and 15 fs pulse duration, assuming optimal focusing and pulse compression at the cathode. The plasmonic lens, however, modifies the optical intensity profile at the surface, focusing the RMS spot size to $\sigma = 161$ nm and increasing temporal duration by about 4 fs, as described in section 6.3.1. In doing so, the peak optical field is enhanced by about 15 times. The optical pulse energy concentrated into the lens center is calculated using $E_{nano} = F^2 A_{nano} t_{nano} I_{inc}$ where F is the field enhancement factor, nano subscripts refer to the nanofocused optical intensity, and I_{inc} is the peak incident laser intensity. We find that only 0.84% of the incident laser pulse energy is coupled into a single plasmonic lens in this case, mainly because the incident beam is more than 10 times larger in diameter than the 4-ring bullseye lens. The predicted photocurrent as a function of the laser power is shown in Figure 6.12b. We predict nearly 100,000 times greater photocurrent from the plasmonic structure compared to the flat gold, allowing to characterize the emission from the structure with negligible photoemitted background current from surrounding areas. Furthermore, these calculations suggest that with our laser parameters, we should be able to achieve the maximum allowed photocurrent from the plasmonic lens nanoemitter at 30 kV and measure the onset of virtual cathode formation.

We note that higher total photocurrent could be obtained by measuring an array of lenses simultaneously. In such a case, a high degree of reproducibility as afforded by the electron-beam lithography method discussed in section 6.3 is crucial for accurate characterization. Meanwhile for a single lens, the photocurrent can be enhanced by increasing the number of rings, thereby coupling more incident laser power into the structure. However, this comes at the expense of longer response time (more time delay between SPPs generated at inner and outer rings, as shown in section 6.3.1) and the maximum photocurrent is still set by the space-charge limit.

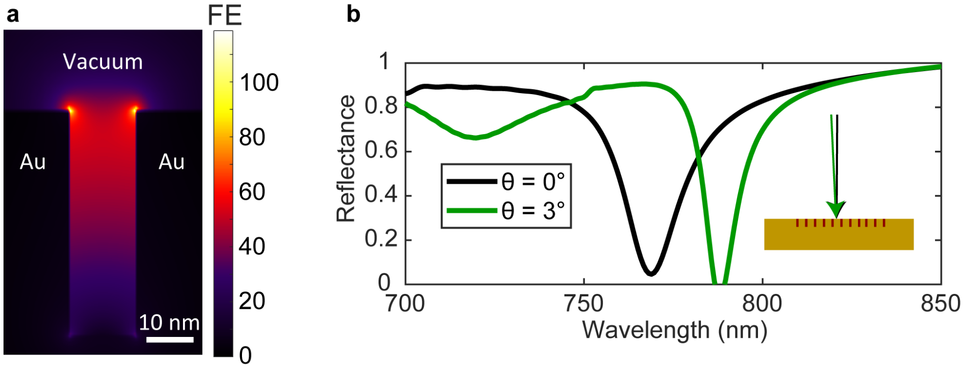

Figure 6.13: Simulated electromagnetic response of a resonant nanogroove photocathode designed for laser illumination with 790 nm wavelength at 3 degrees angle of incidence. **a** Cross-sectional field enhancement map through a groove in an array. **b** Calculated reflectance spectra for illumination incident at 0 and 3 degrees from the surface normal.

6.4.3 Demonstration on nanogrooves

Nanogroove cathode design

The nanostructured photocathodes tested are periodic arrays of nanoscale grooves in gold, similar to those described in refs. 91, 93. Here, the individual grooves exhibit a surface plasmon resonance mode which can be enhanced by arranging them in a periodic array to produce a coupled, long-lived diffractive photonic mode[92]. The hybridized modes can achieve a higher Q factor and larger enhancement than the isolated plasmon resonance. Using the Lumerical software[107], we performed finite-difference time-domain (FDTD) electromagnetic simulations to calculate the electric fields, and optimized the geometric parameters (width, depth, periodicity) to maximize the field enhancement achieved when illuminated with our laser parameters (described in section 6.4.1). The illumination wavelength is ≈ 790 nm, which can be used to produce 4-photon photoemission from gold as shown in the previous sections, and is incident at 3 degrees from the surface normal in the photogun.

The electromagnetic response of a resonant nanogroove structure designed for our laser geometry is illustrated in Figure 6.13. The structure simulated has width = 14 nm, depth = 45 nm, and period = 700 nm. The cross-sectional field map in Figure 6.13a illustrates the spatial localization of the enhancement at the surface-level edges of the grooves. Due to the scaling of 4-photon photoemission with fourth power of the intensity (eighth power of the field magnitude), photoemission will be strongly localized at those high enhancement points. These simulations use sharp corners, whereas in practice the edges will be rounded off somewhat and so localization and enhancement will be lower than computed here. That the emission is mainly from corners is worth noting, as it could lead to increased angular divergence of emitted electron beams along the grating vector. Cathode surface roughness has previously been shown to increase beam emittance[101].

The resonant character of the grooves is exemplified by the spectral response in Figure 6.13b. We show the reflectance at both normal incidence and 3 degrees from normal. The geometry studied here was chosen to optimize the enhancement at 3 degrees: in this

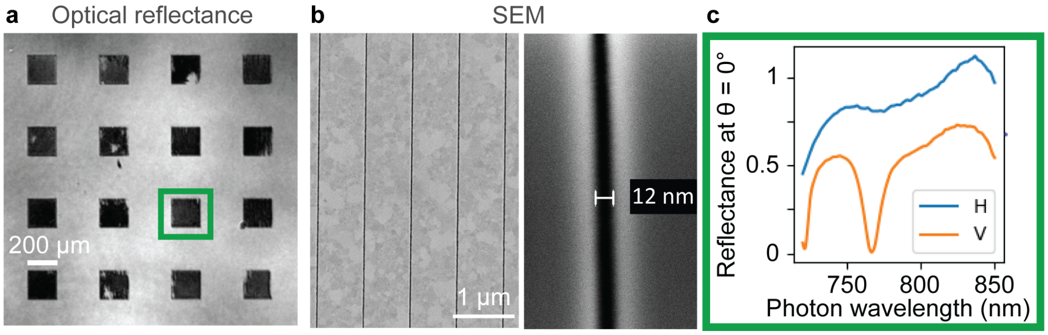

Figure 6.14: Electron and optical imaging of fabricated nanogroove photocathode. **a** Optical reflectance image of a 4 x 4 grid of nanogroove arrays recorded using normally incident Ti:Sa laser illumination with polarization aligned to the grating vector. **b** Scanning electron microscope (SEM) image of a single nanogroove grating and **c** of a single groove. **d** Reflectance spectra measured for the nanogroove array in the green box of panel a with polarization parallel (V) and perpendicular (H) to the grating vector.

case, the photonic and plasmonic modes are strongly hybridized, providing a narrow bandwidth and shifting the resonance wavelength. The optical reflectance is peaked near 790 nm with a bandwidth of 12.5 nm (Q factor = 62.5). At normal incidence, on the other hand, the resonance is peaked at 769 nm with a bandwidth of 21 nm (Q factor = 36.5). The optical response at normal incidence is characterized experimentally in the following section to verify that the structures behave as intended.

Fabrication and optical response

Nanogroove arrays fabricated for photoemission characterization are shown in Figure 6.14. E-beam lithography is used to write the groove patterns into a 2% hydrogen silsesquioxane (HSQ) negative resist spun at 1000 rpm. Onto this mask, gold is evaporated and then peeled off using an epoxy-coated glass chip. 200 μm × 200 μm square arrays are patterned in 4 x 4 grids, with the periodicity varying along one axis and groove width along the other to accommodate systematic process imperfection in the patterning dimensions (the $\approx$ 10 nm groove width is especially prone to error). The prescribed widths of each column are 8 nm, 10 nm, 12 nm, and 14 nm; the prescribed periods of each row are 670 nm, 680 nm, 690 nm, and 700 nm. A reflection image of a 4 x 4 grid is shown in Figure 6.14a, produced using the magnified laser beam polarized along the grating period. The arrays are dark in the image, indicating high absorption of the incident laser. SEM images of one set of grooves are shown in Figure 6.14b-c, illustrating the flat template-stripped surface and the nanoscale groove width. The reflectance spectra of the 690 nm pitch, 12 nm wide grooves over the laser bandwidth are shown in Figure 6.14d. They have a Q factor of $\approx$ 36 and resonance wavelength of 760 nm, similar to the simulated structures. As noted in the previous section, this resonance will be redshifted when illuminated at the 3 degree angle present in the experimental setup.

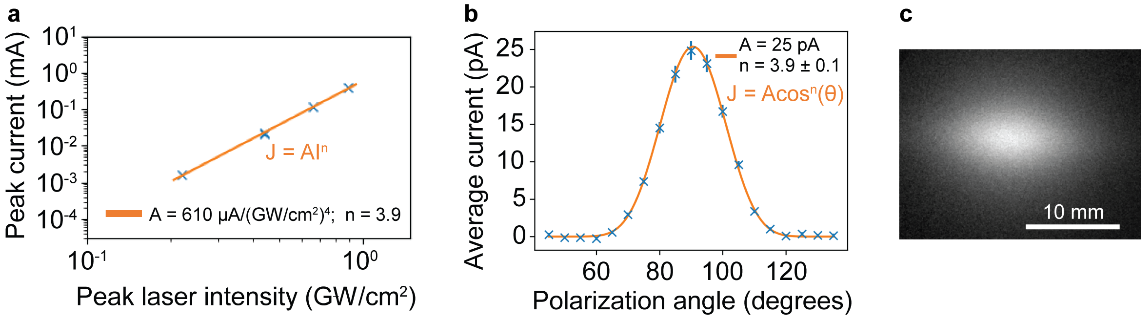

Figure 6.15: Photoemission measurements from the plasmonic nanogroove cathode in the DC gun. **a** Power dependent photocurrent. **b** Polarization dependent photocurrent. **c** Image of the photoemitted beam at the screen at zero solenoid current.

Photoemission measurements

Preliminary photoemission measurements of the fabricated resonant nanogrooves are shown in Figure 6.15. All measurements were performed on the set of grooves closest to the center of the cathode, ie. the one highlighted in Figure 6.14. We first measured the photocurrent as a function of incident laser power (Figure 6.15a), confirming a fourth order dependence expected for four-photon photoemission as shown in section 6.4.1. Average currents up to a few hundred nA were extracted from within the laser spot without damaging the grooves. We then measured the polarization dependence (Figure 6.15b), verifying the expected $J = \cos^4(\theta)$ form since only the component of laser intensity parallel to the grating vector $(I\cos(\theta))$ is absorbed.

Finally, we recorded an image on the final screen which shows the asymmetry of the emitted beam, suggesting an asymmetric transverse emittance. The observed asymmetry could be due to the geometry of the nanogroove photocathode, in which there is curvature at the corners at which electrons are emitted, but only parallel to the grating vector. Detailed modeling of the photoemitted beam properties from this nanogroove geometry as well as theoretical and experimental comparison to beams emitted from a flat gold surface will provide further insight into the origin of this asymmetry. In addition, ongoing work on solenoid scan measurements will precisely measure the transverse emittance components quantitatively and compare with simulated values.

6.4.4 Implications for photoemitter development

Altogether, these measurements demonstrate a new capability for characterizing plasmon-enhanced photoemitters at LBNL that can be used to examine nonlinear yield, space-charge limited current, emitter stability, polarization sensitivity, transverse dimensions of emitted beams, and more. This will be leveraged to characterize novel emitter designs such as the plasmonic lens emitters demonstrated in the previous section.

6.5 Future developments and applications of plasmon-enhanced photoemitters

The nascent field of plasmon-enhanced photoemission still holds great potential for advancing photocathode properties and room for innovation. The first clear milestone to be achieved is demonstration and characterization of photoemission from a plasmonic lens structure. Beyond this, demonstration of such cathodes in a transmission geometry would permit rear illumination, reducing optical components near the electron beam path and potentially allowing more efficient, higher numerical aperture focusing onto the structure[126, 127]. Emission from arrays of such structures can provide a multi-beam probe: this could in principle be used to record diffraction from multiple angles simultaneously, or in other applications such as multi-beam lithography. Addition of a nanotip or nanoparticle in the center of a plasmonic lens could provide additional confinement and enhancement of the field to provide higher coherence RF-compatible sources. Adapting the principles of these sources to lower MTE photocathodes would also provide significant gains in transverse brightness, either by utilizing plasmonics in metals with lower MTE or by coupling a plasmonic structure with additional low-MTE layers or structures. Strong-field or non-linear effects can be explored to achieve attosecond electron bunches. More complex spatial and temporal beam profiles can be explored by creative arrangement and design of SPP and SPR elements. The possibilities are numerous and extend well beyond higher brightness probes for UED. This is hopefully a field of research that will receive growing attention going forward.

Chapter 7:

Conclusions: Frontiers of UED

7.1 Summary of results

For many types of materials and processes, the quest to capture the atomic-scale dynamics in real time is a tremendous challenge. Expanding the frontiers of UED requires developments that leverage a wide range of disciplinary expertise. This doctoral thesis alone spans contributions to scattering theory, accelerator development, photoinduced phase transformations, beam characterization, plasmonics, and photoemission. In combination, these developments provide new routes to access the fundamental dynamics underlying ultrafast phenomena in materials, especially quantum and nanoscale materials. This lends great potential for UED to be used to discover and record novel ultrafast phenomena.

Chapter 2 *Multislice diffraction models to quantify atomic motions in crystals* presents a new multislice approach to more accurately compute UED patterns and quantify atomic motions in crystals. The procedure presented uses a mean-field approach to model the thermal motions and averages scattering patterns over the distribution of orientations within the probe to capture the main effects in UED. The procedure is demonstrated on single crystal gold films, retrieving a photoinduced lattice temperature rise that is three times larger than that retrieved using kinematical models and is in agreement with predictions based on the known optical constants of gold.

Chapter 3 *High Repetition-rate Electron Scattering* introduces the HiRES beamline, a new UED instrument which utilizes a state-of-the-art continuous-wave radiofrequency gun to achieve relativistic UED with unprecedented brightness. Schematics and specifications of the instrument are described. Also, pump-probe UED measurements with the increased repetition rate are shown, and experiment design considerations to make use of the increased repetition rate are discussed.

The work in **Chapter** 4 *Light-induced structural switching in* $TaTe_2$ applies the new pump-probe capability at the HiRES beamline to record a unique structural melt-recovery process in a quantum material for the first time. The UED measurements show that near-infrared excitation can melt the cryogenic trimer order on an ≈ 1 ps timescale, which then rapidly recovers several picoseconds later. First principles calculations suggest a theoretical pathway by which direct optical melting could be responsible for this rapid melt-recovery process.

The work in **Chapter** 5 *Nanoscale probing in RF-based UED* utilizes the high repetition rate of HiRES to probe nanoscale volumes, a previously unexplored regime for relativistic UED beamlines due to limited beam brightness. Probing of isolated nanowires is demonstrated first, including successful capturing of diffraction from individual nanowires on three different sample platforms and discussion of sample preparation strategies for pump-probe experiments. Then, focused probes with $\approx$ 500 nm rms spot size are achieved using prototype permanent magnet quadrupole lenses. Nanoimaging and nanodiffraction capabilities are demonstrated, and future developments and application of this approach is discussed.

Chapter 6 *Plasmon-enhanced photoemitters for brighter UED probes* explores plasmonic enhancement of photocathodes as a route to achieve brighter UED probes from radiofrequency photoguns, especially for nanodiffraction and nanoimaging applications. Plasmonic lenses are introduced as a promising design for generating ultrashort electron nanoprobes. Gold lenses are designed that utilize multiphoton photoemission to produce 60 nm rms electron pulses with as short as 4 fs FWHM duration. The tunability of the temporal response and yield is explored through electromagnetic simulations. High quality prototypes are fabricated and optically characterized, demonstrating the plasmonic properties desired for the application. A DC photogun for testing photoemission from such low-charge emitters is described and demonstrated on a plasmonic nanogroove photocathode, reproducing the expected power and polarization dependence. These results lay the groundwork for future demonstration and characterization of emission from plasmonic lens and other novel plasmon-enhanced photocathodes.

7.2 Future work

At present, the scientific frontiers of UED for materials science are many and far reaching. Few studies of individual 1D or 0D nanomaterial dynamics have been performed, and the possibilities for systematic, detailed examination of size-dependent effects are wide open. Many quantum materials that are not readily prepared in large area crystals have not yet been investigated. Heterostructures and device-like configurations under operating conditions have been sparingly examined, especially thicker stacks subject to large multiple scattering effects. Detailed mapping of heterogeneous dynamics across grains and interfaces has rarely been attempted.

This thesis provides new routes to explore these frontiers, including higher brightness relativistic UED probes and improved scattering models. Still, many further developments can be made in these and other areas to expand the scientific reach of UED. Continued advances in beam brightness and beamline design are needed to ultimately reach few nm lateral resolution with relativistic UED technology. Improved sample platforms and beamline configurations are needed to better manage thermal load and take full advantage of high repetition rate sources. Further development and optimization of dynamical scattering models for UED are needed to enable detailed, quantitative retrieval of complex structural changes. The work entailed here can provide a useful foundation for these pursuits.

The challenges are undoubtedly imposing, but witnessing and recording a dynamic process, especially if for the first time, is incredibly rewarding. It is a rare, privileged glimpse at the incredible, high-tempo quantum ballroom that underlies our world. In fact, if you look close enough, you just might see the atoms beckoning you to dance.

References

---

[1] D. Basov, R. Averitt, and D. Hsieh, “Towards properties on demand in quantum materials,” *Nat. Mater.*, vol. 16, pp. 1077–1088, 2017.

[2] K. Novoselov, A. Mishchenko, A. Carvalho, and A. Castro Neto, “2D materials and van der waals heterostructures,” *Science*, vol. 353, p. aac9439, 2016.

[3] E. Slot, M. Holst, H. Van Der Zant, and S. Zaitsev-Zotov, “One-dimensional conduction in charge-density-wave nanowires,” *Physical review letters*, vol. 93, p. 176602, 2004.

[4] T.-R. T. Han, F. Zhou, C. D. Malliakas, P. M. Duxbury, S. D. Mahanti, M. G. Kanatzidis, and C.-Y. Ruan, “Exploration of metastability and hidden phases in correlated electron crystals visualized by femtosecond optical doping and electron crystallography,” *Sci. Adv.*, vol. 1, p. e1400173, 2015.

[5] A. Kogar, A. Zong, P. E. Dolgirev, X. Shen, J. Straquadine, Y.-Q. Bie, X. Wang, T. Rohwer, I. Tung, Y. Yang, R. Li, J. Yang, S. Weathersby, S. Park, M. E. Kozina, E. J. Sie, H. Wen, P. Jarillo-Herrero, I. R. Fisher, X. Wang, and N. Gedik, “Light-induced charge density wave in $\mathrm{LaTe_3}$,” *Nature Physics*, vol. 16, pp. 159–163, 2020.

[6] M. J. Stern, L. P. R. de Cotret, M. R. Otto, R. P. Chatelain, J.-P. Boisvert, M. Sutton, and B. J. Siwick, “Mapping momentum-dependent electron-phonon coupling and nonequilibrium phonon dynamics with ultrafast electron diffuse scattering,” *Physical Review B*, vol. 97, p. 165416, 2018.

[7] R. Gerchberg and W. Saxton, “Phase retrieval by iterated projections,” *Optik*, vol. 35, p. 237, 1972.

[8] J. M. Cowley, *Electron diffraction techniques.* Oxford University Press, 1992, vol. 2.

[9] K. Kambe, G. Lehmpfuhl, and F. Fujimoto, “Interpretation of electron channeling by the dynamical theory of electron diffraction,” *Zeitschrift für Naturforschung A*, vol. 29, pp. 1034–1044, 1974.

[10] I. G. Vallejo, G. Gallé, B. Arnaud, S. A. Scott, M. G. Lagally, D. Boschetto, P.-E. Coulon, G. Rizza, F. Houdellier, D. Le Bolloc’H, and J. Faure, “Observation of large multiple scattering effects in ultrafast electron diffraction on monocrystalline silicon,” *Physical Review B*, vol. 97, p. 054302, 2018.

[11] L. Wei, S. Sun, C. Guo, Z. Li, K. Sun, Y. Liu, W. Lu, Y. Sun, H. Tian, H. Yang, and J. Li, “Dynamic diffraction effects and coherent breathing oscillations in ultrafast electron diffraction in layered 1 T-TaSeTe,” *Structural Dynamics*, vol. 4, p. 044012, 2017.

[12] J. Li, J. Li, K. Sun, L. Wu, H. Huang, R. Li, J. Yang, X. Shen, X. Wang, H. Luo, R. J. Cava, I. K. Robinson, Y. Zhu, W. Yin, and J. Tao, "Ultrafast decoupling of atomic sublattices in a charge-density-wave material," *arXiv preprint arXiv:1903.09911*, 2019.

[13] E. J. Kirkland, *Advanced Computing in Electron Microscopy.* Springer US, 2010.

[14] G. Sciaini and R. D. Miller, "Femtosecond electron diffraction: heralding the era of atomically resolved dynamics," *Reports on Progress in Physics*, vol. 74, p. 096101, 2011.

[15] H. A. Dürr, R. Ernstorfer, and B. J. Siwick, "Revealing momentum-dependent electron–phonon and phonon–phonon coupling in complex materials with ultrafast electron diffuse scattering," *MRS Bulletin*, vol. 46, pp. 731–737, 2021.

[16] K. M. Siddiqui, D. B. Durham, F. Cropp, C. Ophus, S. Rajpurohit, Y. Zhu, J. D. Carlström, C. Stavrakas, Z. Mao, A. Raja, P. Musumeci, L. Z. Tan, A. M. Minor, D. Filippetto, and R. A. Kaindl, "Ultrafast optical melting of trimer superstructure in layered 1T'-TaTe$_2$," *Communications Physics*, vol. 4, pp. 1–7, 2021.

[17] E. M. Mannebach, R. Li, K.-A. Duerloo, C. Nyby, P. Zalden, T. Vecchione, F. Ernst, A. H. Reid, T. Chase, X. Shen, S. Weathersby, C. Hast, R. Hettel, R. Coffee, N. Hartmann, A. R. Fry, Y. Yu, L. Cao, T. F. Heinz, E. J. Reed, H. A. Dürr, X. Wang, and A. M. Lindenberg, "Dynamic structural response and deformations of monolayer MoS$_2$ visualized by femtosecond electron diffraction," *Nano Lett.*, vol. 15, pp. 6889–6895, 2015.

[18] C. B. Carter and D. B. Williams, *Transmission electron microscopy: a textbook for materials science.* Springer Science & Business Media, 2009, vol. 2.

[19] G. Anstis, Z. Liu, and M. Lake, "Investigation of amorphous materials by electron diffraction—the effects of multiple scattering," *Ultramicroscopy*, vol. 26, pp. 65–69, 1988.

[20] K. Ishizuka and N. Uyeda, "A new theoretical and practical approach to the multislice method," *Acta Crystallographica Section A: Crystal Physics, Diffraction, Theoretical and General Crystallography*, vol. 33, pp. 740–749, 1977.

[21] C. Ophus, "A fast image simulation algorithm for scanning transmission electron microscopy," *Advanced structural and chemical imaging*, vol. 3, pp. 1–11, 2017.

[22] E. J. Kirkland, *Advanced computing in electron microscopy.* Springer, 1998, vol. 12.

[23] A. Rosenauer, M. Schowalter, J. T. Titantah, and D. Lamoen, "An emission-potential multislice approximation to simulate thermal diffuse scattering in high-resolution transmission electron microscopy," *Ultramicroscopy*, vol. 108, pp. 1504–1513, 2008.

[24] T. White, A. Eggeman, and P. Midgley, "Is precession electron diffraction kinematical? Part I: "phase-scrambling" multislice simulations," *Ultramicroscopy*, vol. 110, pp. 763–770, 2010.

[25] L. Palatinus, V. Petříček, and C. A. Corrêa, "Structure refinement using precession electron diffraction tomography and dynamical diffraction: theory and implementation," *Acta Crystallographica Section A: Foundations and Advances*, vol. 71, pp. 235–244, 2015.

[26] W. H. Press, S. A. Teukolsky, W. T. Vetterling, and B. P. Flannery, *Numerical recipes 3rd edition: The art of scientific computing.* Cambridge university press, 2007.

[27] K. Ishizuka, "Multislice formula for inclined illumination," *Acta Crystallographica Section A: Crystal Physics, Diffraction, Theoretical and General Crystallography*, vol. 38, pp. 773–779, 1982.

[28] K. Ishizuka, "FFT multislice method—the silver anniversary," *Microscopy and Microanalysis*, vol. 10, pp. 34–40, 2004.

[29] E. Owen and R. Williams, "The effect of temperature on the intensity of x-ray reflexion," *Proceedings of the Royal Society of London. Series A. Mathematical and Physical Sciences*, vol. 188, pp. 509–521, 1947.

[30] N. Singh and P. Sharma, "Debye-Waller factors of cubic metals," *Physical Review B*, vol. 3, p. 1141, 1971.

[31] R. L. Olmon, B. Slovick, T. W. Johnson, D. Shelton, S.-H. Oh, G. D. Boreman, and M. B. Raschke, "Optical dielectric function of gold," *Physical Review B*, vol. 86, p. 235147, 2012.

[32] S. J. Byrnes, "Multilayer optical calculations," *ArXiv*, p. Preprint at https://arxiv.org/abs/1603.02720, 2016.

[33] Y. Takahashi and H. Akiyama, "Heat capacity of gold from 80 to 1000 K," *Thermochimica Acta*, vol. 109, pp. 105–109, 1986.

[34] J. Williamson, M. Dantus, S. Kim, and A. Zewail, "Ultrafast diffraction and molecular structure," *Chemical Physics Letters*, vol. 196, pp. 529–534, 1992.

[35] J. C. Williamson, J. Cao, H. Ihee, H. Frey, and A. H. Zewail, "Clocking transient chemical changes by ultrafast electron diffraction," *Nature*, vol. 386, pp. 159–162, 1997.

[36] A. H. Zewail, "4D ultrafast electron diffraction, crystallography, and microscopy," *Annu. Rev. Phys. Chem.*, vol. 57, pp. 65–103, 2006.

[37] C.-Y. Ruan, F. Vigliotti, V. A. Lobastov, S. Chen, and A. H. Zewail, "Ultrafast electron crystallography: Transient structures of molecules, surfaces, and phase transitions," *Proceedings of the National Academy of Sciences*, vol. 101, pp. 1123–1128, 2004.

[38] B. J. Siwick, J. R. Dwyer, R. E. Jordan, and R. D. Miller, "An atomic-level view of melting using femtosecond electron diffraction," *Science*, vol. 302, pp. 1382–1385, 2003.

[39] R. P. Chatelain, V. R. Morrison, C. Godbout, and B. J. Siwick, "Ultrafast electron diffraction with radio-frequency compressed electron pulses," *Applied Physics Letters*, vol. 101, p. 081901, 2012.

[40] T. Van Oudheusden, P. Pasmans, S. Van Der Geer, M. De Loos, M. Van Der Wiel, and O. Luiten, "Compression of subrelativistic space-charge-dominated electron bunches for single-shot femtosecond electron diffraction," *Physical Review Letters*, vol. 105, p. 264801, 2010.

[41] V. A. Lobastov, R. Srinivasan, and A. H. Zewail, "Four-dimensional ultrafast electron microscopy," *Proceedings of the National Academy of Sciences*, vol. 102, pp. 7069–7073, 2005.

[42] B. Barwick, H. S. Park, O.-H. Kwon, J. S. Baskin, and A. H. Zewail, "4D imaging of transient structures and morphologies in ultrafast electron microscopy," *Science*, vol. 322, pp. 1227–1231, 2008.

[43] R. Alley, V. Bharadwaj, J. Clendenin, P. Emma, A. Fisher, J. Frisch, T. Kotseroglou, R. Miller, D. Palmer, J. Schmerge, J. Sheppard, M. Woodley, A. Yeremian, J. Rosenzweig, D. Meyerhofer, and L. Serafini, "The design for the LCLS RF photoinjector," *Nuclear Instruments and Methods in Physics Research Section A: Accelerators, Spectrometers, Detectors and Associated Equipment*, vol. 429, pp. 324–331, 1999.

[44] D. T. Palmer, X. J. Wang, R. H. Miller, M. Babzien, I. Ben-Zvi, C. Pellegrini, J. Sheehan, J. Skaritka, T. Srinivasan-Rao, H. Winick, M. H. Woodle, and V. Yakimenko, "Commissioning results of the BNL/SLAC/UCLA symmetrized 1.6-cell S-band emittance-compensated photoinjector," in *Free-Electron Laser Challenges*, vol. 2988. SPIE, 1997, pp. 78–89.

[45] B. Dwersteg, K. Flöttmann, J. Sekutowicz, and C. Stolzenburg, "RF gun design for the TESLA VUV Free Electron Laser," *Nuclear Instruments and Methods in Physics Research Section A: Accelerators, Spectrometers, Detectors and Associated Equipment*, vol. 393, pp. 93–95, 1997.

[46] P. Musumeci, J. Moody, and C. Scoby, "Relativistic electron diffraction at the UCLA Pegasus photoinjector laboratory," *Ultramicroscopy*, vol. 108, pp. 1450–1453, 2008.

[47] P. Musumeci, J. Moody, C. Scoby, M. Gutierrez, and M. Westfall, "Laser-induced melting of a single crystal gold sample by time-resolved ultrafast relativistic electron diffraction," *Applied Physics Letters*, vol. 97, p. 063502, 2010.

[48] J. B. Hastings, F. M. Rudakov, D. H. Dowell, J. F. Schmerge, J. D. Cardoza, J. M. Castro, S. M. Gierman, H. Loos, and P. M. Weber, "Ultrafast time-resolved electron diffraction with megavolt electron beams," *Applied Physics Letters*, vol. 89, p. 184109, Oct. 2006. http://aip.scitation.org/doi/10.1063/1.2372697

[49] S. Weathersby, G. Brown, M. Centurion, T. Chase, R. Coffee, J. Corbett, J. Eichner, J. Frisch, A. Fry, M. Gühr *et al.*, “Mega-electron-volt ultrafast electron diffraction at SLAC National Accelerator Laboratory,” *Review of Scientific Instruments*, vol. 86, p. 073702, 2015.

[50] P. Zhu, Y. Zhu, Y. Hidaka, L. Wu, J. Cao, H. Berger, J. Geck, R. Kraus, S. Pjerov, Y. Shen, R. Tobey, J. Hill, and X. Wang, “Femtosecond time-resolved MeV electron diffraction,” *New Journal of Physics*, vol. 17, p. 063004, 2015.

[51] F. Sannibale, D. Filippetto, C. F. Papadopoulos, J. Staples, R. Wells, B. Bailey, K. Baptiste, J. Corlett, C. Cork, S. De Santis, S. Dimaggio, L. Doolittle, J. Doyle, J. Feng, D. Garcia Quintas, G. Huang, H. Huang, T. Kramasz, S. Kwiatkowski, R. Lellinger, V. Moroz, W. E. Norum, H. Padmore, C. Pappas, G. Portmann, T. Vecchione, M. Vinco, M. Zolotorev, and F. Zucca, “Advanced photoinjector experiment photogun commissioning results,” *Physical Review Special Topics - Accelerators and Beams*, vol. 15, p. 103501, Oct. 2012. https://link.aps.org/doi/10.1103/PhysRevSTAB.15.103501

[52] P. Musumeci, J. Moody, C. Scoby, M. Gutierrez, M. Westfall, and R. Li, “Capturing ultrafast structural evolutions with a single pulse of mev electrons: Radio frequency streak camera based electron diffraction,” *Journal of Applied Physics*, vol. 108, p. 114513, 2010.

[53] P. Musumeci, J. Moody, C. Scoby, M. Gutierrez, and T. Tran, “Rf streak camera based ultrafast relativistic electron diffraction,” *Review of Scientific Instruments*, vol. 80, p. 013302, 2009.

[54] A. Vernes, H. Ebert, W. Bensch, W. Heid, and C. Näther, “Crystal structure, electrical properties and electronic band structure of tantalum ditelluride,” *Journal of Condensed Matter Physics*, vol. 10, pp. 761–774, 1998.

[55] T. Sörgel, J. Nuss, U. Wedig, R. Kremer, and M. Jansen, “A new low temperature modification of $\mathrm{TaTe_2}$—comparison to the room temperature and the hypothetical $\mathrm{1\,T-TaTe_2}$ modification,” *Materials Research Bulletin*, vol. 41, pp. 987 – 1000, 2006.

[56] A. Castellanos-Gomez, M. Buscema, R. Molenaar, V. Singh, L. Janssen, H. S. J. van der Zant, and G. A. Steele, “Deterministic transfer of two-dimensional materials by all-dry viscoelastic stamping,” *2D Materials*, vol. 1, p. 011002, 2014.

[57] C. Chen, H.-S. Kim, A. S. Admasu, S.-W. Cheong, K. Haule, D. Vanderbilt, and W. Wu, “Trimer bonding states on the surface of the transition-metal dichalcogenide $\mathrm{TaTe_2}$,” *Physical Review B*, vol. 98, 2018.

[58] I. El Baggari, G. M. Stiehl, J. Waelder, D. C. Ralph, and L. F. Kourkoutis, “Atomic-resolution cryo-STEM imaging of a structural phase transition in $\mathrm{TaTe_2}$,” *Microscopy and Microanalysis*, vol. 24, pp. 86–87, 2018.

[59] H. Wang, K. Chai, L. Wei, Z.-A. Li, C. Zhu, D. Zheng, Z. Li, J. Li, H. Tian, H. Yang, and J. Li, "Charge density wave and atomic trimerization in layered transition-metal dichalcogenides $1\,\mathrm{T}-\mathrm{MX}_2$ materials," *EPL*, vol. 130, 2020.

[60] M. Eichberger, H. Schäfer, M. Krumova, M. Beyer, J. Demsar, H. Berger, G. Moriena, G. Sciaini, and R. J. D. Miller, "Snapshots of cooperative atomic motions in the optical suppression of charge density waves," *Nature*, vol. 468, pp. 799–802, 2010.

[61] N. Erasmus, M. Eichberger, K. Haupt, I. Boshoff, G. Kassier, R. Birmurske, H. Berger, J. Demsar, and H. Schwoerer, "Ultrafast dynamics of charge density waves in $4\mathrm{H}_b$-TaSe_2 probed by femtosecond electron diffraction," *Physical Review Letters*, vol. 109, p. 167402, 2012.

[62] G. Storeck, J. G. Horstmann, T. Diekmann, S. Vogelgesang, G. von Witte, S. V. Yalunin, K. Rossnagel, and C. Ropers, "Structural dynamics of incommensurate charge-density waves tracked by ultrafast low-energy electron diffraction," *Structural Dynamics*, vol. 7, p. 034304, 2020.

[63] L. Perfetti, P. A. Loukakos, M. Lisowski, U. Bovensiepen, H. Berger, S. Biermann, P. S. Cornaglia, A. Georges, and M. Wolf, "Time evolution of the electronic structure of $1\,\mathrm{T}-\mathrm{TaS}_2$ through the insulator-metal transition," *Physical Review Letters*, vol. 97, p. 067402, 2006.

[64] F. Ji, D. B. Durham, A. M. Minor, P. Musumeci, J. G. Navarro, and D. Filippetto, "Ultrafast relativistic electron nanoprobes," *Communications Physics*, vol. 2, 2019.

[65] M. R. Otto, L. P. R. de Cotret, D. A. Valverde-Chavez, K. L. Tiwari, N. Émond, M. Chaker, D. G. Cooke, and B. J. Siwick, "How optical excitation controls the structure and properties of vanadium dioxide," *Proceedings of the National Academy of Sciences*, vol. 116, pp. 450–455, 2019.

[66] A. Zong, A. Kogar, Y.-Q. Bie, T. Rohwer, C. Lee, E. Baldini, E. Ergeçen, M. B. Yilmaz, B. Freelon, E. J. Sie *et al.*, "Evidence for topological defects in a photoinduced phase transition," *Nature Physics*, vol. 15, pp. 27–31, 2019.

[67] S. Sun, Z. Li, Z.-A. Li, R. Xiao, M. Zhang, H. Tian, H. Yang, and J. Li, "Cooperative inter-and intra-layer lattice dynamics of photoexcited multi-walled carbon nanotubes studied by ultrafast electron diffraction," *Nanoscale*, vol. 10, pp. 7465–7471, 2018.

[68] K. Liu, S. Lee, S. Yang, O. Delaire, and J. Wu, "Recent progresses on physics and applications of vanadium dioxide," *Materials Today*, vol. 21, pp. 875–896, 2018.

[69] J. M. Cowley and A. L. G. Rees, "Design of a high-resolution electron diffraction camera," *Journal of Scientific Instruments*, vol. 30, pp. 33–38, Feb. 1953. http://stacks.iop.org/0950-7671/30/i=2/a=301?key=crossref.0fbcc71daab6a89904e499da79ddf641

[70] R. K. Li, K. G. Roberts, C. M. Scoby, H. To, and P. Musumeci, "Nanometer emittance ultralow charge beams from RF photoinjectors," *Physical Review Special Topics - Accelerators and Beams*, vol. 15, p. 090702, Sep 2012. https://link.aps.org/doi/10.1103/PhysRevSTAB.15.090702

[71] J. K. Lim, P. Frigola, G. Travish, J. B. Rosenzweig, S. G. Anderson, W. J. Brown, J. S. Jacob, C. L. Robbins, and A. M. Tremaine, "Adjustable, short focal length permanent-magnet quadrupole based electron beam final focus system," *Physical Review Special Topics - Accelerators and Beams*, vol. 8, p. 072401, Jul. 2005. https://link.aps.org/doi/10.1103/PhysRevSTAB.8.072401

[72] R. Li and P. Musumeci, "Single-shot MeV transmission electron microscopy with picosecond temporal resolution," *Physical Review Applied*, vol. 2, p. 024003, Aug. 2014. https://link.aps.org/doi/10.1103/PhysRevApplied.2.024003

[73] "General particle tracer," http://www.pulsar.nl/gpt.

[74] D. Marx, J. G. Navarro, D. Cesar, J. Maxson, B. Marchetti, R. Assmann, and P. Musumeci, "Single-shot reconstruction of core 4D phase space of high-brightness electron beams using metal grids," *Physical Review Accelerators and Beams*, vol. 21, p. 102802, 2018.

[75] S. Borrelli, G. L. Orlandi, M. Bednarzik, C. David, E. Ferrari, V. A. Guzenko, C. Ozkan-Loch, E. Prat, and R. Ischebeck, "Generation and measurement of sub-micrometer relativistic electron beams," *Communications Physics*, vol. 1, p. 52, Dec. 2018. http://www.nature.com/articles/s42005-018-0048-x

[76] F. Ji, J. Giner Navarro, P. Musumeci, D. Durham, A. Minor, and D. Filippetto, "Knife-edge based measurement of the 4D transverse phase space of electron beams with picometer-scale emittance." Preprint at https://arxiv.org/abs/1903.12610, 2019.

[77] V. Ronchi, "Le frange di combinazioni nello studio delle superficie e dei sistemi ottici," *Riv. Ottica Mecc. Precis*, vol. 2, 1923.

[78] H. Osterberg, "Evaluation phase optical tests," *Military Standardization Handbook: Optical Design*, pp. 1–8, 1962.

[79] D. B. Durham, F. Riminucci, F. Ciabattini, A. Mostacci, A. M. Minor, S. Cabrini, and D. Filippetto, "Plasmonic lenses for tunable ultrafast electron emitters at the nanoscale," *Physical Review Applied*, vol. 12, p. 054057, 2019.

[80] D. B. Durham, S. R. Loria, F. Riminucci, K. Kanellopulos, X. Shen, F. Ciabattini, A. Mostacci, P. Musumeci, A. M. Minor, S. Cabrini *et al.*, "Design and testing of ultrafast plasmonic lens nanoemitters," in *Plasmonics: Design, Materials, Fabrication, Characterization, and Applications XVIII*, vol. 11462. SPIE, 2020, pp. 87–93.

[81] D. B. Durham, C. M. Pierce, F. Riminucci, S. R. Loria, K. Kanellopulos, I. Bazarov, J. Maxson, S. Cabrini, A. M. Minor, and D. Filippetto, “Characterizing plasmon-enhanced photoemitters for bright ultrafast electron beams,” in *Plasmonics: Design, Materials, Fabrication, Characterization, and Applications XIX*, vol. 11797. International Society for Optics and Photonics, 2021, p. 117972D.

[82] M. J. Rhee, “Refined definition of the beam brightness,” *Physics of Fluids B: Plasma Physics*, vol. 4, pp. 1674–1676, 1992. https://doi.org/10.1063/1.860076

[83] I. V. Bazarov, B. M. Dunham, and C. K. Sinclair, “Maximum achievable beam brightness from photoinjectors,” *Physical review letters*, vol. 102, p. 104801, 2009.

[84] C. M. Pierce, M. B. Andorf, E. Lu, C. Gulliford, I. V. Bazarov, J. M. Maxson, M. Gordon, Y.-K. Kim, N. P. Norvell, B. M. Dunham *et al.*, “Low intrinsic emittance in modern photoinjector brightness,” *Physical Review Accelerators and Beams*, vol. 23, p. 070101, 2020.

[85] W. Li, C. Duncan, M. Andorf, A. Bartnik, E. Bianco, L. Cultrera, A. Galdi, M. Gordon, M. Kaemingk, C. Pennington, L. Kourkoutis, I. Bazarov, and J. Maxson, “A kiloelectron-volt ultrafast electron micro-diffraction apparatus using low emittance semiconductor photocathodes,” *arXiv preprint arXiv:2111.07922*, 2021.

[86] H. U. Yang, J. D’Archangel, M. L. Sundheimer, E. Tucker, G. D. Boreman, and M. B. Raschke, “Optical dielectric function of silver,” *Physical Review B*, vol. 91, p. 235137, 2015.

[87] H. Raether, *Surface Plasmons on Smooth and Rough Surfaces and on Gratings.* Springer, 1988.

[88] M. G. Blaber, M. D. Arnold, and M. J. Ford, “A review of the optical properties of alloys and intermetallics for plasmonics,” *Journal of Physics: Condensed Matter*, vol. 22, p. 143201, 2010.

[89] K. M. McPeak, S. V. Jayanti, S. J. Kress, S. Meyer, S. Iotti, A. Rossinelli, and D. J. Norris, “Plasmonic films can easily be better: rules and recipes,” *ACS Photonics*, vol. 2, pp. 326–333, 2015.

[90] K. L. Kelly, E. Coronado, L. L. Zhao, and G. C. Schatz, “The optical properties of metal nanoparticles: the influence of size, shape, and dielectric environment,” pp. 668–677, 2003.

[91] A. Polyakov, S. Cabrini, S. Dhuey, B. Harteneck, P. Schuck, and H. Padmore, “Plasmonic light trapping in nanostructured metal surfaces,” *Applied Physics Letters*, vol. 98, p. 203104, 2011.

[92] F. Todisco, M. Esposito, S. Panaro, M. De Giorgi, L. Dominici, D. Ballarini, A. I. Fernández-Domínguez, V. Tasco, M. Cuscuna, A. Passaseo *et al.*, “Toward cavity quantum electrodynamics with hybrid photon gap-plasmon states,” *ACS Nano*, vol. 10, pp. 11 360–11 368, 2016.

[93] A. Polyakov, C. Senft, K. Thompson, J. Feng, S. Cabrini, P. Schuck, H. Padmore, S. J. Peppernick, and W. P. Hess, “Plasmon-enhanced photocathode for high brightness and high repetition rate x-ray sources,” *Physical Review Letters*, vol. 110, p. 076802, 2013.

[94] R. Li, H. To, G. Andonian, J. Feng, A. Polyakov, C. Scoby, K. Thompson, W. Wan, H. Padmore, and P. Musumeci, “Surface-plasmon resonance-enhanced multiphoton emission of high-brightness electron beams from a nanostructured copper cathode,” *Physical Review Letters*, vol. 110, p. 074801, 2013.

[95] P. Musumeci, L. Cultrera, M. Ferrario, D. Filippetto, G. Gatti, M. Gutierrez, J. Moody, N. Moore, J. Rosenzweig, C. Scoby *et al.*, “Multiphoton photoemission from a copper cathode illuminated by ultrashort laser pulses in an RF photoinjector,” *Physical Review Letters*, vol. 104, p. 084801, 2010.

[96] M. Krüger, M. Schenk, M. Förster, and P. Hommelhoff, “Attosecond physics in photoemission from a metal nanotip,” *Journal of Physics B: Atomic, Molecular and Optical Physics*, vol. 45, p. 074006, 2012.

[97] B. Piglosiewicz, S. Schmidt, D. J. Park, J. Vogelsang, P. Groß, C. Manzoni, P. Farinello, G. Cerullo, and C. Lienau, “Carrier-envelope phase effects on the strong-field photoemission of electrons from metallic nanostructures,” *Nature Photonics*, vol. 8, p. 37, 2014.

[98] S. Vogelgesang, G. Storeck, J. G. Horstmann, T. Diekmann, M. Sivis, S. Schramm, K. Rossnagel, S. Schäfer, and C. Ropers, “Phase ordering of charge density waves traced by ultrafast low-energy electron diffraction,” *Nat. Phys.*, vol. 14, pp. 184–190, 2017.

[99] M. Müller, V. Kravtsov, A. Paarmann, M. B. Raschke, and R. Ernstorfer, “Nanofocused plasmon-driven sub-10 fs electron point source,” *ACS Photonics*, vol. 3, pp. 611–619, 2016.

[100] M. Sivis, N. Pazos-Perez, R. Yu, R. Alvarez-Puebla, F. J. G. de Abajo, and C. Ropers, “Continuous-wave multiphoton photoemission from plasmonic nanostars,” *Communications Physics*, vol. 1, p. 13, 2018.

[101] Y. Y. Lau, “Effects of cathode surface roughness on the quality of electron beams,” *Journal of Applied Physics*, vol. 61, pp. 36–44, 1987. https://doi.org/10.1063/1.338833

[102] J. M. Steele, Z. Liu, Y. Wang, and X. Zhang, “Resonant and non-resonant generation and focusing of surface plasmons with circular gratings,” *Optics Express*, vol. 14, pp. 5664–5670, 2006.

[103] W. Chen, D. C. Abeysinghe, R. L. Nelson, and Q. Zhan, “Plasmonic lens made of multiple concentric metallic rings under radially polarized illumination,” *Nano letters*, vol. 9, pp. 4320–4325, 2009.

[104] A. Kolomenski, A. Kolomenskii, J. Noel, S. Peng, and H. Schuessler, “Propagation length of surface plasmons in a metal film with roughness,” *Applied optics*, vol. 48, pp. 5683–5691, 2009.

[105] M. Kuttge, E. Vesseur, J. Verhoeven, H. Lezec, H. Atwater, and A. Polman, “Loss mechanisms of surface plasmon polaritons on gold probed by cathodoluminescence imaging spectroscopy.” *Applied Physics Letters*, vol. 93, p. 113110, 2008.

[106] R. L. Olmon, B. Slovick, T. W. Johnson, D. Shelton, S.-H. Oh, G. D. Boreman, and M. B. Raschke, “Optical dielectric function of gold,” *Physical Review B*, vol. 86, p. 235147, 2012.

[107] Lumerical, “FDTD solutions,” http://www.lumerical.com.

[108] J. Bechtel, W. L. Smith, and N. Bloembergen, “Two-photon photoemission from metals induced by picosecond laser pulses,” *Physical Review B*, vol. 15, p. 4557, 1977.

[109] M. A. Laughton and D. F. Warne, *Electrical Engineer’s Reference Book*, 16th ed. Elsevier, 2003.

[110] T. Thio, K. Pellerin, R. Linke, H. Lezec, and T. Ebbesen, “Enhanced light transmission through a single subwavelength aperture,” *Optics letters*, vol. 26, pp. 1972–1974, 2001.

[111] I. R. Hooper and J. R. Sambles, “Dispersion of surface plasmon polaritons on short-pitch metal gratings,” *Physical Review B*, vol. 65, p. 165432, 2002.

[112] N. Vogel, J. Zieleniecki, and I. Köper, “As flat as it gets: ultrasmooth surfaces from template-stripping procedures,” *Nanoscale*, vol. 4, pp. 3820–3832, 2012.

[113] F. G. De Abajo, “Optical excitations in electron microscopy,” *Reviews of Modern Physics*, vol. 82, p. 209, 2010.

[114] M. Kuttge, E. J. R. Vesseur, A. Koenderink, H. Lezec, H. Atwater, F. G. de Abajo, and A. Polman, “Local density of states, spectrum, and far-field interference of surface plasmon polaritons probed by cathodoluminescence,” *Physical Review B*, vol. 79, p. 113405, 2009.

[115] C. E. Hofmann, E. J. R. Vesseur, L. A. Sweatlock, H. J. Lezec, F. J. García de Abajo, A. Polman, and H. A. Atwater, “Plasmonic modes of annular nanoresonators imaged by spectrally resolved cathodoluminescence,” *Nano Letters*, vol. 7, pp. 3612–3617, 2007.

[116] A. Losquin and M. Kociak, “Link between cathodoluminescence and electron energy loss spectroscopy and the radiative and full electromagnetic local density of states,” *ACS Photonics*, vol. 2, pp. 1619–1627, 2015.

[117] T. Coenen, B. J. Brenny, E. J. Vesseur, and A. Polman, “Cathodoluminescence microscopy: optical imaging and spectroscopy with deep-subwavelength resolution,” *MRS Bulletin*, vol. 40, pp. 359–365, 2015.

[118] M. Kociak, O. Stéphan, A. Gloter, L. F. Zagonel, L. H. Tizei, M. Tencé, K. March, J. D. Blazit, Z. Mahfoud, A. Losquin, S. Meuret, and C. Colliex, “Seeing and measuring in colours: Electron microscopy and spectroscopies applied to nano-optics,” *Comptes Rendus Physique*, vol. 15, pp. 158–175, 2014.

[119] D. B. Durham, D. F. Ogletree, and E. S. Barnard, “Scanning Auger spectromicroscopy using the ScopeFoundry software platform,” *Surface and Interface Analysis*, vol. 50, pp. 1174–1179, 2018.

[120] E. S. Barnard, “ScopeFoundry: A python platform for controlling custom laboratory experiments and visualizing scientific data,” http://www.scopefoundry.org/.

[121] T. Coenen, E. J. R. Vesseur, and A. Polman, “Angle-resolved cathodoluminescence spectroscopy,” *Applied Physics Letters*, vol. 99, p. 143103, 2011.

[122] T. Coenen, *Angle-resolved cathodoluminescence nanoscopy.* Universiteit van Amsterdam, 2014.

[123] P. Chaturvedi, K. H. Hsu, A. Kumar, K. H. Fung, J. C. Mabon, and N. X. Fang, “Imaging of plasmonic modes of silver nanoparticles using high-resolution cathodoluminescence spectroscopy,” *ACS Nano*, vol. 3, pp. 2965–2974, 2009.

[124] C. I. Osorio, T. Coenen, B. J. Brenny, A. Polman, and A. F. Koenderink, “Angle-resolved cathodoluminescence imaging polarimetry,” *ACS Photonics*, vol. 3, pp. 147–154, 2015.

[125] R. J. England, R. J. Noble, K. Bane, D. H. Dowell, C.-K. Ng, J. E. Spencer, S. Tantawi, Z. Wu, R. L. Byer, E. Peralta, K. Soong, C.-M. Chang, B. Montazeri, S. J. Wolf, B. Cowan, J. Dawson, W. Gai, P. Hommelhoff, Y.-C. Huang, C. Jing, C. McGuinness, R. B. Palmer, B. Naranjo, J. Rosenzweig, G. Travish, A. Mizrahi, L. Schachter, C. Sears, G. R. Werner, and R. B. Yoder, “Dielectric laser accelerators,” *Reviews of Modern Physics*, vol. 86, pp. 1337–1389, Dec. 2014. https://link.aps.org/doi/10.1103/RevModPhys.86.1337

[126] K. Kanellopulos, “Spiral plasmonic lens for new generation photoemitters,” Ph.D. dissertation, Politecnico di Torino, 2019.

[127] S. Rotta Loria, “Spiral plasmonic lenses for tunable nanoscale ultrafast electron emitters,” Ph.D. dissertation, Politecnico di Milano, 2020.